

---

---

# **Effective Field Theory Approach for DM in XENON100, Superradiance in Liquid Xenon, and Calibration Techniques in XENON1T**

---

---

By

RAN ITAY



Department of Particle Physics and Astrophysics  
WEIZMANN INSTITUTE OF SCIENCE

A dissertation submitted to the Weizmann Institute of Science  
in accordance with the requirements of the degree of DOCTOR  
OF PHILOSOPHY in the Faculty of Physics.

OCTOBER 2017



*“There is something fascinating about science. One gets such wholesale returns of conjecture out of such a trifling investment of fact.”*

Mark Twain .



## ABSTRACT

One of the biggest questions of astro-particle physics is the existence of dark matter. In recent years many experiments have been aiming at solving this question. Unfortunately to this date all measurements were null results, pushing the field to constantly try to extend the edge of its ability. In this thesis three studies elated to different aspects motivated by different phases in direct detection of dark matter experiments.

The first is a search for high energy nuclear recoil with the XENON100 detector based on models coming from effective field theory approach for dark matter-nucleus interactions including both elastic dark matter and inelastic dark matter. I present the first study on recoil energies above 40 keV in the XENON100 detector, searching for signature of interactions coming from these models.

The second study is the develop of a liquid xenon apparatus aiming at measuring quantum scintillation properties of liquid xenon, mainly searching for superradiance effects. A better understanding of these process can help in discriminating background currently considered as irreducible.

The third study is on an external calibration technique for XENON1T detector. In order to discriminate between background and the expected signal, intensive calibration is required. Ton-scale detectors cannot be calibrated using the techniques previously used due to the self shielding of the xenon. I present a technique used in XENON1T to obtain calibration of electromagnetic interactions.



## **DEDICATION AND ACKNOWLEDGEMENTS**

**H**ere goes the dedication.



## AUTHOR'S DECLARATION

I declare that the work in this dissertation was carried out in accordance with the requirements of the University's Regulations and Code of Practice for Research Degree Programmes and that it has not been submitted for any other academic award. Except where indicated by specific reference in the text, the work is the candidate's own work. Work done in collaboration with, or with the assistance of, others, is indicated as such. Any views expressed in the dissertation are those of the author.

SIGNED: ..... DATE: .....



## TABLE OF CONTENTS

	<b>Page</b>
<b>List of Tables</b>	<b>xii</b>
<b>List of Figures</b>	<b>xiii</b>
<b>1 Introduction</b>	<b>1</b>
1.1 Evidence for the Existence Of Dark Matter . . . . .	1
1.1.1 Virial Theorem . . . . .	2
1.1.2 Galactic Rotation Curves . . . . .	2
1.1.3 Gravitational Lensing . . . . .	3
1.1.4 Cosmic Microwave Background . . . . .	4
1.1.5 Big Bang Nucleosynthesis . . . . .	6
1.2 Particle Candidates and Other Solutions to the Dark Matter Problem . . . . .	7
1.2.1 Axions . . . . .	7
1.2.2 Primordial Black Holes . . . . .	7
1.2.3 Modified Newtonian Dynamics . . . . .	7
1.2.4 Weakly Interacting Massive Particles . . . . .	8
1.3 Dark Matter Detection . . . . .	10
1.3.1 Colliders Searches . . . . .	10
1.3.2 Indirect Detection Search . . . . .	11
1.3.3 Direct Detection Search . . . . .	13
1.4 Interaction Rate . . . . .	13
1.4.1 WIMP Nucleus Interaction Cross Section . . . . .	14
1.4.2 Form Factors . . . . .	15
1.5 Effective Field Theory Approach for WIMP-Nucleolus Scattering . . . . .	16
1.6 Direct Detection Strategies . . . . .	17
1.7 Nobel Liquid Detectors . . . . .	19
1.7.1 Single Phase Detectors . . . . .	19
1.7.2 Dual Phase Detectors . . . . .	20
1.8 Non Linear Emission of Radiation in Liquid Xenon . . . . .	20
1.9 The XENON Program . . . . .	23

---

**TABLE OF CONTENTS**

---

1.9.1	XENON10 . . . . .	23
1.9.2	XENON100 . . . . .	24
1.9.3	XENON1T . . . . .	25
1.9.4	XENONnT . . . . .	27
<b>2</b>	<b>Effective Field Theory Search for High Energy Nuclear Recoils in XENON100 Detector</b>	<b>29</b>
2.1	Low Energy Channel . . . . .	30
2.2	High Energy Channel . . . . .	32
2.3	Signal model . . . . .	34
2.3.1	Elastic scattering . . . . .	35
2.3.2	Inelastic WIMP scattering . . . . .	35
2.4	Statistical inference . . . . .	36
2.5	Data From Recoil Energies Up To 1000 PE . . . . .	38
2.6	Results . . . . .	40
2.7	Summary . . . . .	42
<b>3</b>	<b>Direxeno</b>	<b>45</b>
3.1	Experimental Setup . . . . .	45
3.1.1	The gas handling system . . . . .	47
3.1.2	The cryogenic system . . . . .	48
3.1.3	The detector system . . . . .	50
3.1.4	The data acquisition system . . . . .	52
3.2	Optical properties of the sphere . . . . .	53
3.3	Detector sensitivity . . . . .	56
3.4	Summary . . . . .	59
<b>4</b>	<b>Calibration System for Xenon1T</b>	<b>61</b>
4.1	Radioactive source . . . . .	62
4.1.1	ER band calibration . . . . .	62
4.1.2	Charge collection efficiency . . . . .	65
4.2	Collimators . . . . .	65
4.2.1	Simulation . . . . .	66
4.3	Summary . . . . .	68
<b>A</b>	<b>EFT SIGNAL MODEL DETECTOR RESPONSE TABLE</b>	<b>71</b>
<b>Bibliography</b>		<b>75</b>

## LIST OF TABLES

TABLE	Page
2.1 Definitions and contents of the analysis bins for the high-energy channel. . . . .	34
3.1 Anisotropic emission patterns. For all patterns $r_{aniso} = 0.1$ . . . . .	56
3.2 The parameters used in simulation . . . . .	57
4.1 High energy gamma lines from $^{228}\text{Th}$ decay chain . . . . .	64
4.2 result of GEANT4 simulations for a 16X16X16cm collimator . . . . .	68
4.3 Result of GEANT4 simulation for a 10X10X10cm collimator . . . . .	69
A.1 Detector response table using $\mathcal{L}_{\text{eff}}$ with constrained scaling parameter set to $-1\sigma$ value	72



## LIST OF FIGURES

<b>FIGURE</b>	<b>Page</b>
1.1 Rotation curve of NGC 6503 . . . . .	3
1.2 Strong lensing . . . . .	4
1.3 Bullet Cluster . . . . .	5
1.4 Plank 2015 CMB power spectrum . . . . .	6
1.5 WIMP freeze out . . . . .	9
1.6 DM detection channels . . . . .	10
1.7 Limits on DM from the LHC . . . . .	11
1.8 AMS-02 observetaion of a 1TeV WIMP . . . . .	12
1.9 Differential event rate for various elements. . . . .	14
1.10 Muon flux in underground facilities . . . . .	18
1.11 Excitation detection channels. . . . .	19
1.12 Comparison between ordinary fluorescence and superradiance. . . . .	22
1.13 The XENON Program detectors . . . . .	24
1.14 TPC detection principle . . . . .	25
1.15 XENON1T Image . . . . .	26
1.16 XENON exclusion limits and sensitivities . . . . .	26
2.1 drde for example operators. . . . .	30
2.2 Summary of regions of interest backgrounds, and observed data . . . . .	31
2.3 The total acceptance of all cuts used . . . . .	33
2.4 The expected signal in the high-energy region . . . . .	36
2.5 The expected signal in low energy region . . . . .	37
2.6 Super high energy phase space . . . . .	39
2.7 The XENON100 limits (90% C.L. <sub>S</sub> ) on isoscalar dimensionless coupling for all elastic scattering EFT operators . . . . .	41
2.8 90% C.L. <sub>S</sub> limits, for the inelastic model . . . . .	42
2.9 The XENON100 90% C.L. <sub>S</sub> limits on a $1 \text{ TeV}/c^2$ WIMP isoscalar dimensionless coupling constant as function of the WIMP mass splitting $\delta_m$ . . . . .	43
3.1 A schematic view of DireXeno. . . . .	46

---

## LIST OF FIGURES

3.2	The DireXeno system . . . . .	47
3.3	DireXeno gas schematics . . . . .	48
3.4	The cryogenic system . . . . .	49
3.5	The HPFS shell . . . . .	51
3.6	PMT holder . . . . .	52
3.7	Detector part . . . . .	54
3.8	DireXeno DAQ schematics . . . . .	55
3.9	Some relevant characteristics of HPFS-8655. . . . .	55
3.10	$\langle\chi^2_v\rangle$ test example. . . . .	58
3.11	Simulation of Number of events for discovery . . . . .	58
4.1	Attenuation coefficient of xenon . . . . .	63
4.2	$^{228}\text{Th}$ decay chain . . . . .	64
4.3	$^{137}\text{Cs}$ decay . . . . .	65
4.4	(a) The cryostat and the collimator, (b) CAD design of the collimator . . . . .	66
4.5	A picture of the two belts . . . . .	67
4.6	A top view of the water tank . . . . .	67
4.7	I-Collimator (a) scatter of good calibration events in the sensitive volume (b) Intial momentum of background events . . . . .	68
4.8	U-Collimator (a) scatter of good calibration events in the sensitive volume (b) Intial momentum of background events . . . . .	69
A.1	A visualization of the detector response table for $-1\sigma$ (i.e. conservative) $\mathcal{L}_{\text{eff}}$ . . . . .	73

## INTRODUCTION

The most accredited theoretical framework for the cosmology of our universe, based on numerous cosmological and astronomical observations, is the "Λ-Cold Dark Matter" model (Λ-CDM). It suggests that only a small fraction ( $\sim 5\%$ ) of the energy density in the universe is in the form of baryonic matter, the rest  $\sim 95\%$  is lurking in the dark [1, 2]. The "Dark-sector" consist of *Dark Energy* ( $\sim 69\%$ ) and a non-baryonic matter ( $\sim 26\%$ ), *Dark Matter* (DM).

In the 1930s the Swiss astronomer Fritz Zwicky observed that the mass of the cluster inferred by gravitational observation is much larger than the one inferred by the visible luminous light matter. He then deduced the existence of a new type of unseen matter which does not interact with electromagnetic radiation, naming this matter "*dunkle materie*", *Dark Matter* [3]. Since then much evidence has been accumulated, suggesting that DM is present at galactic as well as cosmological scales.

In the past decade many experiments joined the race towards DM detection, and the field has progressed dramatically. These experiments can be divided roughly into three groups, underground direct detection experiments such as XENON [4, 5], LUX [6], PANDAX [7], CDMS [8], DAMA/LIBRE [9] and others , indirect detection in space (FERMI [10], AMS [11]) and on earth (IceCube [12]), and production experiments in accelerators such as ATLAS [13] and CMS [14] at the Large Hadron Collider.

### 1.1 Evidence for the Existence Of Dark Matter

An extensive amount of observations pointing to the presence of DM at the single-galaxy, intergalactic and cosmological scales, are present. In this section a brief summary of these observation is presented.

### 1.1.1 Virial Theorem

The virial theorem relates the average potential energy density  $\langle V_p \rangle$  of a stationary gravitationally bound system to its mean kinetic energy density  $\langle T_k \rangle$ , namely:

$$(1.1) \quad \langle T_k \rangle = -\frac{1}{2} \langle V_p \rangle.$$

In the 1930s Zwicky made the puzzling observation that the velocity dispersion of individual nebulae in the large Coma galaxy cluster contradicts the expectation of the virial theorem, if estimating the total mass solely from the visible matter content [3]. Additional mass in the form of DM needs to be added to explain the observations. Although Zwicky did not take into account the mass of the hot plasma in the cluster, adding it reduces the discrepancies but doesn't solve it.

The hot plasma bounded by the gravitational potential of the cluster emits bremsstrahlung X-rays. The x-ray emission is proportional to the plasma density squared. This can be used to estimate the the total mass and mass profile of clusters assuming the cluster is virialized. This type of observations suggest that DM rather than baryonic matter dominates the dynamics of clusters [15].

### 1.1.2 Galactic Rotation Curves

The orbital velocity as a function of radius (rotation curve) can be obtained from the measurement of the redshifts of the 1420 MHz hydrogen transition [16] as well as of spectral lines from stars. The hydrogen cloud extends beyond the galactic disk, allowing the measurement of orbital velocities further out. By measuring the rotation curve of galaxies it is possible to compute their mass profile ( $M(r)$ ).

In 1970 Vera Rubin found a disagreement in the mass profile calculated by the rotation curves and the one expected from luminous matter in NGC4605 spiral galaxy [17]. This disagreement can be solved, assuming additional non-visible mass enhancing the gravitational forces.

Formally, assuming Newtonian dynamics

$$(1.2) \quad v(r) = \sqrt{\frac{G \cdot M(r)}{r}},$$

where

$$(1.3) \quad M(r) = \int_0^r 4\pi\rho(r)r^2 dr.$$

The majority of a galaxy's luminous mass is situated at the close vicinity of its center ; therefore if no other mass exist, at large radii one would expect  $v(r) \sim r^{-1/2}$ . In contradiction the measurements done by Rubin and in many more experiments indicate  $v(r) \sim \text{const}$ , see Fig. 1.1. Adding DM with density profile  $\rho(r) \sim r^{-2}$  explains this observations.

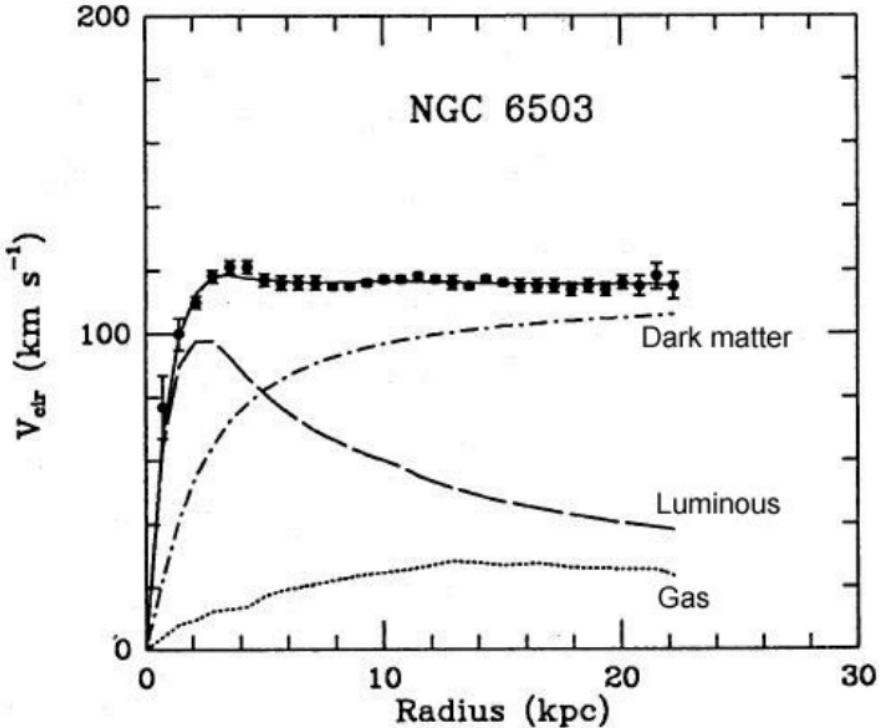


FIGURE 1.1. Measured Rotation curve (solid line) of NGC 6503 galaxy. In dashed, luminous component only. In dotted, the gas component, and expected DM halo in dotted-dashed. Image taken from [16].

### 1.1.3 Gravitational Lensing

One of the predictions of general relativity is that trajectory of light in space is determined by the space-time metric, which is determined by the mass distribution. Due to this effect, when a large gravitational potential is located in the line of sight between an observer and a far galaxy, the light from the galaxy is distorted. This phenomena is called Gravitational Lensing [18]. By analyzing the lensed image, the mass profile of the "lens" can be characterized.

*Strong Lensing* is when the gravitational field of the "lens" is so strong it produces multiple images forming an Einstein's cross, as well as Einstein's rings [19]. In Fig. 1.2(a) is a picture of the largest lensing galaxy cluster observed, Abell 1689. In Fig. 1.2(b) is the a lensed, multiple image picture of the quasar QSO-2237.

Two important features are concuded when analyzing the mass profile of the "lens": 1) DM and ordinary matter are not misaligned [20]. 2) The mass profile follows  $\rho(r) \propto r^{-2}$  dispersion ratio [21].

*Weak Lensing* is when the light coming from the source is only weakly distorted by the gravitational lens. In this case it is impossible to detect an individual lensed source; however, multiple background sources align symmetrically around the lens, allowing the detection of the

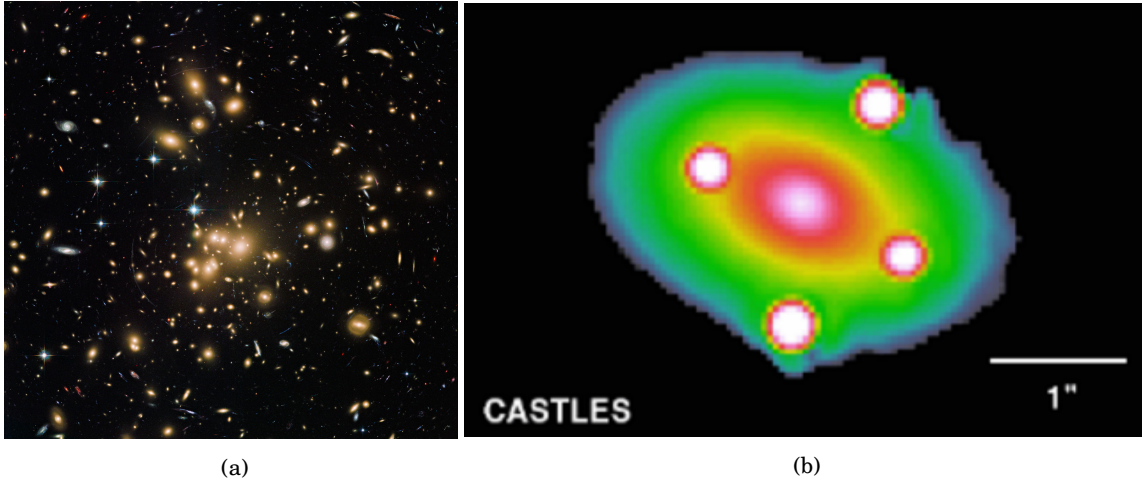


FIGURE 1.2. (a) Hubble Space Telescope Advanced Camera for Surveys image of the lensing cluster Abell 1689. Image credit: ESA/Hubble. (b) QSO-2237 quasar lensed image, creating both einstein's arcs and cross. Image credit: CASTLES

lens mass [22].

The most famous weak lensing evidence for DM comes from the "Bullet Cluster", a lensed image of a collision of two galaxies, 1E0657-56 and MACS J0025.4-1222 [23]. In this observation (see Fig. 1.3), it is clear that the mass distribution of the luminous and non-luminous matters are spatially displaced. While the luminous matter seems to experienced a violent collision, the non-luminous matter seems to be unaffected. The collisionless behaviour of the DM puts strong constrains on its self interaction [24].

#### 1.1.4 Cosmic Microwave Background

The most precise constraint of the abundance of dark matter in the Universe and a landmark test on the  $\Lambda$ -CDM model comes from the measurements of the cosmic microwave background (CMB). The CMB is a reminisce thermal electromagnetic radiation field from the early Universe.

At the early stages of the Universe, it was hot, dense, and filled with plasma. Then after expanding enough the temperature dropped, and electrons and protons recombined creating hydrogen atoms. At that stage (referred as "recombination time"), as the density of free electrons dropped, the thermal radiation could travel freely, without being scattered. These photons propagate through the Universe ever since.

The CMB follows with extreme precision the spectrum of a black body with temperature of 2.726 K. It is also known to be very isotropic and temperature anisotropy is at the scale of  $10\mu\text{K}$ . These temperature fluctuations, considered Gaussian [1], are usually expanded using spherical

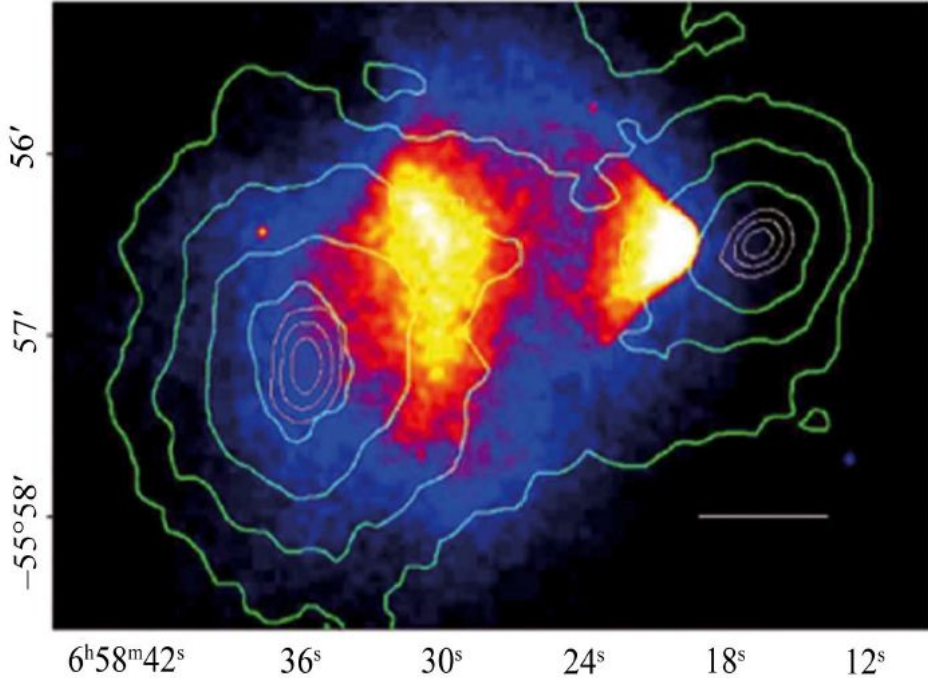


FIGURE 1.3. Contours of spatial distribution of mass, from gravitational lensing overplotted over Chandra x-ray data that traces hot plasma in a galaxy. It can be seen that most of the matter resides in a location different from the plasma, which underwent frictional interactions during the merger and slowed down.

harmonics,

$$(1.4) \quad \frac{\delta T}{T}(\theta, \phi) = \sum_{l=2}^{\infty} \sum_{m=-l}^{m=l} a_{lm} Y_{lm}(\theta, \phi).$$

The variance of the coefficient  $a_{lm}$  denoted as  $c_l$  is defined:

$$(1.5) \quad c_l \equiv \langle a_{lm} \rangle = \frac{1}{2l+1} \sum_{m=-l}^{m=l} a_{lm}^2$$

All DM relevance information from CMB can be extracted from the power spectrum of  $c_l$  as a function of the multipole  $l$ . The shape of the power spectrum follows the oscillations of the plasma in the early Universe. In general, the flatness of the Universe can be extracted from the position of the first peak. The ratio between the baryonic and non-baryonic matter is extracted from the ratio between the first two peaks.

More specifically, there are many parameters which affect the CMB spectrum, amongst them are the DM density ( $\Omega_{DM}$ ), the baryonic matter density ( $\Omega_b$ ) and the Hubble constant ( $h$ ). Assuming a cosmological model with fixed number of parameters the best fit to the spectrum determines the values of the parameters. The most updated measurement of the CMB spectrum seen in Fig 1.4 constrains the values of the above mentioned parameters [2] to:

$$(1.6) \quad \Omega_{DM} h^2 = 0.1197 \pm 0.0022 \quad \Omega_b h^2 = 0.00222 \pm 0.00023 \quad h = 0.67 \text{ [100 km/s/Mpc]}$$

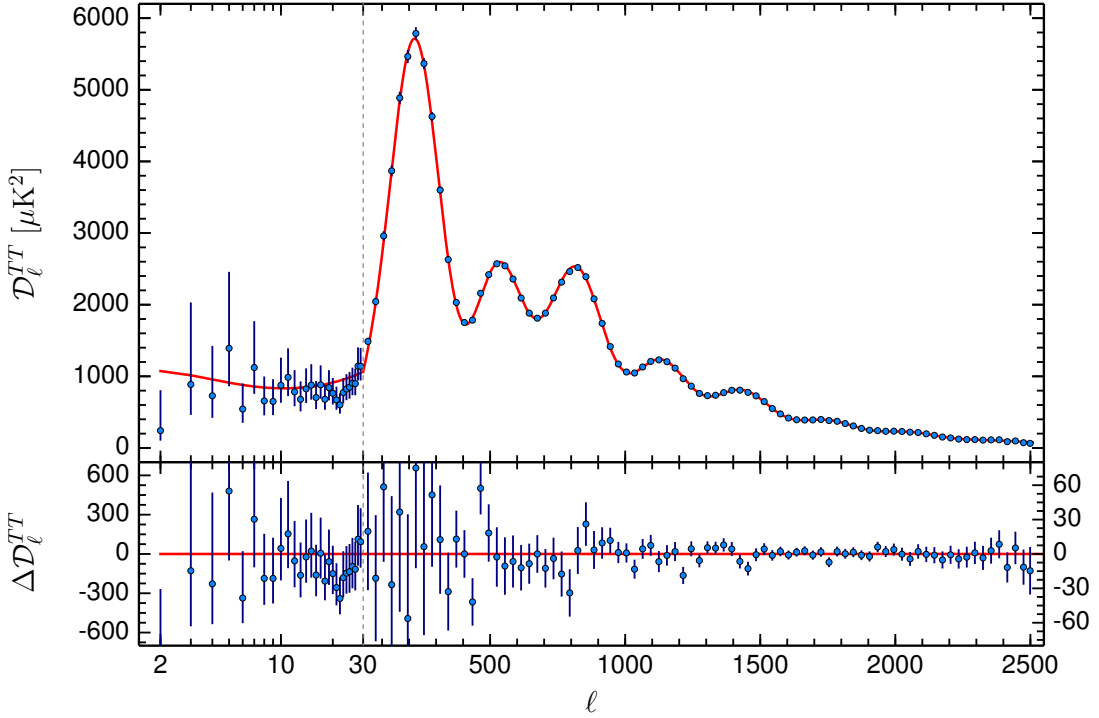


FIGURE 1.4. The Planck 2015 temperature power spectrum the solid line is the best fit for the  $\Lambda$ -CDM model, the error bars show  $\pm\sigma$  uncertainties

### 1.1.5 Big Bang Nucleosynthesis

Big Bang Nucleosynthesis (BBN) is a theory describing the production of the lightest nuclei via a dynamic interplay amongst the four fundamental forces during the first seconds of the Universe [25]. The BBN process started when the Universe expanded and became cold enough for electrons and protons to recombine, creating light elements such as Helium, Deuterium, and Lithium, it lasted  $\sim 20$  min.

The abundance of the lightest nuclei created in the BBN era can be parametrized by the baryonic density  $\Omega_b$  only. This can be done as DM doesn't affect the expansion rate of the Universe, because the Universe is radiation dominant. The inferred value of  $\Omega_b$  which gives the correct abundance, coincide with the one measured by CMB, supporting the existence of non-baryonic matter constituting a large fraction of the matter in the Universe.

## 1.2 Particle Candidates and Other Solutions to the Dark Matter Problem

As discussed in previous section there is a large number of convincing evidences for supporting the existence of DM in the Universe, of which its nature is yet unknown. In this section is a short discussion of possible candidates for DM particles, as well as an alternative solution involving the modification of Newton's laws.

### 1.2.1 Axions

Axions are neutral pseudoscalars initially introduced by Peccei and Quinn in 1977 to solve the "strong CP problem" [26]. The Standard model of particles (SM) contains a CP violating proportional to the parameter  $\bar{\theta} = \theta_{weak} + arg(det(M))$ . From measurements of the electrical dipole moment of the neutron the  $\bar{\theta}$  parameter is constrained to be smaller than  $10^{-10}$  [27, 28]. The question why the  $\bar{\theta}$  parameter is so small is known as the strong CP problem. An elegant solution to this problem is introducing an additional global  $U(1)$  symmetry, spontaneously broken producing a Goldstone boson known as the axion.

Many theoretical and experimental efforts were invested in axion search. The original proposed Peccei-Quinn axion with symmetry breaking scale in the order of the weak scale (246 GeV) is ruled out; however, axion and axion like particles (ALPs) are still allowed [29, 30]

### 1.2.2 Primordial Black Holes

primordial black hole (PBH) are a postulated type of black holes formed at the era before BBN, thus they are not subject to the baryon to photon ration, which gives the baryon density. They were first introduced by Stephen Hawking [31] at 1971, and they can theoretically account for fraction of the DM density [32].

Limits on the mass of PBH can be placed from the lack of Hawking-radiated gamma-rays [33], combined with null results from microlensing surveys, and constraints based on the CMB [34]. The current allowed mass range of of DM in the form of PBH is  $(10^{14}\text{--}10^{23})\text{ kg}$ .

### 1.2.3 Modified Newtonian Dynamics

Although the cold dark matter paradigm solves the problems arising from several observations that are mentioned above, there are other paradigms that answer this puzzling observations. The most reasonable is Modified Newtonian Dynamics (MOND) [35] suggested by Mordechai Milgrom at 1983.

The theory of MOND holds that newton laws should be modified as follows:

$$(1.7) \quad f = ma \Rightarrow f = \mu \left( \frac{a}{a_0} \right) ma,$$

where  $\mu$  is a function between 0 - 1 and  $a_o \approx 10^{10}$  is a constant with acceleration units. At high acceleration  $\mu = 1$  and this reproduces Newton's law; however at small accelerations  $\mu \approx \frac{a}{a_o}$ . This small modification solves the mass discrepancies arising from rotation curves up to a factor of 2 which can be easily explained by some baryonic matter that can not be observe because of its weak luminosity.

Although MOND solves the missing mass from rotation curves, in order to solve the lensing observations one needs to take into account relativistic modifications. The Tensor-Vector-Scalar (TeVeS) gravity [36]. Due to the relativistic nature of TeVeS it can explain also gravitational lensing.

Although MOND and TeVeS can explain some phenomena which are hard to explain in the DM paradigm, They still cannot explain all evidences mentioned above. Mainly observations coming from strong lensing, and CMB still do not have an adequate explanations in these paradigms.

#### 1.2.4 Weakly Interacting Massive Particles

In order to solve the DM problem it seems natural to extent the matter content in the SM. Ideally a good DM particle candidate, apart from being electromagnetically neutral, should be non-baryonic and stable over the age of the Universe resulting in the correct abundance starting from thermal reactions in the early stage of space and time. The generic idea of a weakly interacting massive particle (WIMPs), has become one of the most favored dark matter candidates [37].

Freeze-out is an appealing mechanism to generate a fixed amount of a specific matter. It is already successfully explained photon decoupling (CMB) and the production of nuclei (BBN). At early stages of the Universe it was hot and dense and particles were in chemical equilibrium between creation and annihilation reactions between various particles and radiation types. DM particles  $\chi$  could transform into other SM particles by co-annihilation, or be produced from the same process in SM particles.

$$(1.8) \quad \chi\bar{\chi} \leftrightarrow f\bar{f}, W^+W^-, HH, \dots$$

The annihilation rate is determined by  $R_{ann} = \langle \sigma_{ann} v \rangle n$  where  $\sigma_{ann}$  is the thermal average of the self-interaction cross section,  $v$  and  $n$  are the relative velocity and number density of DM particles respectively. For the creation process, the available kinetic energy of colliding particles must exceed the mass threshold of generating a  $\chi\bar{\chi}$  pair. During equilibrium the energy distribution is assumed to be thermalized and follow a Maxwell-Boltzmann distribution  $e^{E/K_B T}$ . When the Universe expanded enough, the temperature dropped and collision of SM particles were not energetic enough the create DM  $\chi\bar{\chi}$  pairs, causing the number density of DM to decrease faster then SM particles. At some point the Universe expansion rate became larger than DM annihilation rate causing the number density of DM to freeze-out. This moment in time, defines the exact number of DM particles inside a comoving volume. The time-evolution of the number

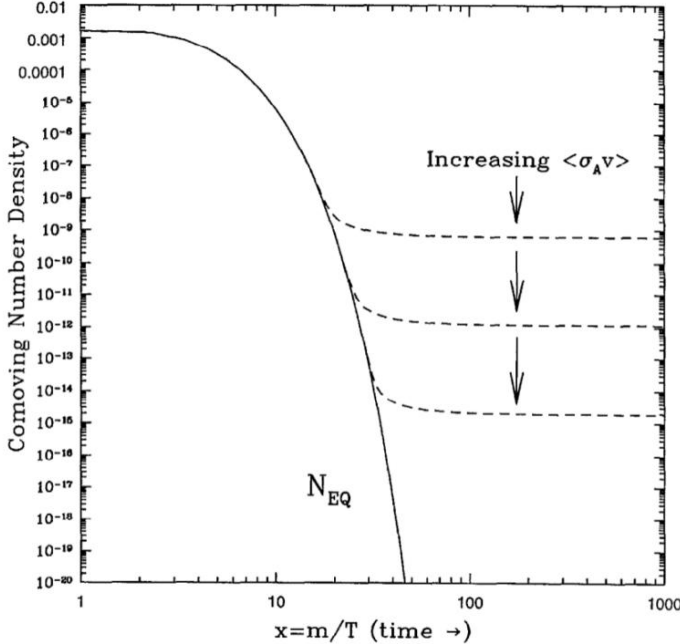


FIGURE 1.5. Evolution of the dark matter number density as a function of mass over temperature in the universe (proportional to increasing time after the Big Bang). Different assumed annihilation cross-sections  $\sigma_{ann}$  lead to differing relic dark matter number densities. Image taken from [38]

density as a function of  $1/T$  (proportional to the time passed from equilibrium) is illustrated in Fig. 1.5).

From calculation of the DM particles abundance, the freeze out temperature is estimated to be  $T_{fo} \approx m_\chi/20$ . The number density after freeze-out depends strongly on the co-annihilation rate and decreases for larger values of  $\langle\sigma_{ann}v\rangle$ . Assuming  $\Lambda$ -CDM description of the Universe evolution, The current relic abundance for DM  $\Omega_\chi h^2$  can be simplified to:

$$(1.9) \quad \Omega_\chi h^2 \approx \frac{3 \times 10^{-27} \text{ cm}^3 \text{ s}^{-1}}{\langle\sigma_{ann}v\rangle}.$$

Equation 1.9 yields that a the co-annihilation cross section is  $\sim 10^{-26}$ , which is typical for the electroweak scale, where it is expected to find new physics. This great coincidence is called the *The WIMP Miracle*.

In several extension of the SM such as Super Symmetry, a particle candidate with such properties arise naturally. The motivation from cosmology along with the ones from particle physics have promoted the WIMP to be one of the leading classes of DM candidates.

Over the years many extension and modifications to the WIMP paradigm have been proposed. These modifications include the *inelastic WIMP* [39]. In this scenario, WIMPs ( $\chi_1$ ) have 3 important additional features:

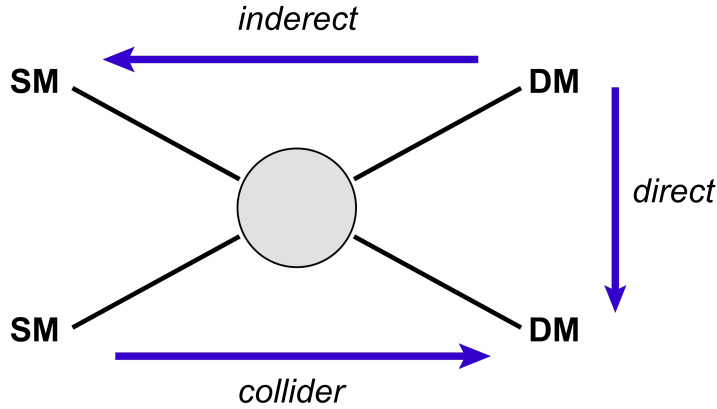


FIGURE 1.6. A schematics of the potential channels for DM detection.

- Highly suppressed elastic scattering cross section with nuclei.
- Second mass state  $\chi_2$  heavier than  $\chi_1$  where  $\delta_m$  is of the order of a typical halo WIMP kinetic energy. Generally,  $\delta \sim 100$  keV for weak scale values.
- Allowed scattering off of nuclei with an inelastic transition of the dark matter particle, i.e.,  $\chi_1 + n \rightarrow \chi_2 + n$

## 1.3 Dark Matter Detection

The extensive amount of convincing evidence explained in 1.1 lead to a world race towards the detection of DM. There are three main channels to probe DM interaction, a schematic of which is shown in Fig 1.6.

### 1.3.1 Colliders Searches

WIMPs can be produced by the energetic collision of two SM particles (e.g.,  $q\bar{q}$ ,  $ee^+$ ). The signature expected for such process include quark jets, leptons, but more importantly missing transverse momentum carried away by the undetectable produced DM particle. So far all searches of colliders have ended up with null results 1.7.

Even upon detection, the full nature of DM cannot be probed in collider experiment as they cannot prove stability beyond the traveling time in the detector, a key ingredient for WIMPs. Moreover the compression between collider results and direct detection ones, is not trivial, and can be done only in a model dependent way.

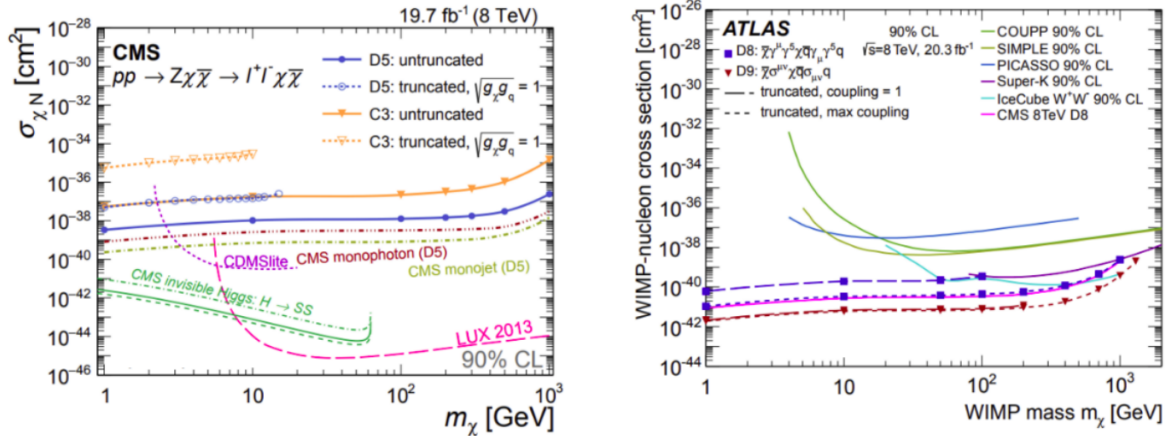


FIGURE 1.7. 90%CL upper limits on the DM-nucleon scattering cross section, from the monojet, monophoton, and mono-Z searches, as a function of the DM mass. left (right) Spin-independent (spin-dependent) interaction. Several interaction types and dark-matter particle natures are considered [40].

### 1.3.2 Indirect Detection Search

Indirect detection refers to a technique that uses observations of SM particles which can be created from the co-annihilation or decay of dark matter in our Galaxy and throughout the Universe. The total number of dark-matter particles does not change significantly after freeze-out in the early universe, but their spatial distribution changes considerably during structure formation.

The signals in indirect searches are SM products of the dark matter annihilation and decay process. most channels result immediately in unstable SM particles which quickly decay and hadronize into stable states. Stable states include photons, neutrinos, electrons and positrons, protons antiprotons, and heavier nuclei and anti-nuclei. For a thorough review on indirect detection searches see [41].

#### $\gamma$ -ray channel

$\gamma$ -ray can be produced from WIMP annihilation in various ways: the annihilation into quarks and gauge bosons resulting in a continuous spectrum; direct annihilation to  $\gamma$ -rays and virtual internal bremsstrahlung resulting in spectral features, which constitute a smoking-gun signal that cannot be explained without DM.

These expected signals are overlaid with background coming from conventional astrophysical sources. In WIMP mass between O(100 MeV) – O(100 GeV), pair-conversion telescopes on satellites (e.g., Fermi Large Area Telescope) are most sensitive. For WIMP mass above  $\sim 10$  GeV

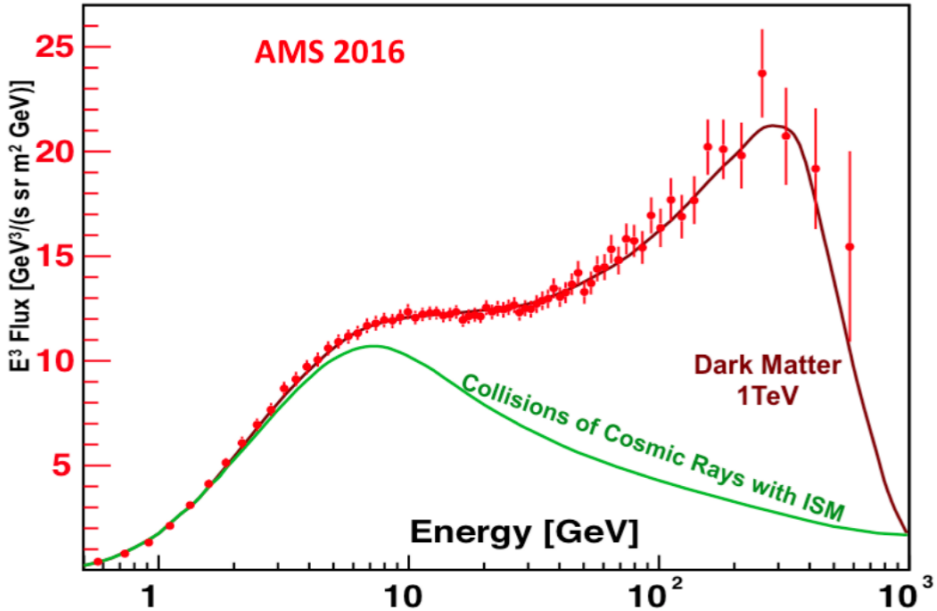


FIGURE 1.8. The current AMS positron flux measurement compared with theoretical models. The green line represents the expected flux of positrons from cosmic rays collisions with interstellar material, the red line is the expected spectrum of a 1 TeV WIMP, and the light red data points are the observed flux.

Imaging Air Cherenkov Telescopes (e.g., HESS, MAGIC, VERITAS) become more sensitive.

### Charge Cosmic Rays

In this channel the main signature for DM is in the anti-proton and positron flux. As anti-particles are only produced seldom, even a small addition of WIMP annihilation produced anti-particles is detectable. The signal reveals itself as a rise in the ratio of particle anti-particle flux (e.g.,  $e/e^+$ ). Measuring the ratio also reduces the uncertainties of the measurement.

The leading experiment in this channel is AMS-02 which detected a rise in the positron flux in 2013 [42] and in 2016 released a press note with claims of a signal of WIMPs with mass of 1 TeV (see Fig. 1.8). These results can be explained also by other ways [43] and are not published in a paper yet.

### Neutrino Channel

DM can be gravitationally trapped in celestial bodies such as stars and planets. This results in an enhanced DM population near the center of these objects. As a consequence of the increased density the annihilation rate of DM inside stars is substantially larger. All the produced particles

will thermalize except for the neutrinos which will escape and can be detected by neutrino detectors such as IceCube [44] and ANTARES [45] which sets currently the strongest limits from this channel.

### 1.3.3 Direct Detection Search

This search channel refers to measuring on Earth, the interaction between WIMPs and SM particles. Experiments trying to observe WIMP interaction through this channel (e.g., XENON, LUX, ArDM, CDMS and more) are situated in underground laboratories. The various detection strategies as well as relevant calculations are presented in the following sections.

## 1.4 Interaction Rate

If WIMPs are moving through Earth, a large number of them, are expected to pass through any terrestrial detector. The rate of interactions per unit mass on a target is:

$$(1.10) \quad dR = \frac{N_0}{A} \sigma v dn(v),$$

where  $A$  is the atomic mass of the target,  $\sigma$  is the cross section,  $N_0$  is Avogadro number. The differential particle density  $dn(v)$  is

$$(1.11) \quad dn(v) = \frac{\rho_\chi}{m_\chi * k} f(v, v_E) d^3 v,$$

where  $v$  is the WIMP velocity in the detector rest frame,  $v_E$  is the Earth velocity in the galactic rest frame, and  $f(v, v_E)$  is the WIMP velocity distribution usually assumed to be a Maxwell-Boltzmann distribution

$$(1.12) \quad f(v, v_E) = \exp\left(\frac{-(v + v_E)^2}{\sigma_v^2}\right),$$

where  $\sigma_v$  is the WIMP speed dispersion. The normalization factor  $k$  is defined such that

$$(1.13) \quad k = \int_0^{2\pi} d\phi \int_{-1}^1 d(\cos(\theta)) \int_0^{v_{esc}} \exp\left(\frac{-(v + v_E)^2}{\sigma_v^2}\right),$$

yielding,

$$(1.14) \quad \int_0^{v_{esc}} dn \equiv \frac{\rho_\chi}{m_\chi}$$

where  $v_{esc}$  is the local galactic escape velocity. Standard values for the velocity distribution parameters are:

$$(1.15) \quad \sigma_v = 230 \text{ km/s}, \quad v_{esc} = 600 \text{ km/s} \rightarrow k \approx (\pi \sigma_v^2)^{3/2}$$

The recoil energy of a nucleus with mass  $m_N$  struck by a DM particle with kinetic energy  $E = \frac{1}{2}M_\chi v^2$  scattered at an angle  $\theta$  is:  $E_R = E_0 r (1 - \cos(\theta))/2$  where  $r \equiv \frac{4M_\chi M_N}{(M_\chi + M_N)^2}$  and  $E_0 = \frac{1}{2}M_\chi \sigma_v^2$ .

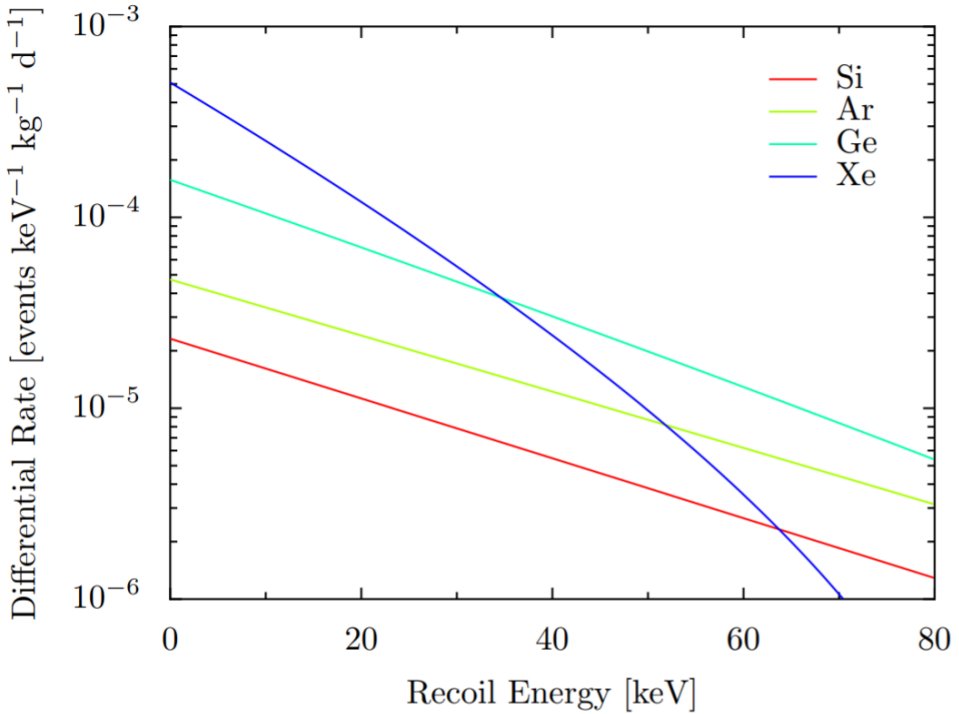


FIGURE 1.9. Expected differential recoil spectra from WIMP-nucleon scattering in different target materials, for a WIMP mass of  $m_\chi = 100$  GeV, assuming SI cross section of  $\sigma_\chi = 10^{-44} \text{ cm}^2$

Assuming isotropic scattering the recoils are distributed uniformly in  $E_R$ , where  $0 \leq E_R \leq E_0 r$ ; therefore

$$(1.16) \quad \frac{dR}{dE_R} = \int_{E_{min}}^{E_{max}} \frac{1}{E_0 r} dR(E) = \frac{1}{E_0 r} \int_{v_{min}}^{v_{max}} \frac{\sigma^2}{v^2} dR(v),$$

where  $E_{min}$  is the smallest possible recoil energy and  $v_{min}$  is its corresponding velocity. For a more comprehensive treatment of the WIMP interaction rate see [46]. In Fig. 1.9, is an example of the interaction rate for various elements.

#### 1.4.1 WIMP Nucleus Interaction Cross Section

WIMPs are charged under  $SU(2)_{weak}$ , hence they will interact with matter via weak-interactions. The cross section for zero momentum transfer is traditionally modeled as:  $\sigma_0 = 4G_F^2 \mu_N^2 C$ , where  $G_F = 1.1 \times 10^{-5} \text{ GeV}/(\hbar c)^3$  is the Fermi constant,  $\mu_N$  is the WIMP-target reduced mass, and  $C$  is an enhancement factor which is determined by the nature of the WIMP.  $C$  is different for different types of interactions. The *standard* interaction types treated in direct detection experiments are the spin-dependent (SD) and spin-independent (SI) which are reviewed in this section. For a discussion on other types of motivated interactions (e.g., spin-orbit) see Sec 1.5.

For the SI case the enhancement factor is modeled as:

$$(1.17) \quad C_{SI} = \frac{1}{\pi G_F^2} [Z f_p + (A - Z) f_n]^2,$$

where  $f_p$  and  $f_n$  are the effective WIMP-proton, WIMP-neutron coupling respectively. This type of interactions grows as  $A^2$ , and favors heavy targets. This type of interaction can appear due to isoscalar currents.

$$(1.18) \quad \mathcal{L} \supset \alpha_q^S \bar{\chi} \chi \bar{q} q + \alpha_q^V \bar{\chi} \gamma_\mu \chi \bar{q} \gamma^\mu q.$$

In the SD case, the scattering amplitude changes sign with the spin orientation; hence, only isotopes with odd number of protons or neutrons can be used for detection. The enhancement factor is modeled as:

$$(1.19) \quad C_{SD} = \frac{8}{\pi J} [a_p \langle S_p \rangle + a_n \langle s_n \rangle] J(J+1).$$

$a_p$  and  $a_n$  are the WIMP-proton and WIMP-neutron effective coupling respectively,  $\langle S_p \rangle$  and  $\langle S_n \rangle$  are the proton and neutron spin, and  $J$  is the total nuclear spin. This type of interaction can appear due to isovector currents such as:

$$(1.20) \quad \mathcal{L} \supset \alpha_q (\bar{\chi} \gamma_\mu \gamma_5 \chi) (\bar{q} \gamma^\mu \gamma_5 q)$$

### 1.4.2 Form Factors

At high momentum transfer, the inverse nuclear size becomes comparable to the momentum transfer (few hundred keVs), causing the cross section to drop due to the loss of coherence. To account for this effect, nuclear form factors, which are essentially the Fourier transform of the nucleon density function are introduced ( $F(q)$ ). Usually the form factors are parametrized as a function of the dimensionless quantity  $qr_n$ , where  $r_n$  is the nuclear radius. The cross section can be separated into two parts:

$$(1.21) \quad \sigma(qr_n) = \sigma_0 F^2(qr_n),$$

where  $\sigma_0$  is the zero-momentum transfer cross section, and  $F(qr_n)$  is the form factor, containing all momentum-transfer dependency. Much study has been conducted on the exact parametrization of the form factors [47]; however for low momentum transfer the effect of the different parametrization is negligible.

Finally the total event rate as a function of recoil-energy is given by:

$$(1.22) \quad \frac{dR}{dE_R} = \frac{\rho_\chi}{M_T M_\chi} \int_{v > v_{min}}^{v_{esc}} d^3v \cdot \frac{d\sigma_i}{dE_R} \cdot F_i^2(q^2) f(v, v_E) v$$

Where the astrophysical input are incorporated in the first and last terms. The particle and nuclear physics is incorporated in the  $\sigma_i$  and  $F_i^2(q^2)$  are the the cross section and form factor for interaction type  $i$  respectively.

## 1.5 Effective Field Theory Approach for WIMP-Nucleolus Scattering

The traditional approach for calculating the WIMP-nucleon scattering rate, has been to take only leading-order terms in a WIMP-nucleon effective field theory (EFT) with a very simple treatment of nuclear structure (as explained in Sec. 1.4.1). This leads to two main types of interactions, which are commonly labelled SI and SD. However, in recent years many authors have pointed out that in certain theories these interactions may be suppressed or nonexistent, and that otherwise subleading interactions may dominate the scattering process [48]. To account for this possibility in a systematic way, a more sophisticated EFT approach has been developed [49–51]. In the new approach, an effective Lagrangian describing the WIMP-nucleus interaction is constructed, taking into account all Galilean-invariant operators up to second order in the momentum exchange. This framework introduces new operators associated with different types of nuclear responses, along with the standard SI and SD ones, resulting in a set of 14 operators  $\mathcal{O}_i$  which may couple independently to protons and neutrons. In Eqs. (1.23) I list these operators following the convention from [50]. The operators depend explicitly on four linearly independent quantities:  $\vec{v}_{elast}^\perp \equiv \vec{v} + \frac{\vec{q}}{2\mu_N}$ ; the relative perpendicular velocity between the WIMP and the nucleon;  $\vec{q}$ , the momentum transferred in the scattering event; and  $\vec{S}_\chi$  and  $\vec{S}_N$ , the WIMP and nucleon spins.  $\mathcal{O}_2$  is not considered here as it cannot be obtained from a relativistic operator at leading order.

$$\begin{aligned}
\mathcal{O}_1 &= 1_\chi 1_N & \mathcal{O}_9 &= i\vec{S}_\chi \cdot (\vec{S}_N \times \frac{\vec{q}}{m_N}) \\
\mathcal{O}_3 &= i\vec{S}_N \cdot (\frac{\vec{q}}{m_N} \times \vec{v}_{el}^\perp) & \mathcal{O}_{10} &= i\vec{S}_N \cdot (\frac{\vec{q}}{m_N}) \\
\mathcal{O}_4 &= \vec{S}_\chi \cdot \vec{S}_N & \mathcal{O}_{11} &= i\vec{S}_\chi \cdot (\frac{\vec{q}}{m_N}) \\
\mathcal{O}_5 &= i\vec{S}_\chi \cdot (\frac{\vec{q}}{m_N} \times \vec{v}_{el}^\perp) & \mathcal{O}_{12} &= \vec{S}_\chi \cdot (\vec{S}_N \times \vec{v}_{el}^\perp) \\
\mathcal{O}_6 &= (\vec{S}_\chi \cdot \frac{\vec{q}}{m_N})(\vec{S}_N \cdot \frac{\vec{q}}{m_N}) & \mathcal{O}_{13} &= i(\vec{S}_\chi \cdot \vec{v}_{el}^\perp)(\vec{S}_N \cdot \frac{\vec{q}}{m_N}) \\
\mathcal{O}_7 &= \vec{S}_N \cdot \vec{v}_{el}^\perp & \mathcal{O}_{14} &= i(\vec{S}_\chi \cdot \frac{\vec{q}}{m_N})(\vec{S}_N \cdot \vec{v}_{el}^\perp) \\
\mathcal{O}_8 &= \vec{S}_\chi \cdot \vec{v}_{el}^\perp & \mathcal{O}_{15} &= -(\vec{S}_\chi \cdot \frac{\vec{q}}{m_N}) \left[ (\vec{S}_N \times \vec{v}_{el}^\perp) \cdot \frac{\vec{q}}{m_N} \right]
\end{aligned} \tag{1.23}$$

Unlike the commonly studied types of interaction (SI and SD), which are not suppressed when  $\vec{q} \rightarrow 0$  and for which the scattering rate on nucleons is expected to be largest for low energy nuclear recoils, some of the new EFT operators depend explicitly on  $\vec{q}$  and so their interaction cross section is suppressed for low momentum transfers. Consequently, their scattering rate peaks at nonzero nuclear recoil energy. For sufficiently high WIMP masses, this may occur above typical analysis energy range, which usually have an upper range of around 43 keV<sub>nr</sub> (nuclear

recoil equivalent energy) since they are designed to search the exponentially falling recoil spectra expected for SI and SD interactions (see Fig. 2.1). High energy nuclear recoils (NR), therefore, remain unexplored in many experiments.

Another typical assumption that can be relaxed is that WIMPs should scatter elastically with nuclei. There are dark matter models in which the incoming and outgoing WIMPs have different mass states [39] separated by a keV-scale splitting. In the case where the outgoing state is more massive than the incoming state, the cross section for low recoil energies can again be suppressed, this time by scattering kinematics. Recently an inelastic adaptation of the EFT operator framework discussed above was developed [52]. In this case the operators presented in Eqs. 1.23 are modified such that  $\vec{v}_{inelastic}^\perp = \vec{v}_{elastic}^\perp + \frac{\delta_m}{|\vec{q}|^2} \vec{q}$ , where  $\delta_m$  = is the mass splitting of the two WIMP states. In this paradigm the minimum momentum transfer for an interaction to occur is given by:

$$(1.24) \quad v_{min}/c = \frac{1}{\sqrt{2m_N E_R}} \left| \frac{m_N E_R}{\mu_N} + \delta_m \right|,$$

where  $\mu_N$  is the WIMP-nucleon reduced mass.

## 1.6 Direct Detection Strategies

The expected WIMP interaction flux and interaction types and rates, as well as the expected flux (explained above) are used as to design any instrument aiming at the detection of WIMP scattering from a target nuclei (direct detection). The detector must have a low threshold for NR O(1-10) keV as most WIMP paradigm yields an exponential decay of the recoil spectrum. Hence a lower threshold yields a large increase in sensitivity. The expected total interaction rate in a detector is very low; therefore the detector should have low background.

The main background source for WIMP detection is in the form of ER, and can be divided into two: external and internal background. External background refers to any particle entering the detector from outside and interacting within the detector.  $\gamma$  and  $\mu$  are the main types of particle which can penetrate the detector. Internal background refers to radioactive isotopes of the detector materials ( $^{39}\text{Ar}$ ) or impurities ( $^{222}\text{Rn}$  and  $^{85}\text{Kr}$ ). In addition neutrons or neutrinos can also induce NR background which is currently irreducible.

Many efforts are devoted for reducing ER background, focusing on decreasing the radioactive contaminations, in addition to stating the detector in a low background environment. Most detectors are situated in an underground facility to reduce muon flux from cosmic rays (see Fig. 1.10). Additionally, if the detector has the ability to discriminate between NR (signal) and ER (background) it will increase its detection sensitivity, as most background comes from  $\gamma$ -rays and  $\beta$  decays will be rejected. Because the event rate grows with target volume, the larger the number of nuclei is, the larger is the detector sensitivity, this can compensate for bigger background rates. Finally would the detector have the ability to identify special features of

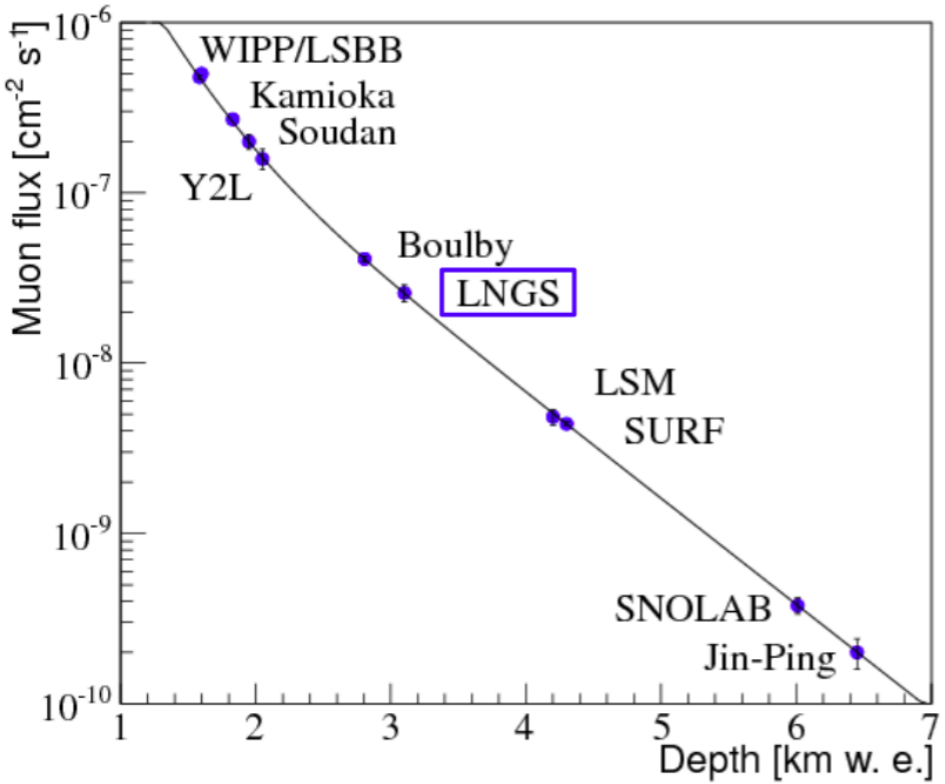


FIGURE 1.10. The muon flux as a function of underground facility depth measured in km water equivalent. LNGS which hosts the XENON experiments is highlighted.

WIMPs such as interaction types, and the directionality of the incoming WIMP, it will have a clearer signature of WIMP detection.

The energy deposited in a material by any interacting particle, can be measured by three excitation channels: scintillation, ionization, and heat (phonons). Different detectors use different excitation channels; scintillators based experiments use light detectors to detect the scintillation lights (e.g., DAMA/LIBRE), Germanium based detectors usually use the ionization channel (e.g., CoGeNT) and superconductor based experiment detect heat (e.g., CRESST). Most leading experiments measure two of the excitation channel (e.g., XENON measuring scintillation and ionization). The measurement of two excitation channels gives a better ability to discriminate signal to background. The discrimination parameter is usually the ratio between the two channels.

Past and present representative experiments of WIMP direct detection and the detection method they use are shown in Fig. 1.11. In the next section I focused on Liquid-Noble detectors, mainly on XENON based detectors.

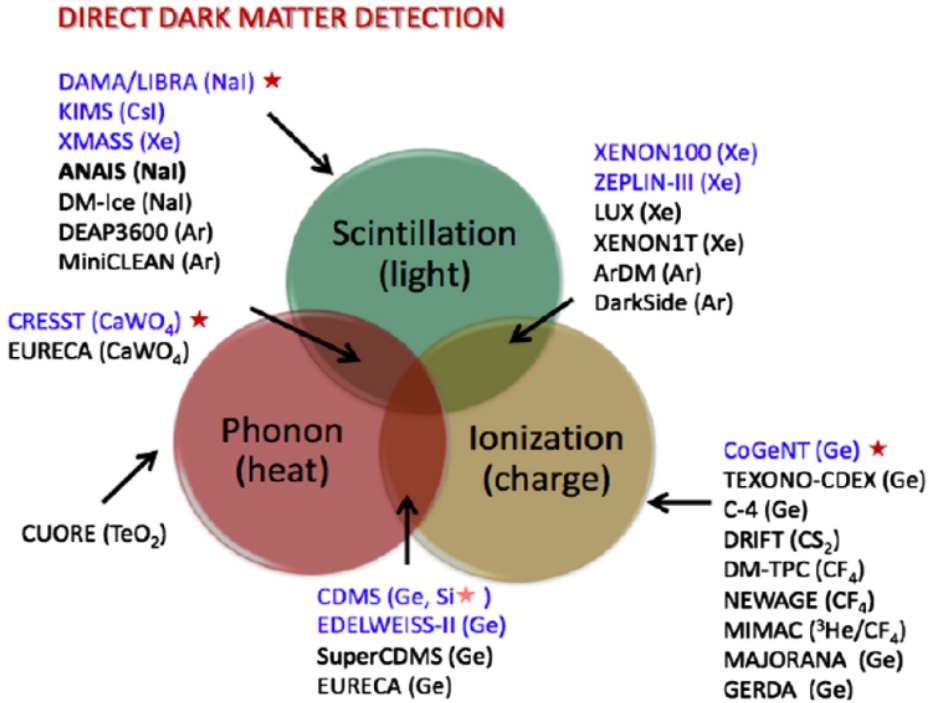


FIGURE 1.11. Direct detection experiments classified by their detection strategies.

## 1.7 Nobel Liquid Detectors

The most sensitive DM direct detection detectors currently are based on Liquid Noble elements, mainly Xenon and Argon. The excitation channels these detectors utilize are the scintillation and ionization. The strategy these detectors exploit for lowering the background rates is the self-shielding of the target materials. PMT arrays deployed in the liquid xenon (LXe) or liquid argon (LAr) detects the photons from the scintillation. Extracting the ionization electrons using an electric field allows ionization measurement. The ionization to scintillation ratio and the pulse shape can be used as discriminator parameters between signal (NR) and background (ER). The low concentration of radioactive isotopes results in an inner volume practically free of electromagnetic background. Liquid noble detectors are divided into two; liquid only detectors (single phase) and liquid and gas detectors (dual phase).

### 1.7.1 Single Phase Detectors

Single phase detectors fully exploit the self-shielding properties of LXe and LAr to create a low background inner volume. These experiment usually relay on light detectors immersed in the liquid target. The position reconstruction of an interaction is obtained by the observed light hit pattern and its resolution depends on the photodetector size. The main advantage of

these detectors is their simplicity. Since no ionization measure is used, the complexity in adding high voltage and cathode-anode-grid systems is avoided. The main disadvantage is that less information is known about each interaction event and the discrimination between ER and NR is less efficient.

An example of a single phase LXe detectors is the XMASS detector, positioned in the Kamioka observatory in Japan. It is a spherical detector holding 830 kg of LXe surrounded by 642 PMTs. The detector is deployed in a 10 ton water tank to reduce background. XMASS have excluded a cross section of  $1.5 \times 10^{-43} \text{ cm}^2$  for a 100 GeV WIMP with an exposure of 292 days [53]. An example for future LAr single phase detector is the DEAP experiment located in SNOLab underground facility. The LAr pulse shape discrimination that will be used to enhance the expected sensitivity. The detector is expected to hold more than 1-tonne of LAr with background expectation of less than 0.3 event/year.

### 1.7.2 Dual Phase Detectors

Dual phase detectors rely on time projection chamber (TPC) technique, exploiting both scintillation and ionization channels. The scintillation photons are detected like in the single phase detectors usually using PMTs. The ionization electrons drifts in the liquid due to an external electric field and extracted to the gas phase using a stronger electric field, and generate proportional scintillation. The ratio of the two signals is used as a discriminator parameter, as ER produces a higher ionization signal compared to NR. A full 3D position reconstruction is achieved using the hit pattern of the proportional scintillation and the time difference between the two signals. A more detailed description of the XENON experiment TPC can be found in 1.9.

The leading dual phase LXe collaborations are LUX [54] PANDAX [55] and XENON1T [56]. Currently XENON1T sets the most stringent limit for the SI interaction [5]. LAr have an additional advantage using pulse shape discrimination techniques. The main disadvantage of LAr is the low PMT efficiency for argon scintillation light. The most common way to increase the detection efficiency is by coating the PMT with a wavelength shifter. Amongst the leading LAr programs are WArP [57], ArDM [58], and DarkSide [59].

## 1.8 Non Linear Emission of Radiation in Liquid Xenon

As explained in Sec. 1.6, in LXe and LAr based experiments the exact properties (time and spatial) of the scintillation and ionization responses to all types of interaction must be well quantified and understood. Mainly, much research has been focused on the scintillation and ionization responses of LXe to events with recoil energy as low as  $\sim 10 \text{ keV}$  [60–63]. Specifically the reconstruction of the directionality of recoil nuclei or electrons is of great interest to DM direct detection experiments. Better understanding of these properties may help to reduce background

dramatically, both by detecting the direction of the incoming particle, and by better discriminating ER and NR.

A particle interacting within the LXe media, forms a cloud of excited and ionized states with typical length of 100 nm. The excited Xe ( $Xe^*$ ) combines with other Xe atoms to form an excited dimer state (excimer) when they decay to ground state they emit light.



The electrons emitted from the ionization can recombine with a surrounding atom, this process of recombination provides another possibility to produce excimers,



Once  $Xe^*$  is produced it adds to the scintillation process explained in 1.25. There are two types of  $Xe_2^*$  excimer states, singlet and triplet, with lifetime of  $\sim 3$  ns and  $\sim 25$  ns respectively. The wavelength emitted by these states is between (175-180) nm which is lower than the lowest excitation of xenon, and therefore travel through it to reach a photo-detector situated outside the LXe. In LAr the same process happens however the lifetime of the singlet ( $\sim 7$  ns) and triplet( $\sim 1600$  ns) are different. Because the ratio of singlets to triplets is different for ER and NR this is used for better discrimination ("pulse shape discrimination") [64].

Several existing and proposed experiments such as DRIFT-II [65], DMTPC [66], NEWAGE [67] and MIMAC [68], exploit recoil direction properties. These experiments are using dilute gas in which the ionization tracks extend to a few millimeters. However, in LXe the track length is estimated to be  $O(100\text{nm})$ . Moreover the topology of the excimers clouds is represented by a complex structure of branches which are formed by secondary recoils [69]. These two different properties, track length and structure, makes it highly difficult if not impossible to construct directionality in a LXe experiment. Therefore, a different approach for directionality measurement needs to be adopted for DM LXe based experiments.

The phenomena of an isolated particle in an excited state undergoing a transition to its ground state (i.e. spontaneous decay) as a result of the vacuum electromagnetic field is well described in the theory of quantum electrodynamics. This theory is applicable for an ensemble of particles only when the particles interact with the vacuum electromagnetic field separately. In this case the time distribution of emitted light will follow an exponential law. The characteristic time,  $\tau_{sp}$ , of a single particle to radiate is equal to the reciprocal of the transition rate  $\Gamma$  from the initially excited level. The radiation pattern in this case is isotropic in its nature, see Fig. 1.12a.

These radiation properties are significantly different when the radiating particles are dense enough. In this case the collective radiation from the ensemble is different than the sum of

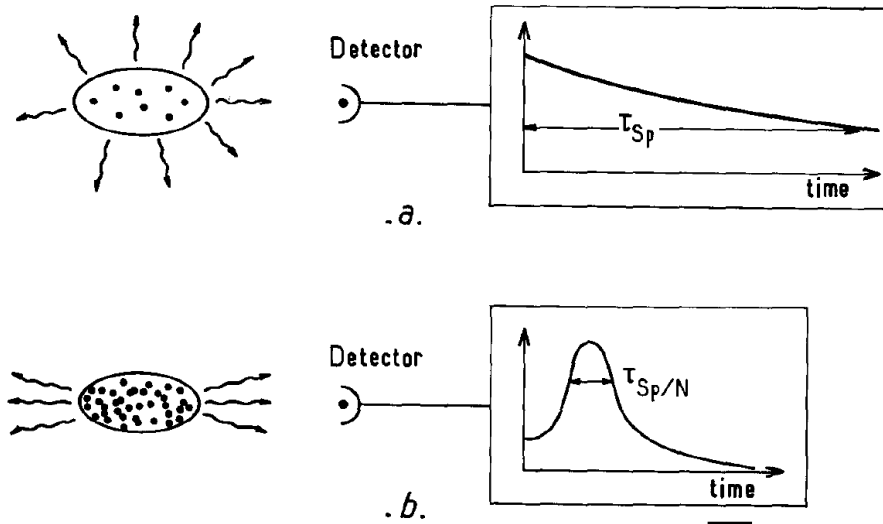


FIGURE 1.12. Comparison between ordinary fluorescence and superradiance. (a) In ordinary fluorescence, where each atom (or molecule) interacts independently with the vacuum electromagnetic field, the intensity decays exponentially (with time constant  $\tau_{sp}$ ), with an isotropic directional distribution. (b) Superradiance is highly directional and its duration is of order  $\tau_{sp}/N$ , where  $N$  is the number of radiators in the sample. Figure from [72]

all particles radiating. This phenomena was first postulated by Dicke [70] in 1954 and was first measured in Xe by Rosenberger in 1965 [71]. In his research the radiation decay time from a two level atomic system was considered and expected to be dependent on the number of radiating particles  $N$ . This type of emission is referred as superradiance. This phenomena is due to interaction of the radiating particles with each other via a common electromagnetic radiation field, which results in a correlation between the atomic dipole moment. This correlation leads to a macroscopic optical polarization proportional to  $N$ . Hence the radiation intensity is proportional to  $N^2$ , leading to a pulsed radiation with duration proportional to  $1/N$ , see Fig 1.12b. The phenomena of superradiance has been studied extensively since see [72, 73]

An effective self-induction of correlations between dipole moments is a necessary condition for a particles to exhibit a *superradiance* emission. The conditions for this to occur are very different than the ones of regular fluorescence. The characteristic time of *superradiance* emission to happen,  $\tau_c \sim 1/N$  must be shorter the relaxation time of the atomic dipole moment,  $\tau_d$ . It also has to be shorter then  $\tau_{sp}$ , however in most cases,  $\tau_d$  is smaller than  $\tau_{sp}$ , hence this is a more stringent condition. Notice that unlike inverse population that happens in lasers, which occurs due to an external "pump", the correlation build-up between the radiating particles in *superradiance* happens spontaneously in the course of emission process.

The *superradiance* emission pattern depends greatly on the geometrical configuration of the

atomic system. The relevant quantities affecting the different behaviors are the de-excitation wavelength ( $\lambda$ ) and linear the size of the system ( $L$ ). There are three different scenarios:  $L^3 \ll \lambda^3$ ;  $L \gtrsim \lambda$ ;  $L \gg \lambda$ . In the first case, a system of radiating particles with linear size much smaller than the wavelength, the system will emit a pulse in an arbitrary direction with a maximal intensity of  $I \sim N^2$ . In the second case the linear size of the system is comparable to the wavelength, however the distance between 2 radiating particles is still smaller than the wavelength, the system will emit most of its energy into a small solid angle in the direction of the greater dimension of the system. This directionality is caused by the growing interference of the emitted photons. The particles will start emitting isotropic spontaneous emission, and gradually will grow correlations between the atomic dipole via the radiation field. The third case is the case of classical standard emission.

## 1.9 The XENON Program

The XENON program for DM searches, is a phases program using LXe detectors to measure the scattering of DM of xenon nuclei. In each phase the mass of the detector increase by roughly an order of magnitude, starting from 10 kg in the first phase, and ending with 7 tonne in the last. The program operates the detectors at the Laboratori Nazionali del Gran Sasso (LNGS) in Italy. Under an average depth of 3600 m water equivalent, the cosmic muon flux is suppressed by six orders of magnitude with respect to sea level (see Fig. 1.10). The time line for all phases, as well as their properties and sensitivities are presented in Fig. 1.13.

The XENON detectors are dual phase (liquid-gas) TPCs, with simultaneous detection of the Xe scintillation light (S1) at the few keV level, and ionization (S2) at the single electron level. The ratio S2/S1 produced by a WIMP (or neutron) interaction is different from that produced by an electromagnetic interaction, allowing a very efficient particle identification.

The ultra low background has been achieved by: careful selection of the materials; the xenon self-shielding capabilities as well as water shielding in advance phases; and selecting data only from a fiducial volume (FV) located at the center of the detector.

A short summary on each phase and its upgrade from previous phase is presented here, the main concepts of the XENON TPC are explained using XENON100 as an example in Sec. 1.9.2.

### 1.9.1 XENON10

The first phase was the XENON10 detector a cylinder  $\sim 20$  cm diameter and 20 cm length, holding 25 kg of xenon (10 kg in the FV). The detector was operating mainly as a prototype for the larger detectors to come. It was operating between the years 2005 and 2007, achieving an exclusion limit of  $\sigma_{SI} = 8.8 \times 10^{-44} \text{ cm}^2$  for a 50 GeV WIMP [74].

	XENON10	XENON100	XENON1T	XENONnT
Era				
Mass	25 kg	161 kg	3200 kg	~8000 kg
Drift	15 cm	30 cm	100 cm	144 cm
Status	Achieved (2007)	Achieved (2016)	Projected (2018)	Projected (2023)
$\sigma_{SI}$ Limit ( $\text{@} 50 \text{ GeV/c}^2$ )	$8.8 \times 10^{-44} \text{ cm}^2$	$1.1 \times 10^{-45} \text{ cm}^2$	$1.6 \times 10^{-47} \text{ cm}^2$	$1.6 \times 10^{-48} \text{ cm}^2$

FIGURE 1.13. The timeline of the four phases of the XENON program

### 1.9.2 XENON100

The second phase was the XENON100 detector a cylindrical  $\sim 40$  cm diameter and 40 cm length hosting 161 kg of LXe, of which 62 kg function as the active target and 34 kg as the FV. The detector uses of a total of 178 1-inch square Hamamatsu R8520-AL PMTs employed in two arrays, one in the gas phase at the top of the TPC, and the other at the bottom, immersed in the LXe [75].

A particle interacting with the LXe deposits energy that creates both prompt scintillation (S1) and delayed proportional scintillation (S2) both finally producing vacuum ultra violet (VUV) 178 nm photons. The photons are detected using the two PMT arrays. The S2 signal is produced by ionization electrons, drifted in an electric field of 530V/cm towards the liquid-gas interface, where they are extracted to the gas phase using a stronger electric field of  $\sim 12$ kV/cm in which the proportional scintillation occurs. The spatial distribution of the S2 signal on the top PMT array, together with the time difference between S1 and S2 signals, provide respectively  $x$ - $y$  and  $z$  position information for each interaction, allowing 3D position reconstruction to be achieved.

Interaction in different locations of the detector have different signatures. In order to take these effects into account, a correction is applied based on light and charge collection efficiency maps. These maps are prepared using calibration sources ranging up to energies well above 240 keV<sub>nr</sub>. The corrected signals (cS1,cS2) are spatially independent and uniform to all interactions [75]. Note that some of the top PMTs saturate for large S2 signals and therefore in most analysis only the bottom PMT array is used to infer the energy scale in S2. A schematic of the detection principle is shown in Fig 1.14

The detector has been operating between the years 2008 and 2016, achieving an exclusion limit of  $\sigma_{SI} = 1.1 \times 10^{-45}$  for a 50 GeV WIMP [4]. Additionally XENON100 excluded many

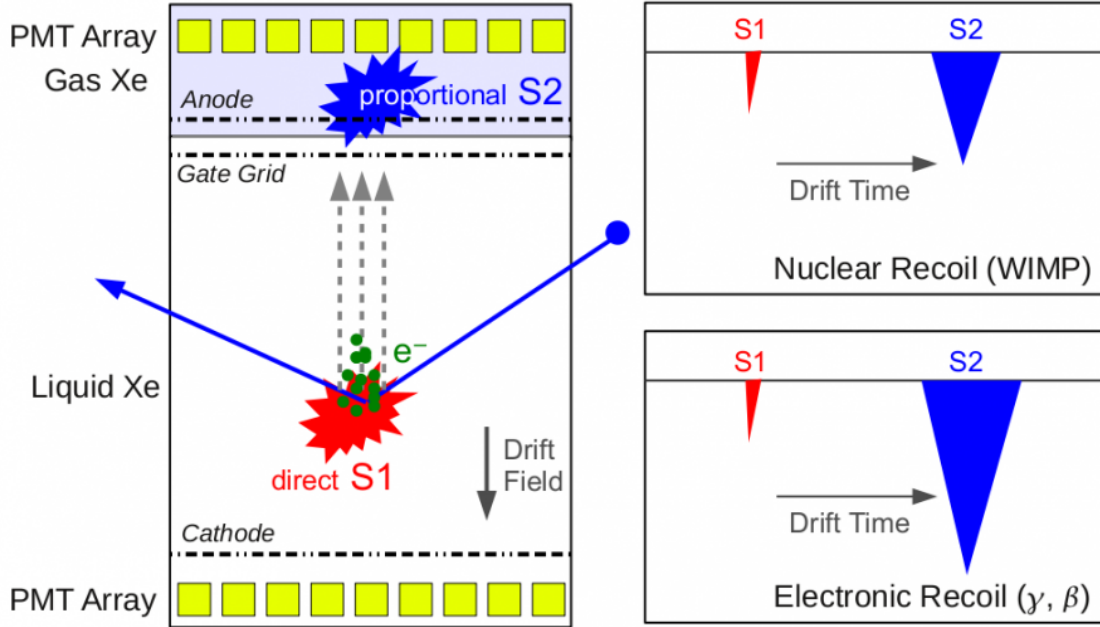


FIGURE 1.14. Operational principle of the XENON TPC. The ratio  $S_2/S_1$  provides separation between nuclear and electromagnetic recoils.

interpretation trying to explain the tension with DAMA/LIBRE observation results. In Chapter 2 I present an analysis done on the XENON100 data considering the EFT approach for high energy recoils [76].

### 1.9.3 XENON1T

The third phase of the XENON program is the XENON1T detector [56]. This detector is the first ton scale dual phase TPC DM detector. It has been fully operating since 2016. The XENON1T TPC contains  $\sim 3$  tons of LXe (1 ton in the FV) and has achieved the lowest background rate in DM detectors. The low level of background is achieved by carefully selecting low radioactive materials, and by deploying the TPC inside a 10 meters high, 10 meters diameter cylindrical water tank, which acts as an active cosmic muon veto and as a passive neutron shield. A view of XENON1T is shown in Fig 1.16.

The first science run had an exposure of 1 month, achieving the most stringent exclusion limit to date with a minimum of  $7.7 \times 10^{-47} \text{ cm}^2$  for a 35 GeV WIMP, the full limit is shown in Fig. 1.16. In Chap. 4, is a description of the calibration system of XENON1T.



FIGURE 1.15. A picture of the XENON1T detector(left) and its control room (right)

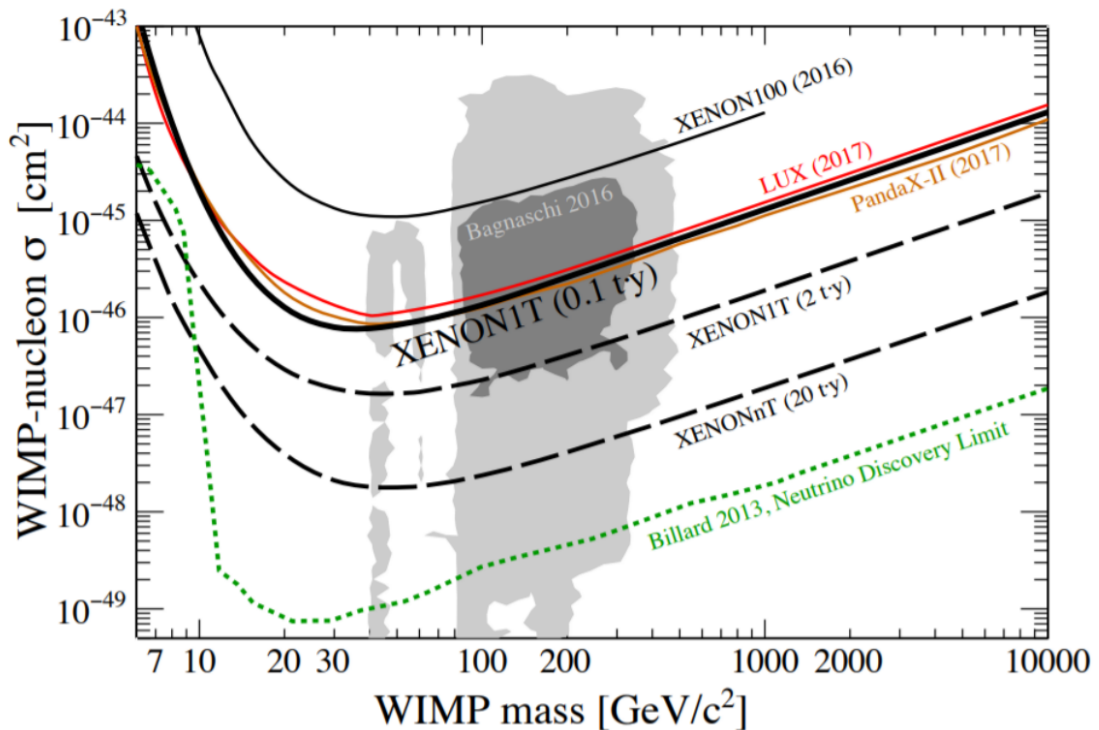


FIGURE 1.16. The spin-independent WIMP-nucleon cross section limits for first run of XENON1T LUX and XENON100 final results, and projected sensitivities for XENON1T and XENONnT future data. level.

#### 1.9.4 XENONnT

The fourth phase of the XENON program is the XENONnT detector. Unlike other phases, this phase will be integrated inside the infrastructure of its ancestor XENON1T. The main upgrade will be the replacement of the inner vessel of XENON1T to a larger vessel which contains roughly  $\sim 8$  ton of LXe. The projected sensitivity of XENONnT is estimated to be  $1.6 \times 10^{-48} \text{ cm}^2$



## EFFECTIVE FIELD THEORY SEARCH FOR HIGH ENERGY NUCLEAR RECOILS IN XENON100 DETECTOR

Standard SI,SD analysis concentrate on energy recoils of up to  $O(10)$  keV<sub>nr</sub>, hence a hard high energy threshold is used for them. In XENON100 this threshold value is 43 keV<sub>nr</sub>. However SI and SD are not the only types of interactions possible. These new interactions which predicts higher recoil energies are considered in the EFT framework (see 1.5). moreover a WIMP may have several mass states, which will also result in a possible higher energy recoil. In Fig. 2.1 is an example of an expected recoil spectrum from different operators.

The EFT framework of [49] is constructed at the WIMP-nucleon level and so each operator may be present independently for protons and neutrons, though UV models can of course correlate their couplings. The full EFT thus has 28 coupling parameters in addition to the WIMP mass, plus a mass splitting  $\delta$  in the inelastic case. This parameter space is too large to explore in full, so a similar approach to the SI/SD case is taken, assuming only one active operator at a time, considering it equally coupled to protons and neutrons (the “isoscalar” case).

To facilitate the full exploitation of these results by the community, I provide in supplementary material a set of tools for converting any theoretical recoil spectrum  $dR/dE$  into an accurate event rate prediction for this analysis, including all detector response and analysis efficiency effects. This may help to set a mildly conservative but quite accurate limit on arbitrary models in the full EFT parameter space, or any other particle dark matter model for which one can supply the expected recoil spectrum. These tools are described further in Appendix A.

In this work I reanalyze science run II data recorded between February 2011 and March 2012, corresponding to 224.6 live days. The characterization of the detector response to ER interactions is performed using dedicated calibration campaigns with  $^{60}\text{Co}$  and  $^{232}\text{Th}$  radioactive sources, while the response to NR interactions is performed using  $^{241}\text{AmBe}$  neutron source calibration

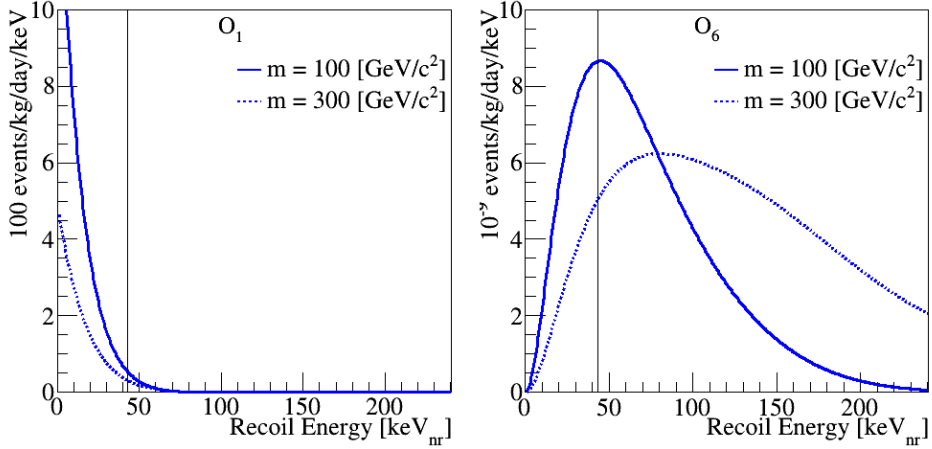


FIGURE 2.1. Example EFT recoil spectra for elastic scattering of spin-1/2 WIMPs on Xenon nuclei (weighted according to the isotope abundances in the XENON100 experiment). Left(right) shows the predicted spectra for EFT operator  $\mathcal{O}_1(\mathcal{O}_6)$ . The normalization is controlled by the coupling coefficient of each EFT operator and the experimental exposure. The solid vertical line at 43 keV<sub>nr</sub> shows the approximate division between the two signal regions used in this analysis. As shown, the standard SI ( $\mathcal{O}_1$ ) spectrum is concentrated mainly in the already explored energy region. However, some EFT operators, for certain WIMP masses, predict a significant fraction of recoil events above the upper energy cut used in the standard SI analysis, motivating an extension of this cut. The highest recoil energy shown in the plots, 240 keV<sub>nr</sub>, roughly corresponds to the highest energy accounted for this analysis.

campaigns.

This work extends the previous results [4, 77], referred to in the following as the low-energy channel, with a new study exploring the recoil energy range between (43 – 240) keV<sub>nr</sub>. The data analysis is divided into two mutually exclusive channels, one optimized for low energies and ranging from (3 – 30) PE in cS1 (low-energy), and the other optimized for high energies recoils ranging from (30 – 180) PE in cS1 (high-energy). These two analyses are then combined statistically.

## 2.1 Low Energy Channel

This analysis channel relies on the reanalysis of run II data described in [4]. The region of interest (ROI), background expectation models, data selections and their acceptances are mostly unchanged and so are only briefly summarized here. Differences with respect to said results are highlighted when present.

The ROI for this channel is defined in the  $(\log(cS2_b/cS1), cS1)$ -plane and is shown in Fig. 2.2. The lower bound on  $\log(cS2_b/cS1)$  corresponds to a  $3\sigma$  acceptance quantile (as a function of cS1)

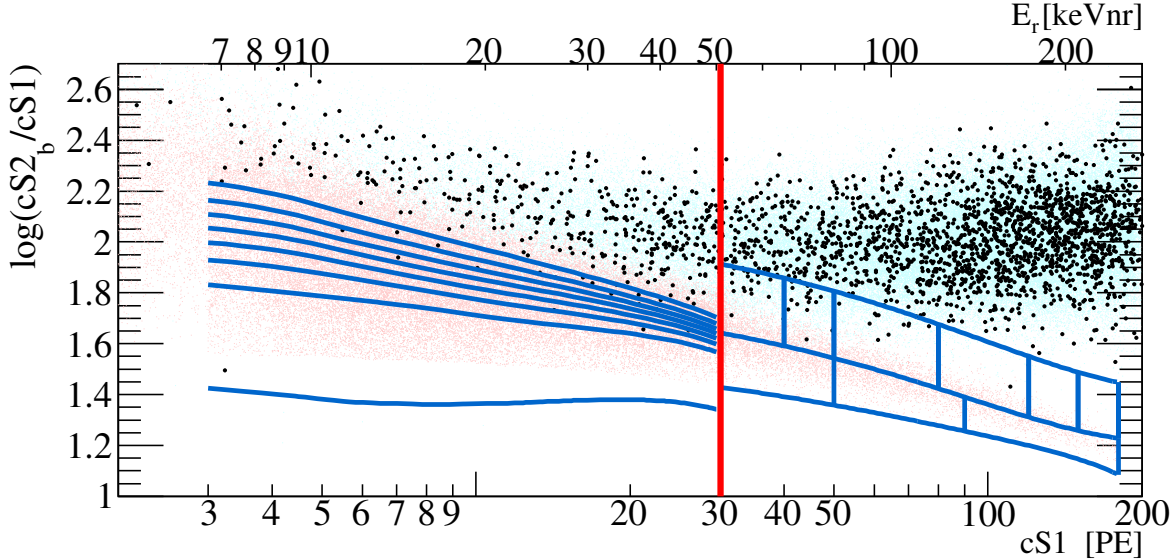


**FIGURE 2.2.** Summary of regions of interest, backgrounds, and observed data. ER calibration data, namely  $^{60}\text{Co}$  and  $^{232}\text{Th}$  data are shown as light cyan dots. NR calibration data ( $^{241}\text{AmBe}$ ) are shown as light red dots. Dark matter search data is shown as black dots. The red line is the threshold between the low- and high-energy channels. The lines in blue are the bands. For the low-energy channel, the bands are constructed to achieve constant expected signal density, and are operator and mass dependent, shown here for a  $50 \text{ GeV}/c^2$  WIMP using the  $\mathcal{O}_1$  operator. For the high-energy region, the nine analysis bins are presented also in blue lines.

of a 20 GeV WIMP mass signal model assuming an  $\mathcal{O}_1$  (SI) interaction, while the upper bound is fixed at  $\log(cS2_b/cS1) = 2.7$ . The range in  $cS1$  is selected as  $(3 - 30)$  PE. The ROI is further divided into eight subregions (also called bands) depending on the operator  $\mathcal{O}_i$  and on the WIMP mass hypothesis. These bands are arranged to achieve constant expected signal density in each region, as described in [4].

Other than falling into the ROI, an event should fulfill several additional selection criteria (cuts). Data quality and selection cuts are defined to remove events with poor data quality or noisy signals. Events are discarded if they present a time-coincident signal in the outer LXe veto, S2 signals below threshold, multiple-scatters, or are localized outside a predefined fiducial volume of 34 kg. In addition, this analysis channel uses the postunblinding cuts and data reprocessing described in [4]. More details on these selection criteria and their relative WIMP signals acceptances can be found in [4, 78].

Note that this analysis channel does not employ a variable lower  $S1$  threshold as a function of the event position in the TPC but instead applies a fixed lower threshold cut on  $cS1$  at 3 PE, conversely to the choice made in [4].

The expected background is modeled separately for ER and NR contributions which are

then scaled to exposure and added together. The NR background is estimated by Monte Carlo simulation and accounts for the radiogenic and cosmogenic neutron contributions [79]. The ER background is parametrized as the linear combination of Gaussian-shaped and non-Gaussian components. The former is obtained via a parametric fit of the  $^{60}\text{Co}$  and  $^{232}\text{Th}$  calibration data, as discussed in [77].

The latter, which consist of anomalous events such as those presenting incomplete charge collection or accidental coincidence of uncorrelated S1s and S2s, is evaluated via dedicated techniques described in [4].

Systematic uncertainties on the background model arising from the Gaussian parametrized fit, and from the normalizations of the NR and non-Gaussian components, have been evaluated and propagated to each band. These errors are small with respect to the statistical uncertainties of each band, which are conservatively taken as the overall uncertainty [4], as discussed in Sec. 2.4.

## 2.2 High Energy Channel

This analysis channel targets high-energy nuclear recoils and is the focus of this work. The data selection criteria used are based on the criteria described in detail in [78], which were optimized for high acceptance to low-energy nuclear recoils. Most of these cuts were found to be fully compatible with (or easily extended) to high energy depositions; however some required more comprehensive studies, which are described in the following .

The width of an S2 pulse increases with the depth ( $z$ ) of the interaction. This is due to the diffusion of the electron cloud during its propagation through the liquid xenon. Since low-energy S2 events show larger spread due to low statistics of drifted electrons, the cut was previously defined in an energy-dependent way. However, for the large recoil energies considered in this channel, this energy dependency is no longer valid. I therefore use here a cut on the S2 width which is a function of the depth of the interaction alone.

As a WIMP will interact only once in the detector, I remove events which have more than one S2. I adopt in this analysis a cut that is more suitable to higher energies and demand a single S2 in a  $160\ \mu\text{s}$  window, instead of a linear dependence between the second S2 size and the first.

To define the interaction's exact location in  $(x, y)$ , I use several algorithms, one of which is based on a neural network (NN) [78]. The NN was not trained to recognize high energy ER events, and therefore a cut on the NN reconstruction quality is not suitable for this analysis. I therefore discard this cut but keep all other selections on position reconstruction quality, which is sufficient to ensure a correct position reconstruction.

The total acceptance to WIMP signals is computed based on  $^{241}\text{AmBe}$  calibration data as a function of cS1, following the procedure described in [78]. I present this function in Fig. 2.3, where the total acceptance is fitted using a third-order polynomial.

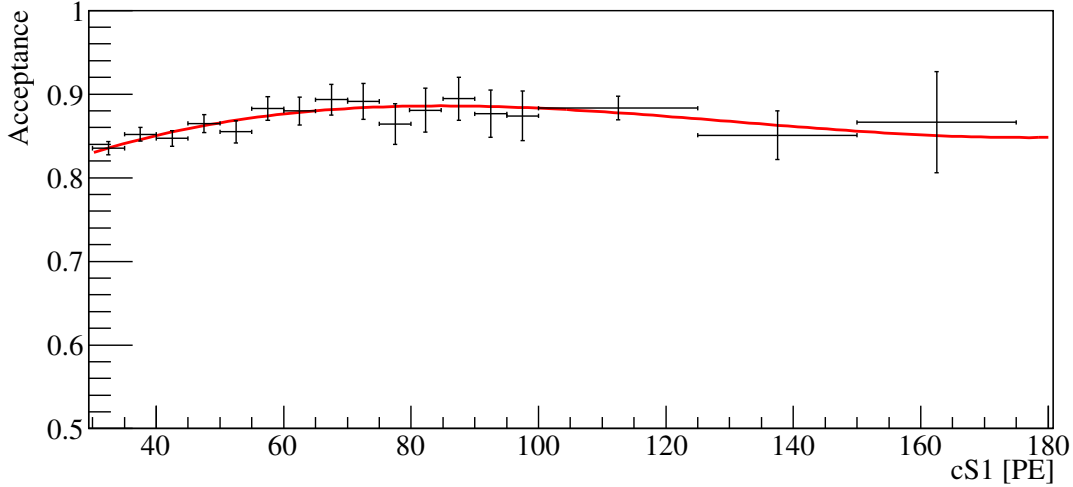


FIGURE 2.3. The total acceptance of all cuts used. Data from calibration are shown in black, with a third-order polynomial fit in red.

I define our signal region in the discrimination  $\log(cS2_b/cS1), cS1$ -plane using  $^{241}\text{AmBe}$  calibration data. The region of interest is shown in Fig. 2.2 as blue contour lines. The upper bound in  $\log(cS2_b/cS1)$  is defined such that the contribution due to xenon inelastic interaction lines is negligible. The lower bound is defined as the  $3\sigma$  acceptance quantile of the  $^{241}\text{AmBe}$  distribution.

I divide our signal region into two bands in  $\log(cS2_b/cS1)$ , constructed such that the  $^{241}\text{AmBe}$  data sample is equally distributed in between them. The number of events in each band is  $\sim 3000$ . The bands are further divided into nine bins, the number and boundaries of which have been optimized via Monte Carlo (MC) simulation. The definitions of the bins boundaries are presented in Table 2.1 and in Fig. 2.2.

The main source of background results from ER leakage. I therefore estimate the background distribution in the ROI using  $^{60}\text{Co}$  and  $^{232}\text{Th}$  calibration events. Contributions from radiogenic and cosmogenic neutrons, as well as accidental coincidence, are negligible for such a high energy recoil. In Table 2.1, I report the background expectation in the ROI along with the observed events for each bin. Here the background expectation is computed by scaling the calibration sample yield by  $6.54 \times 10^{-3}$ , which is the ratio of observed counts to calibration counts in an independent sideband. The sideband is defined above the upper limit of this analysis and below the ER calibration band mean. Note that in the computation of exclusion limits the background normalization is fitted to data, rather than using the sideband normalization, as described in Sec. 2.4.

#	Band	Energy range (cS1)	# Background events	# Observed events
1	upper	30 - 40	24±5	20
2	upper	40 - 50	16±3	17
3	upper	50 - 80	12±3	11
4	upper	80 - 120	1.1±0.3	1
5	upper	120 - 150	(1.0±0.5)×10 <sup>-1</sup>	1
6	upper	150 - 180	(0.8±0.4)×10 <sup>-1</sup>	0
7	lower	30 - 50	0.9±0.3	0
8	lower	50 - 90	(3.5±1.2)×10 <sup>-1</sup>	0
9	lower	90 - 180	(1.8±0.7)×10 <sup>-1</sup>	0

TABLE 2.1. Definitions and contents of the analysis bins for the high-energy channel.

The expected background counts are calculated by taking the calibration sample and scaling it by  $6.54 \times 10^{-3}$ , which is the ratio of observed counts to calibration counts in a sideband.

## 2.3 Signal model

The signal model is produced by taking a theoretical event rate spectrum, the production of which is described in Secs. 2.3.1 and 2.3.2, and applying the analysis acceptance and detector response as described in [78] to obtain the expected event rate in the detector in terms of detector variables (i.e. cS1 and cS2<sub>b</sub>). In both analysis channels, I use Eq. 2.1 in order to compute the expected average cS1 for a given NR energy,

$$(2.1) \quad \langle cS1 \rangle = E_{nr} \cdot (L_y \mathcal{L}_{eff}) \cdot \left( \frac{S_{nr}}{S_{ee}} \right)$$

where  $E_{nr}$  is the recoil energy,  $L_y$  is the average light yield in the detector,  $\mathcal{L}_{eff}$  is the scintillation efficiency relative to 122keV<sub>ee</sub> as a function of  $E_{nr}$ , and  $S_{ee}$  and  $S_{nr}$  are the quenching factors due to the externally applied electric field. Aside from  $E_{nr}$  and  $\mathcal{L}_{eff}$  these parameters have fixed values, namely  $L_y = 2.28 \pm 0.04$ ,  $S_{nr} = 0.95$ , and  $S_{ee} = 0.58$ . Recoils below 3 keV<sub>nr</sub> are assumed to produce no light. For details of the physics behind these parameters and the construction of the signal probability density function (PDF), see [4, 78].

For the low-energy region, the expected cS2<sub>b</sub> signal is computed following [80] using Eq. 2.2,

$$(2.2) \quad \langle cS2_b \rangle = E_{nr} \mathcal{Q}_y Y$$

where  $Y = 8.3 \pm 0.3$  is the amplification factor determined from the detector response to single electrons [81], and  $\mathcal{Q}_y$  is the charge yield as a function of  $E_{nr}$ . Applying the detector and PMT responses, and the acceptance as in [4], defines the low-energy signal model over the region 3 PE < cS1 < 30 PE, with cS2<sub>b</sub> > 73.5 PE as the S2 threshold.

Equation 2.2 hides a subtlety. The actual cS2<sub>b</sub> PDF is composed of two pieces, a Poisson term associated with the initial charge liberation and a Gaussian term associated with the PMT response and other detector effects:

$$(2.3) \quad p_{\text{S}2}(\text{cS2}_b|E) = \sum_{N'} P_{\text{pmt}}(\text{cS2}_b|YN', \sigma_Y \sqrt{N'}) \cdot \text{Pois}(N'|\mu_Q)$$

where  $\mu_Q = E_{\text{nr}} \mathcal{Q}_y$  is the expected number of liberated charges in a nuclear recoil event of energy  $E$ , and  $N'$  is the actual number of liberated charges. The amplification factor  $Y$  is applied to the actual number of liberated charges  $N'$ , not the expected number  $\mu_Q$ . Associated with this is the variance of the Gaussian response PDF,  $\sigma_Y \sqrt{N'}$ , where in this analysis  $\sigma_Y = 6.93$  as measured and described in [81].

For the high-energy region I cannot produce the S2 distribution in the same way as the method in [80], since it has not been calibrated for such high recoil energies. I therefore use the NR calibration data distribution in  $\log(\text{cS2}_b/\text{cS1})$  to estimate the WIMP distribution. Above 180 PE in cS1, the event yield of <sup>241</sup>AmBe data is too low to estimate the distribution accurately. This forms the upper bound of this analysis. With the cS2<sub>b</sub> distribution determined by this empirical method, I require only a prediction of the cS1 distribution. This is obtained from Eq. (2.1), followed by the application of detector and PMT responses, as well as the acceptance given in Fig. 2.3, which completes the high-energy signal model definition.

Figures 2.4 and 2.5 show signal distribution examples for two EFT operators and for the low and the high-energy region, respectively. In both cases, the signal distributions are normalized to yield five events in the total energy range (low-energy and high-energy).

### 2.3.1 Elastic scattering

The expected recoil energy spectrum of each WIMP mass for each EFT operator is calculated using the Mathematica package DMFormFactor supplied by Anand et al. [50, 51]. I use standard assumptions as in previous analyses (e.g [4]) regarding the local dark matter density and velocity distribution, namely  $\rho_{\text{local}} = 0.3 \text{ GeV}\cdot c^{-2}/\text{cm}^3$  and a Maxwell-Boltzman distribution with a mean given by the local circular velocity  $v_0 = 220 \text{ km/s}$  and cut off at an escape velocity of  $v_{\text{esc}} = 544 \text{ km/s}$ . The responses of xenon nuclei to a scattering event are computed from one-body density matrices provided with the package, in contrast to the Helm form factors which have been used in previous analyses. These spectra are produced for the seven most abundant xenon isotopes (128, 129, 130, 131, 132, 134 and 136), combined in proportion to the abundance of these isotopes in the XENON detector [82], then translated into expected signal rates via the method described above.

### 2.3.2 Inelastic WIMP scattering

To obtain recoil spectra for WIMP-nucleon scattering for all EFT operators with inelastic kinematics, I use a modified version of DMFormFactor provided by Barello et al. [52]. The au-

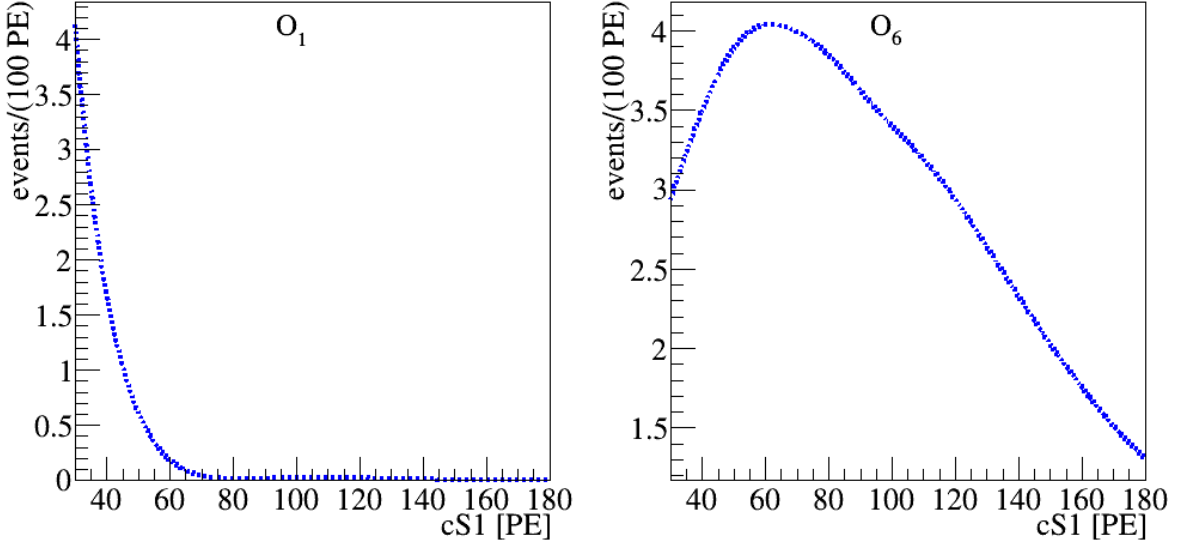


FIGURE 2.4. The expected signal in the high-energy region for a  $300 \text{ GeV}/c^2$  WIMP mass, normalized to five events. Left(right) is the spectra for  $O_1(O_6)$ . Notice that for  $O_1$  most of the events are not expected to deposit energy higher than 30 PE whereas for  $O_6$  a large fraction of the events appear in this region.

thors have modified the original package to enforce the new energy conservation condition  $\delta_m + \vec{v} \cdot \vec{q} + |\vec{q}|^2/2\mu_N = 0$ , primarily by replacing  $\vec{v}_{\text{elastic}}^\perp \rightarrow \vec{v}_{\text{inelastic}}^\perp = \vec{v}_{\text{elastic}}^\perp + \frac{\delta_m}{|\vec{q}|^2} \vec{q}$  in the definitions of the EFT and nuclear operators.

Assumptions regarding the dark matter halo and nuclear physics are unchanged. The mass splitting  $\delta_m$  between dark matter states is varied from  $(0 - 300)$  keV, safely beyond the value at which the predicted rate is zero for the entire mass range I consider.

## 2.4 Statistical inference

The statistical interpretation of data is performed using a binned profile likelihood method, in which hypothesis testing relies upon a likelihood ratio test statistic,  $\tilde{q}$ , and its asymptotic distributions [83] to constrain the coupling constants  $c_k$  for each operator  $\mathcal{O}_k$ . The two analysis channels are combined by multiplying their likelihoods together to produce a joint likelihood function.

$$(2.4) \quad \mathcal{L} = \mathcal{L}_{\text{lowE}(c_i^2, \mathcal{Q}_y, \mathcal{L}_{\text{eff}})} \times \mathcal{L}_{\text{highE}(c_i^2, \mathcal{L}_{\text{eff}})}.$$

Both analyses parametrize the NR relative scintillation efficiency,  $\mathcal{L}_{\text{eff}}$ , based on existing measurements [84]. Its uncertainty is the major contributor to energy scale uncertainties and is considered as correlated between the two analysis channels via a joint nuisance likelihood term.

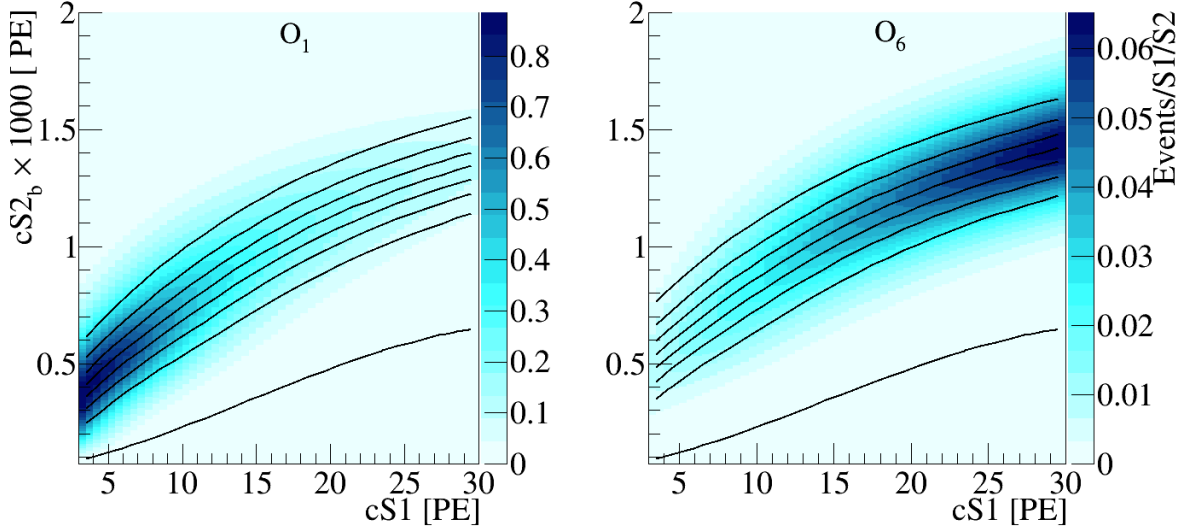


FIGURE 2.5. The expected signal in the low-energy region for a  $300 \text{ GeV}/c^2$  WIMP mass, normalized to five events. (a) is the spectra for  $\mathcal{O}_1$  (b) is the spectra for  $\mathcal{O}_6$ . Notice that for  $\mathcal{O}_1$  most of the events are expected to deposit energy lower than 30 PE whereas for  $\mathcal{O}_6$  a large fraction of the events do not appear in this region at all. The black lines indicate the bands constructed on these specific mass and operator models, and are dividing the signal into eight equally distributed signal subregions. This parameter space can be mapped with a one-to-one mapping to the  $\log(cS1_{ib}/cS1) - cS1$  space.

Throughout this study, all the parameters related to systematic uncertainties are assumed to be normally distributed.

For the low-energy channel an extended likelihood function which is very similar to the one reported in [85] and described in detail in [4] is employed. The  $\log(cS2_b/cS1), cS1$ -plane is divided into eight WIMP mass-dependent bands where events are counted. This binned approach is extended with the corresponding  $cS1$ -projected PDF of each band. The total normalization of the background is fit to data, and an uncertainty is assigned to the relative normalization of each band according to the corresponding statistical uncertainty of the calibration sample.

Signal shape variations due to energy scale uncertainty are modeled via simulation. These include the said  $\mathcal{L}_{\text{eff}}$  uncertainties and additionally the charge yield uncertainties, which are parametrized based on  $\mathcal{Q}_y$  measurement as described in [80].

The low-energy likelihood function is shown in Eq. 2.5,

$$(2.5) \quad \mathcal{L}_{lowE} = \mathcal{L}_1(c_k^2, \mathcal{L}_{\text{eff}}, \mathcal{Q}_y) \mathcal{L}_2(\epsilon_b) \mathcal{L}_3(\mathcal{L}_{\text{eff}}, \mathcal{Q}_y).$$

$$(2.6) \quad \mathcal{L}_1(c_k^2, \mathcal{L}_{\text{eff}}, \mathcal{D}_y) = \prod_j \text{Poiss}(n^j | \epsilon_s^j M_s(c_k^2) + \epsilon_b^j M_b) \times \prod_{i=1}^{n^{i,j}} \frac{\epsilon_s^j M_s(c_k^2) f_s^j(cS1^i) + \epsilon_b^j M_b f_b^j(cS1^i)}{\epsilon_s^j M_s + \epsilon_b^j M_b},$$

where  $f_s^j$  and  $f_b^j$  are the probability density functions of the signal and background respectively in band  $j$ , and  $M_s$  and  $M_b$  are the maximum likelihood estimators for the total number of signal and background events respectively.

$$(2.7) \quad \mathcal{L}_2 = \prod_j \text{Poiss}(n_b^j | \epsilon_b^j N_b)$$

The high-energy channel analysis employs a binned likelihood function. Observed and expected event yield are compared in the nine ROI  $\log(cS2_b/cS1), cS1$ -bins described in Sec. 2.2. Given the large statistical uncertainty of the background model the above extended likelihood approach is not repeated here. Instead, the maximum likelihood estimation of the background expectation in each bin is constrained by the statistical uncertainty of the calibration sample, while the total normalization is fit to the data. Additionally, to account for potential mis-modeling of the expected background distribution, mainly due to anomalous multiple scatter events, a systematic uncertainty of 20% is assigned independently to each bin. In the high-energy channel, uncertainty on the signal acceptance of analysis selections are computed for each signal hypothesis using the parametrized acceptance curve shown in Fig. 2.3. Uncertainties on the signal model  $\log(cS2_b/cS1), cS1$  distribution due to  $^{241}\text{AmBe}$  sample statistical fluctuations, as well as energy scale shape variation due to  $\mathcal{L}_{\text{eff}}$  uncertainties, are taken into account.

The high-energy likelihood function is defined in Eq. 2.8

$$(2.8) \quad \mathcal{L}_{\text{highE}}(c_k^2, \mathcal{L}_{\text{eff}}) = \prod_i ( \text{Poiss}(n_i^{obs} | n_i^s + n_i^b) \times \text{Gauss}(\eta_i^b) ) \times \mathcal{L}_{\text{stat}}(\epsilon_j^s, \epsilon_i^b) \times \mathcal{L}_{\text{unc}}^s(\mathcal{L}_{\text{eff}}, A)$$

where the product goes over all 9 bins,  $\epsilon_i^b$  is the fraction of background event in **bin**  $i$  and  $\epsilon_j^s$  is the fraction of  $^{241}\text{AmBe}$  data in **band**  $j$ . This means the uncertainty on the signal is assessed per band.  $n_i^s = N_{\text{tot}}^s(c_k^2, \mathcal{L}_{\text{eff}}) \times \zeta_{i,j}^s(\mathcal{L}_{\text{eff}}, \epsilon_j^s)$  is the number of signal events in bin  $i$ ,  $\zeta_{i,j}^s(\mathcal{L}_{\text{eff}}, \epsilon_j^s)$  is the fraction of signal events in bin  $i$  which is in band  $j$ .  $n_i^b = N_{\text{tot}}^{\text{cal}} \times \tau \times \epsilon_i^b(\eta_i^b)$  is the number of background events in bin  $i$ .  $\tau$  is the overall normalization of background to data, and is a free parameter.

## 2.5 Data From Recoil Energies Up To 1000 PE

Upon completing our analysis, I examined data in the  $cS1$  region above 180 PE, up to 1000 PE, since it will not be analyzed in any future XENON publications. I used the same data selection criteria as those applied for the high-energy channel. These selection criteria are not optimized

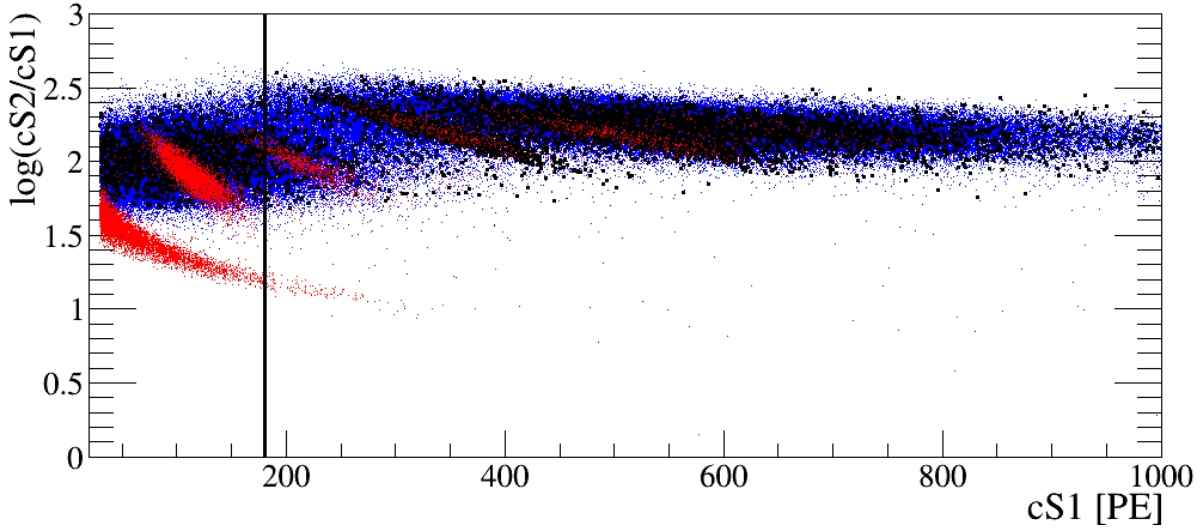


FIGURE 2.6. The full XENON100 dark matter science run data up to 1000 PE in cS1 (shown in black). In blue I show data from ER calibration ( $^{60}\text{Co}$  and  $^{232}\text{Th}$ ) and in red I show data from NR calibration ( $^{241}\text{AmBe}$ ). See the text for details on these populations. While the black vertical line represents the highest energy considered for quantitative interpretation in this analysis, there is no indication of elastic NRs even above that energy.

for the new even-higher energies and may exhibit a drop in acceptance for NRs to below 50%. Due to the lack of NR calibration data and of a rigorous background model in this energy range, a quantitative and statistically solid inference on dark matter hypotheses is impractical. Nonetheless, I provide a plot of the data here. Fig. 2.6 shows the distribution of science data in this extended range (in black) together with NR (in red) and ER calibration data (in blue).

The NR calibration data show the NR band from elastic scattering, with the aforementioned loss of statistics at energies above 180 PE clearly visible. Also visible are lines in the ER band from the inelastic scattering of neutrons on  $^{129}\text{Xe}$  (39.6 keV at 130 PE) and  $^{131}\text{Xe}$  (80.2 keV at 220 PE) as well as the delayed deexcitation of  $^{131m}\text{Xe}$  (169.3 keV at 350 PE) and  $^{129m}\text{Xe}$  (236.1 keV at 500 PE). ER calibration data are shown in blue and indicate the distribution of the prevalent background in this energy range. Since the detector is optimized for low-energy events, large S2 pulses saturate the PMT bases. This is visible in the ER band above 250 PE.

Finally, data from the dark matter search are shown in black. As can be seen, there is no indication of elastic NRs at energies above those analyzed in this study.

## 2.6 Results

A benchmark region of interest is defined between the upper and lower thresholds in cS1 for each channel. This region is bounded in  $y$ -space from above by the  $^{241}\text{AmBe}$  NR mean line and below by the lower  $3\sigma$  quantile of the  $^{241}\text{AmBe}$  neutron calibration data. The expected background in the region is  $3.0 \pm 0.5_{\text{stat}}$  (low-energy) and  $1.4 \pm 0.3_{\text{stat}}$  (high-energy). The number of DM candidates in this benchmark region is 3 (low-energy), and 0 (high-energy). Consequently, the data are compatible with the background-only hypothesis and no excess is found.

For the elastic scattering case, a 90% C.L.<sub>S</sub> [86] confidence level limit is set on the effective coupling constant,  $c_i$ , for all operators and masses in the range of  $10 \text{ GeV}/c^2$  to  $1 \text{ TeV}/c^2$ . The  $c_i$  are dimensionful, with units of  $[\text{mass}]^{-2}$ , so I first convert them to dimensionless quantities by multiplying them by  $m_{\text{weak}}^2 = (246.2 \text{ GeV})^2$ , following the conventions of [50].

These limits are shown in Fig. 2.7 in black, along with limits from CDMS-II Si, CDMS-II Ge and SuperCDMS [87].

For the inelastic scattering case, 90% C.L.<sub>S</sub> confidence level limits on the coupling constants (again scaled by  $m_{\text{weak}}^2$ ) are set. Fig. 2.8 shows limits on the  $\mathcal{O}_1$  (SI) coupling constant as a function of mass splitting and WIMP mass, Fig. 2.9 shows limits for all other operators as a function of the mass splitting  $\delta_m$  with a fixed WIMP mass of  $1 \text{ TeV}/c^2$ , projections of results from CDMS-II [88], ZEPLIN-III [89], and XENON100 [90] in the coupling constant and  $\delta_m$  parameter space are also reported.

For the elastic operator  $O_1$ , our results can be compared to those of standard SI analyses by computing the relevant zero-momentum WIMP-nucleon cross sections. This is not simple to do rigorously because the treatment of nuclear structure used in our analysis is different than in standard analyses; however, this difference is small for scattering via  $O_1$ . I can therefore quite safely use the “traditional” correspondence [91]

$$(2.9) \quad \sigma_N^{\text{SI}} = \left( C_1^N \right)^2 \frac{\mu_{\chi,N}^2}{\pi}$$

where  $\mu_{\chi,N}$  is the WIMP-nucleon reduced mass. Standard SI analyses assume isospin-conserving interactions, as I do in this analysis, so I can simply set  $C_1^N = C_1^0$ , such that  $\sigma_p^{\text{SI}} = \sigma_n^{\text{SI}}$ .

In principle a similar comparison can be done between our limit on the  $O_4$  coupling and standard SD analysis limits; however, this time the standard analyses do *not* assume isospin-conserving interactions. Instead they typically assume maximal isospin violation, that is, assuming that WIMPs couple either protons or neutrons. Limits are then derived independently on  $\sigma_p^{\text{SD}}$  and  $\sigma_n^{\text{SD}}$ . Because of this difference in assumptions, our limits on SD couplings are not directly comparable to usual analyses. However, they can be recast under the appropriate alternate model assumptions using the detector response tables I provide in the supplementary material.

## 2.6. RESULTS

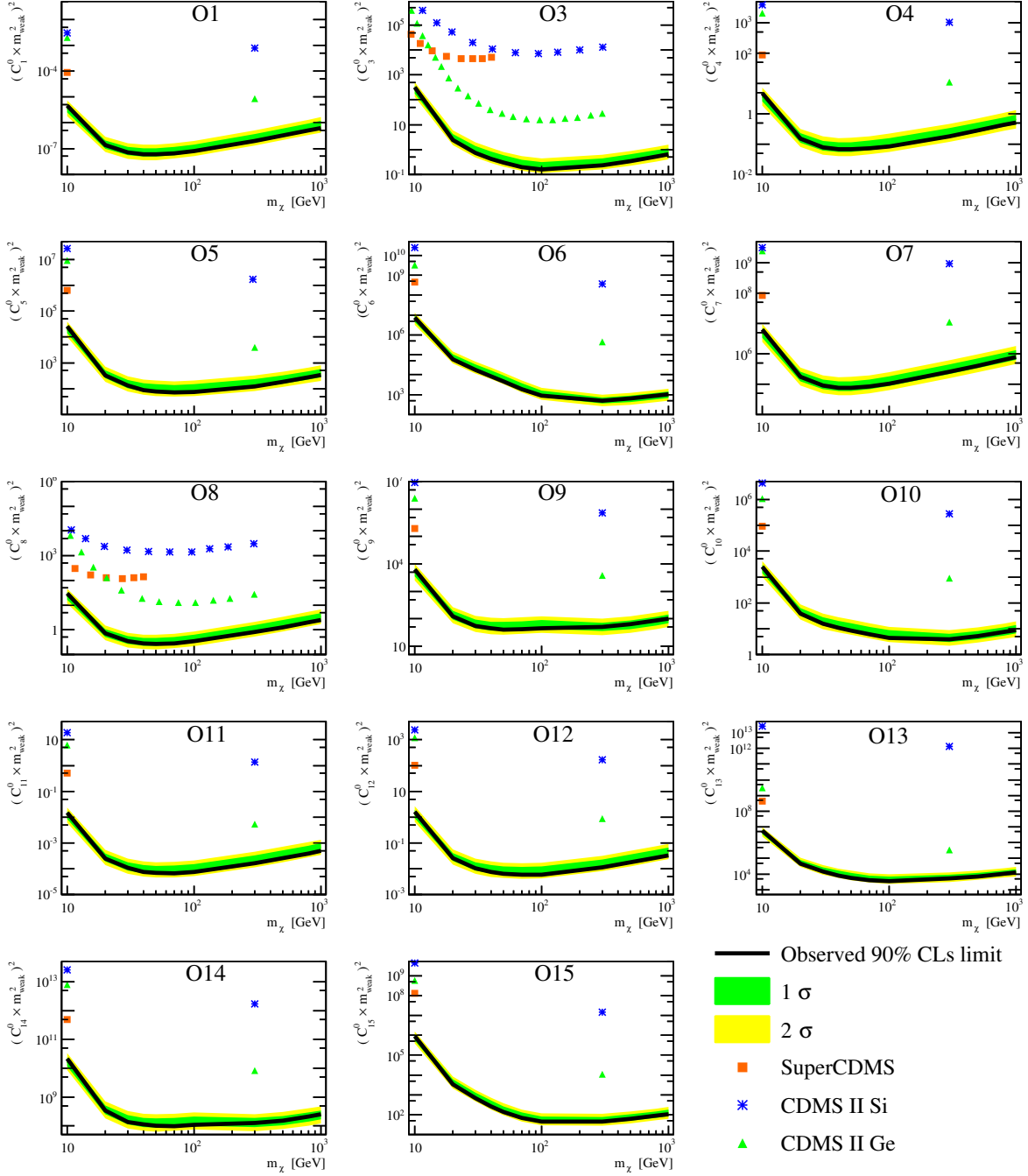


**FIGURE 2.7.** The XENON100 limits (90% C.L.<sub>S</sub>) on isoscalar dimensionless coupling for all elastic scattering EFT operators. The limits are indicated in solid black. The expected sensitivity is shown in green and yellow(1 $\sigma$  and 2 $\sigma$  respectively). Limits from CDMS-II Si, CDMS-II Ge, and SuperCDMS [87] are presented as blue asterisks, green triangles, and orange rectangles, respectively. For operators 3 and 8, a full limit was published, for all other operators only  $m_\chi = 10$  and  $m_\chi = 300$  are available.

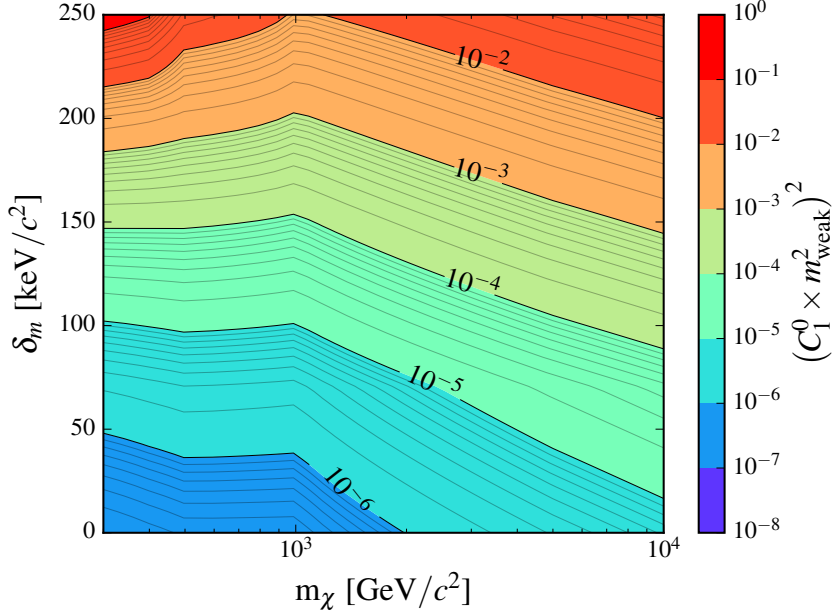
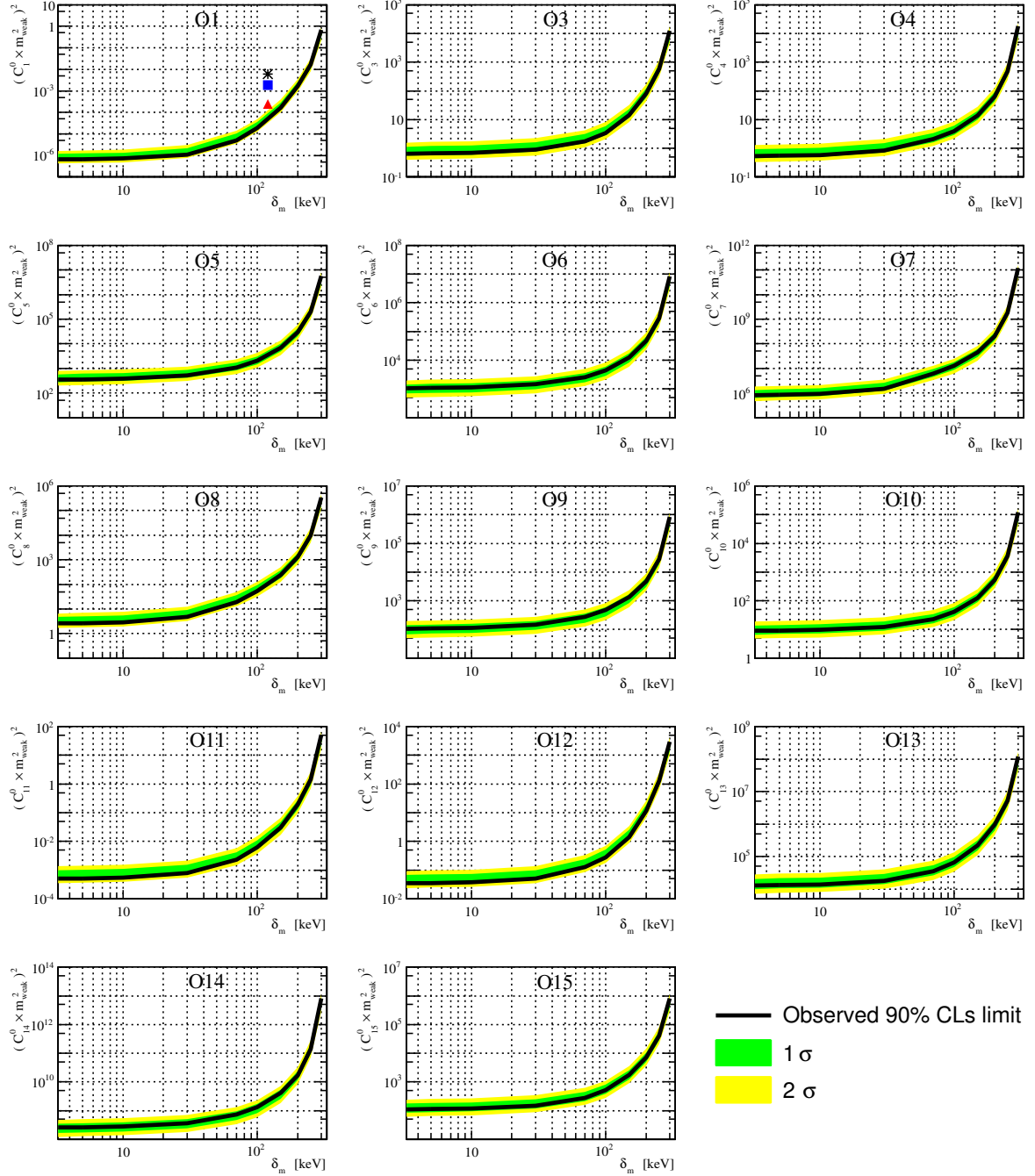


FIGURE 2.8. 90% C.L.S limits, for the inelastic model, on the magnitude of the coupling constant for  $\mathcal{O}_1$ , reported as a function of the WIMP mass and mass splitting  $\delta$ .

## 2.7 Summary

In this section I have presented an analysis of XENON100 data at recoil energies above 43 keVnr, with the new high energy bound set to 240 keVnr. I considered in this analysis two models which predict interactions in this energy region: an EFT approach for elastic WIMP-nucleon scattering, and a similar EFT approach but considering instead inelastic WIMP-nucleon scattering. The observed data were compatible with background expectations, and 90% C.L.S exclusion limits were constructed for WIMP masses between (10 and 1000) GeV.

## 2.7. SUMMARY



**FIGURE 2.9.** The XENON100 90% C.L.<sub>S</sub> limits on a  $1 \text{ TeV}/c^2$  WIMP isoscalar dimensionless coupling constant as function of the WIMP mass splitting  $\delta_m$  for all inelastic scattering EFT operators. Limits are indicated in solid black. The expected sensitivity is shown in green and yellow ( $1\sigma$  and  $2\sigma$  respectively). For  $\mathcal{O}_1$  (SI) results from XENON100(red triangle) CDMS-II(blue rectangle) and ZEPLIN-III(black star) are overlaid.



## DIREXENO

In Liquid Xenon experiments, the cloud of excimers produced when a particle recoils energy in xenon is estimated to have a complex shape. Nonetheless it is expected to have a typical size of  $O(100\text{nm})$ . Hence it is expected that the excimer cloud might undergo a *superradiance* emission. A variation in the temporal time of radiation between ERs and NRs might exist due to the size of the excimer cloud. This can improve the discrimination between background(ER) and signal(NR) for LXe DM detectors. Moreover weather the emitted radiation is correlated to the incoming exciting particle momentum, can be a more powerful tool for background reduction. Discarding events coming from the direction of the sun for example, is necessary once the neutrino floor [92] will be crossed.

Early studies conducted by Basov [93] (experimentally) and in NIST [94] (theoretically) both present the option of generating a coherent radiation in the VUV regime ( $\sim 178\text{ nm}$ ). The experimental setup was designed to bombard the LXe with 800 keV electron current pulse exciting (10 ns) the LXe. The constant electron current causes a reverse population constantly. In contrary in direct detection of DM experiments, there is no "pump" producing this inverse population. The study of weather a cloud of excimers caused by a single interaction can exhibit *superradiance* is still absence.

In this chapter I discuss Direxeno (Directional Xenon). An experimental setup designed at measuring *superradiance* or any other non-linear effect in LXe.

### 3.1 Experimental Setup

In order to identify *superradiance* effects in LXe, the temporal and spatial properties of scintillation events should be studied and quantified. In the DireXeno system LXe is circulated through a

small spherical cavity held in a thick sphere made of high purified fused silica (HPFS). The sphere is surrounded ( $\sim 4\pi$ ) by PMTs allowing high resolution spatial and temporal measurements of individual photons. The PMTs do not come in contact with the xenon, so less impurities are introduced to it, and the material selection is less stringent. The geometrical design of the system approximates a point source of scintillation photons, and a detailed vertex reconstruction within the LXe bubble is unnecessary. A schematic view of the system is shown in Fig 3.1 .

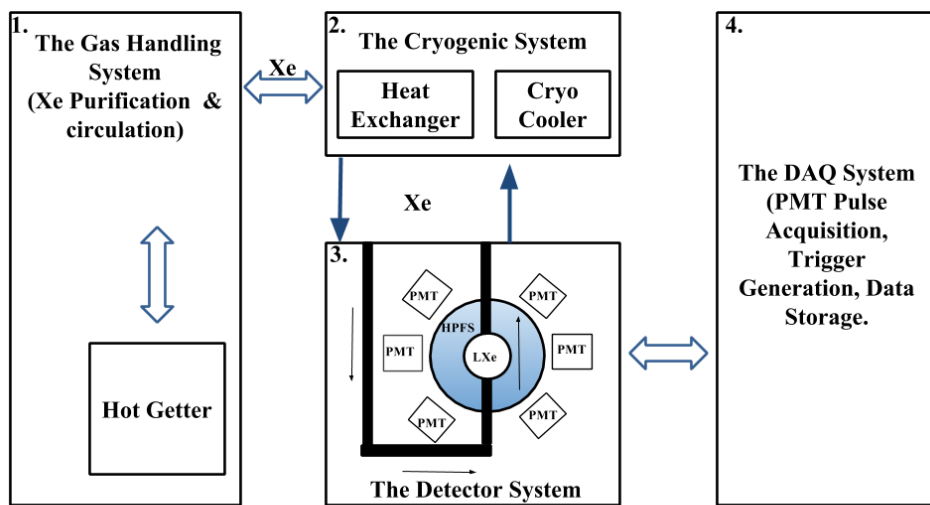


Figure 3.1: A schematic view of DireXeno.

The current system is designed with  $\sim 1$  ns time resolution, less than 1 ns synchronization between PMTs, and  $\sim 8$  radians spatial resolution. Since the exact nature and magnitude of *superradiance* in LXe is yet unknown a guiding principle in the design was flexibility to upgrades or redesign of any part of the system to fulfill any future experiment requirements. The modular design allows gain fast and easy recovery in case of components malfunction.

The system is made of four main building blocks. (i) **The gas handling system** which in normal working mode circulates the xenon and purifies it. (ii) **The cryogenic system**, liquefies the xenon and delivers it to the detector system. (iii) **The detector system** consists of a fused silica sphere that holds a small bubble of LXe target, and PMTs around the sphere. (iv) **The DAQ system** supplies high voltage (HV) to the PMTs and handles monitoring, triggering and digitization of data. The entire assembly is held on 3 separate racks as shown in Fig. 3.2.

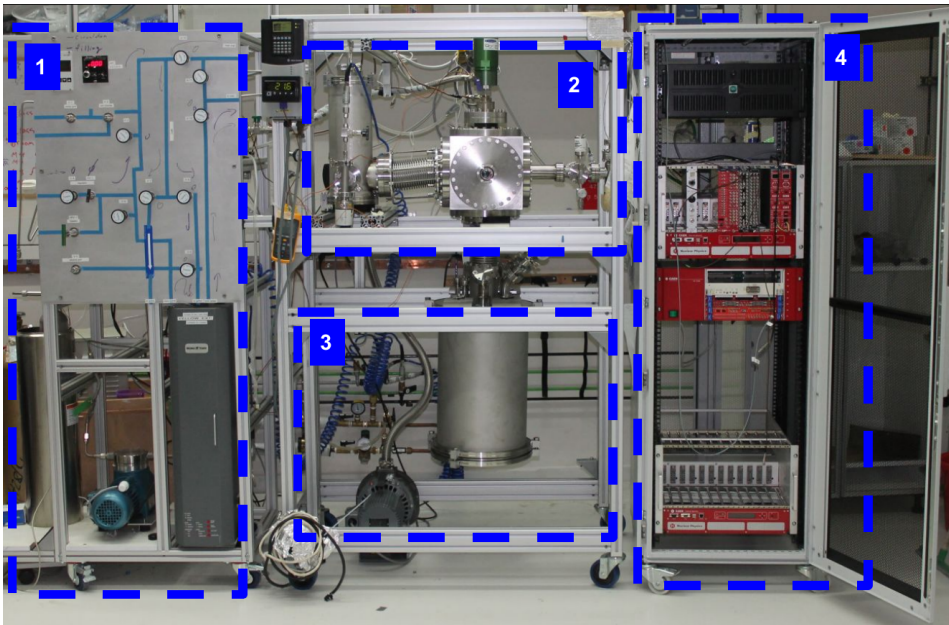


FIGURE 3.2. The DireXeno system mounted on the three racks. 1. The gas handling system. 2. The cryogenic system including the heat exchanger. 3. The detector chamber. 4. The Data acquisition system.

### 3.1.1 The gas handling system

In DIREXENO only the prompt scintillation is measured, so a high level of LXe purity is not of a great importance. However in many LXe detectors the desired level of impurity concentration is at the level of 1 ppb  $O_2$  equivalent [? ] This is crucial to allow ionization electrons drift for several cm. To reach that purity level in a reasonable amount of time (several days instead of months), a continuous purification is needed. The gas handling system provides this process along with all gas handling operations such as filling and recuperation and circulation. The xenon circulation also plays a major role in heat transfer.

During purification, The xenon is forced by a circulation pump<sup>1</sup> extracting LXe from the detector part through a heat exchanger<sup>2</sup> where it is heated and vaporized, into a hot getter<sup>3</sup> which cleans the xenon. The xenon passes through a mass flow controller<sup>4</sup> (MFC), enabling monitoring and controlling the amount of heat introduced to the system. Once purified, the xenon is delivered back to the cryogenic system via the heat exchanger, where the remaining GXe is liquefied before flowing back to the detector part. A schematic of this system is shown in fig. 3.3.

<sup>1</sup>N143 SN.12E AC 230V50HZ KNF diaphragm circulation pump

<sup>2</sup>GEA GBS100M-24 plate heat exchanger

<sup>3</sup>MONO-TORR PS4-MT15-R-2

<sup>4</sup>MKS mass flow controller 1179A00614CR1BM

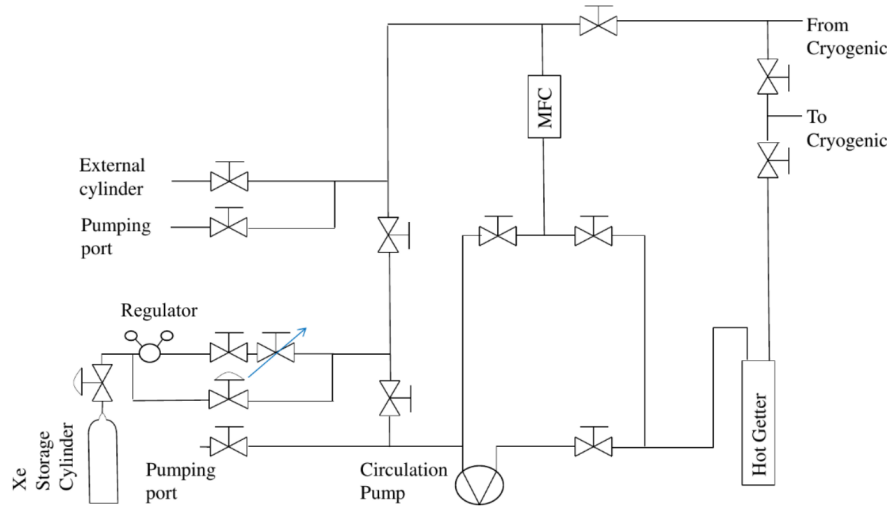


FIGURE 3.3. Schematics of the gas handling system. High pressure valves are indicated as valves with arcs. Needle valves are indicated as a valve with an arrow.

### 3.1.2 The cryogenic system

Remote cooling is generally used in LXe experiments due to reduction in background radiation and acoustic noise from the cooler to the detector, and due to design flexibility. The cryogenic system is connected to the gas handling system on one side and to the detector part on the other, and built such that replacing the cryo-cooler type (e.g., to PTR) requires just an adaptation to the top flange.

The cryogenic system is divided to an outer vessel (OV) which holds the insulation vacuum, and an inner vessel (IV) which holds the xenon. In addition to the vacuum which prevents heat leakage due to diffusion and convection, the IV is completely covered by multi layer aluminized Myler to prevent heating via radiation.

The OV is made of a 10" Conflat (CF) cube, with ports on all six faces, interfacing the gas handling system and the detector part, and bearing service ports (e.g., feed-throughs, pumping ports, view ports). The OV is connected to the detector part via a 6" CF flexible bellows, providing a shared vacuum.

The IV is made of 1.5" long cylinder with 6" CF flanges on both sides, holding xenon within. A 120 mm diameter cold finger is welded to its top flange. The design of the cold finger is similar to the one in [75]. The inner part of the cold finger is made of long fins, resulting in a better heat transport. The upper part of the cold finger is in thermal contact with the QDrive cryo-cooler<sup>5</sup> via a copper adapter. The copper adapter holds two 100Ω pt resistor which are connected to a PID reader<sup>6</sup> for temperature measurements. A cartridge-heater is also inserted to the copper adapter for emergency heating in case xenon freezes on the cold finger.

<sup>5</sup>QDrive 20BB 9p6 A 3 AYNBNCO

<sup>6</sup>cryo-con model 18i Cryogenic Temp Monitor

### 3.1. EXPERIMENTAL SETUP

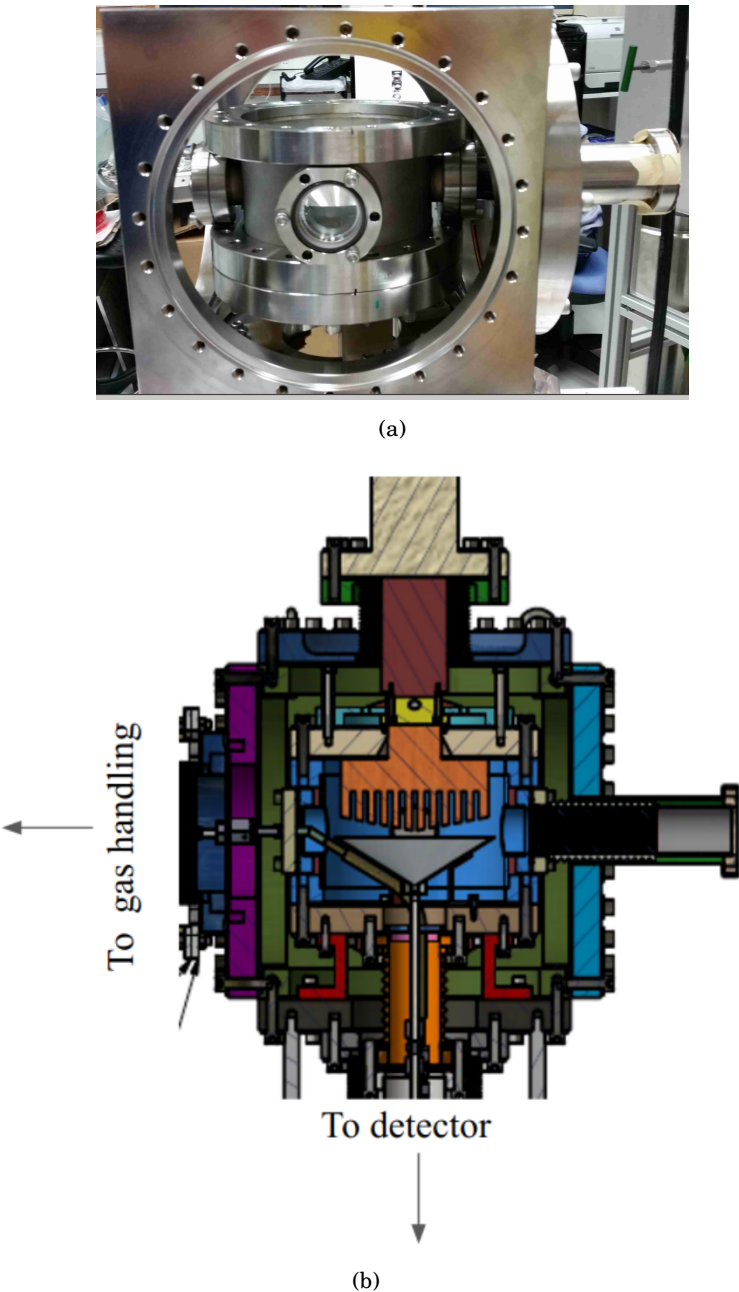


FIGURE 3.4. (a) Picture of the cryogenic system. (b) CAD view of the cryogenic system.

The cryo-cooler is connected via a  $4\frac{1}{2}$ " flange to the OV top flange. While usually cryo-coolers used for xenon experiments constantly operate in maximal cooling, the QDrive cryo-cooler utilizes a temperature control to vary its cooling power up to 70 W. This allows setting a desired working temperature which is constant within less than 0.1 °C measured on the cryo-cooler.

On the inner side of the IV bottom flange a thin 0.6 mm SS funnel is installed collecting LXe drops from the cold finger, and delivering them to the detector. This flange is attached to the detector part, via a  $3\frac{3}{8}$ " flexible bellows. The bellows hosts two pipes connected to the circulation system, and a third pipe coming from the funnel. The three pipes deliver LXe whereas the GXe is filling the bellows volume. The purer LXe (from the gas handling system) and the less pure LXe (from the cold finger) are separated, and can be delivered to different parts of the system. Some of the guidelines for the design of the cryogenic system are based on [? ]. The CAD view of the design of the cryogenic system and a photo of the actual system are shown in Fig 3.4.

### 3.1.3 The detector system

The detector system refers to a vacuum chamber and its inner assembly consisting of a transparent sphere that contains the LXe, the PMT sensors observing it and their accessories. This chamber is placed below the cryogenic system.

The interface unit to the cryogenic system is built out of two flanges welded together via seven tubes, which serve as service ports for electrical and other feedthroughs: four with a  $2\frac{3}{4}$ " CF flange, and three with a  $1\frac{1}{3}$ " CF flange (mini-CF). The upper flange, ISO-K NW320, shares the cryogenic system's OV insulation vacuum, while the bottom one, CF-10", is part of the IV and could hold xenon for future detectors. The CF flange is also adapted to fit a smaller CF- $4\frac{5}{8}$ " flange which is currently used.

The vacuum chamber is made of an ISO-K NW320 nipple closed with a blank flange from below, the length of the nipple is determined such that the maximal height of the whole apparatus is 190 cm, allowing an easy transport of the detector through standard doors.

The  $4\frac{5}{8}$ " CF flange is connected to a split vessel that serves as a LXe reservoir. one part is connected to the top of the HPFS sphere, and one to the bottom. LXe is circulated such that LXe coming from the gas system drips into one part and pumped from the other. This controls the liquid level, and the sphere is constantly filled with LXe.

The sphere is a custom designed hollow shell made of Corning HPFS 8655 with high transmittance to VUV. Two Invar tubes with SS mini-CF flange are connected to the sphere on both sides. The technical design and photo of the sphere are shown in Fig. 3.5. The optical properties of the sphere will be further discussed in Sec. 3.2. The bottom flange of the sphere is held using a brass holder to prevent force or torque applied on the sphere while mounting it. The brass holder is connected to a plate held from the top CF-10" flange.

Photons emitted from the LXe in the sphere are detected by 20 PMTs<sup>7</sup>. The PMTs are chosen

---

<sup>7</sup>R8520-406 Hamamatsu 1" PMT, active area 20.5 mm × 20.5mm

### 3.1. EXPERIMENTAL SETUP

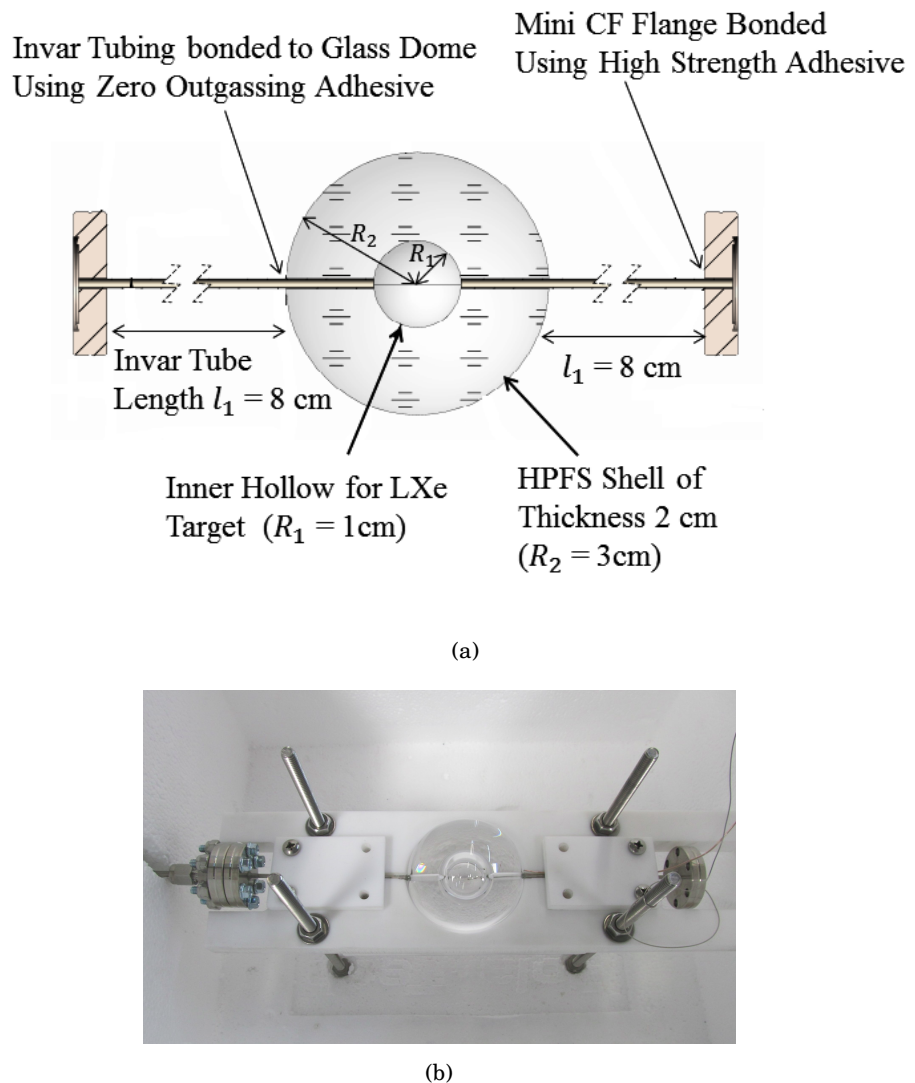


FIGURE 3.5. (a) The technical design of the HPFS shell with Invar tubing and mini CF flanges. (b) The manufactured HPFS shell, held in a test fixture.

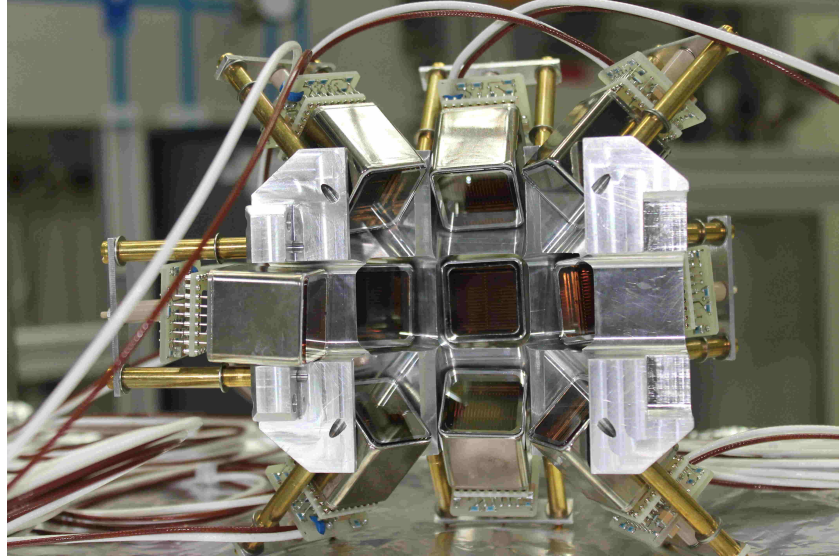


FIGURE 3.6. A PMT holder–hemisphere. Two identical hemispheres are used to hold the PMTs around the sphere.

to have a quantum efficiency greater than 30% at 178 nm. The gain of the PMTs is  $2 \times 10^6$  at an applied voltage of 900 V. A positive voltage divider<sup>8</sup>, is used to provide high voltage to the PMTs. The PMTs are held with a special aluminum holder, coated with anti-reflection substance. The holder is made of two hemispheres hosting the PMTs in 3 rows all of them pointing to the center of the sphere. The PMTs are attached to the holder by their voltage-divider bases using M2 PEEK screws (see Fig 3.6). The CAD design and a photo of the detector system are shown in Fig. 3.7.

### 3.1.4 The data acquisition system

The DAQ system is heterogeneous using both NIM and VME electronic modules. The data readout is being carried out through a PCIe card<sup>9</sup> connected via an optical link to a VME controller<sup>10</sup>. A schematic layout of the DAQ system is shown in Fig. 3.8.

The PMTs are ramped up to +800V (the maximum is +900V) using VME high voltage distributor module<sup>11</sup>. The raw pulses from the PMTs are amplified and shaped using two PMT preamplifiers<sup>12</sup>. The preamplifier operates from DC to 275 MHz and produces two identical  $50\ \Omega$  non inverting outputs with voltage gains of 10 for each PMT channel. One of the outputs is converted into a digital signal by an ADC<sup>13</sup>, and the other to binary signals using two

<sup>8</sup>Hamamatsu VDS18130p 24 channel poisitve polarity.

<sup>9</sup>CAEN A3818 PCIe

<sup>10</sup>CAEN V2718 VME controller

<sup>11</sup>iseg VDS18130p : 24 independent channels positive polarity voltage distributer

<sup>12</sup>Phillips 776. 16 independent and direct-coupled amplifiers channels

<sup>13</sup>CAEN ADC V1742: switched capacitor digitizer

discriminators<sup>14</sup>.

The ADC consists of two 12bit 5GS/s switched capacitor digitizer sections, each of them with 16+1 channels, based on DRS4 chip. The dynamic range of the input signal is 1 Vpp with an adjustable DC offset. This module constantly samples (5GS/s, 2.5 GS/s or 2 GS/s) either bipolar or unipolar analog input signals, and records them into circular analog memory buffers. Once triggered, all analog memory buffers are frozen and digitized into a digital memory buffer with a 12 bit resolution.

The binary output signals from the discriminator are duplicated and fed to

the logic module<sup>15</sup> and to a scaler<sup>16</sup>. A global majority trigger is generated in the logic module with the coincidence of any two out of the twenty PMTs within a time window of **XXX ns**. The event information and trigger rate are read from the ADC, while the individual PMTs trigger rate from the scaler. Further analyses of the relevant events are carried out offline.

## 3.2 Optical properties of the sphere

The central component of the experiment is the HPFS sphere, which holds the LXe target, located in the center of the detector system. The sphere is made of two Corning HPFS 8655 hemispheres attached by a UV transparent glue. The refractive index of this HPFS is 1.58 at 185 nm, matching to the LXe one, which is 1.61. Hence, there is minimal diffraction from the original direction of the photons as they transit from the LXe target to the sphere. The refractive index at various wavelengths are shown in Fig. 3.9 (left panel).

The HPFS transparency to VUV photons is an extremely crucial parameter for setting the sphere's dimensions (inner and outer radii). Therefore, the transmittance of an HPFS sample was measured, using a VUV monochromator light source. The measured transmittances as a function of wavelength are shown in Fig. 3.9 (right panel). The transmittance of the sample at 178 nm, is  $\sim 98.7\%/\text{cm}$ .

The sources that will be used for exciting the xenon, and creating the superradiance (signal) as well as the standard emission (background), will be  $^{137}\text{Cs}$  ( $E_{\gamma}=662 \text{ keV}$ ) and  $^{57}\text{Co}$  ( $E_{\gamma}=122\text{keV} \& 136 \text{ keV}$ ) for ER with mean free path of  $\sim 4 \text{ cm}$  and  $\sim 1 \text{ cm}$  respectively. For NR  $^{241}\text{AmBe}$ , D-D neutron generator, or neutron produced in an accelerator will be used.

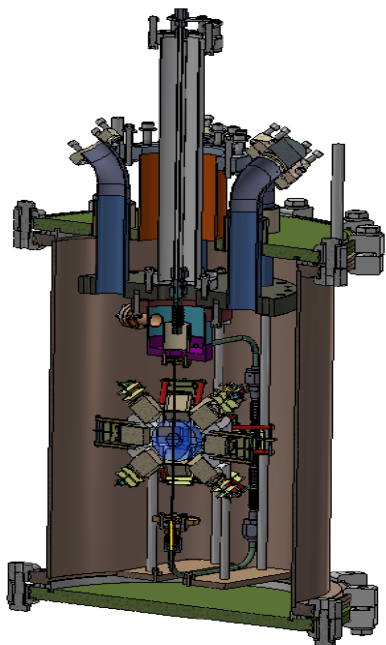
Using a GEANT4 based simulation [95] studying the path of the scintillation photons the sphere dimensions are optimized. The shell should be thick enough to reduce internal reflections, but not too thick to attenuate the scintillation light. The LXe target bubble within should not be too large in order to avoid double scatters. The outer radius is 3 cm, and the inner (the hollow space that holds the LXe) is 1 cm.

---

<sup>14</sup>CAEN V895 16 channel leading edge discriminator

<sup>15</sup>CAEN V1495: FPGA based general purpose VME board

<sup>16</sup>CAEN V830: 16 channel scalar



(a)



(b)

FIGURE 3.7. (a) CAD design of the detector part. (b) First mounting of the detector part, still not connected to the rest of the system.

### 3.2. OPTICAL PROPERTIES OF THE SPHERE

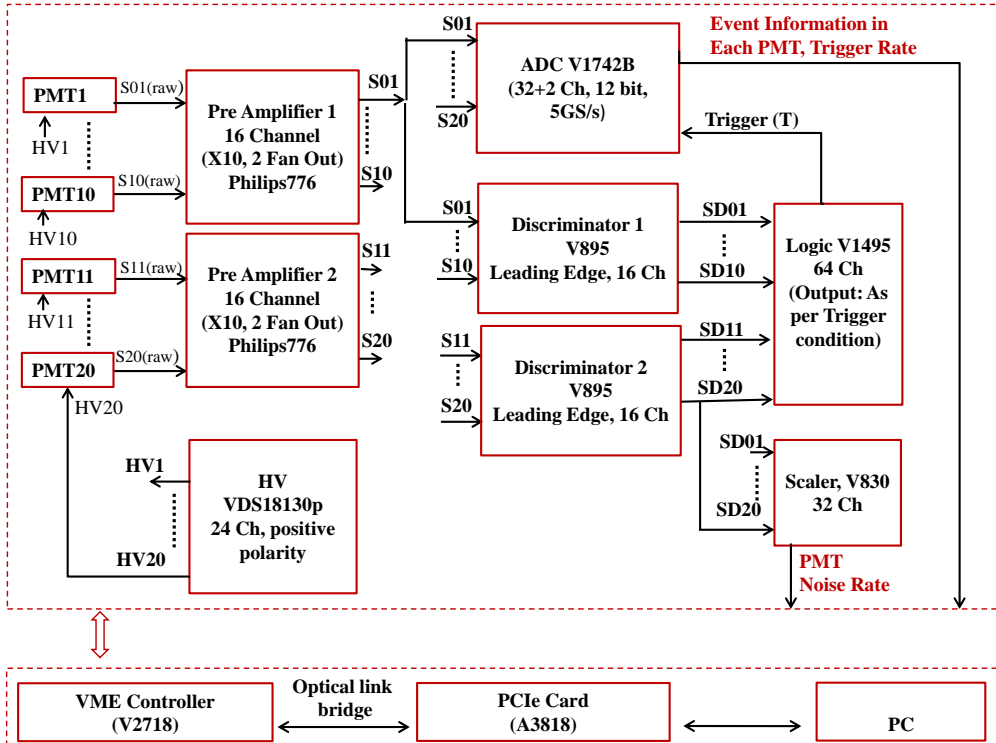


FIGURE 3.8. The schematic of the data acquisition system of DireXeno. The signal coming from 20 PMTs ( $i = 1 - 20$ ) and the subsequent electronic channels to record the events once triggered. Where  $S_i(\text{raw})$  is the raw electrical pulse output of the PMTs,  $S_i$  are the amplified pulses, and  $SD_i$  are the binary outputs from the discriminator [Why is VME controller in lower box](#) .

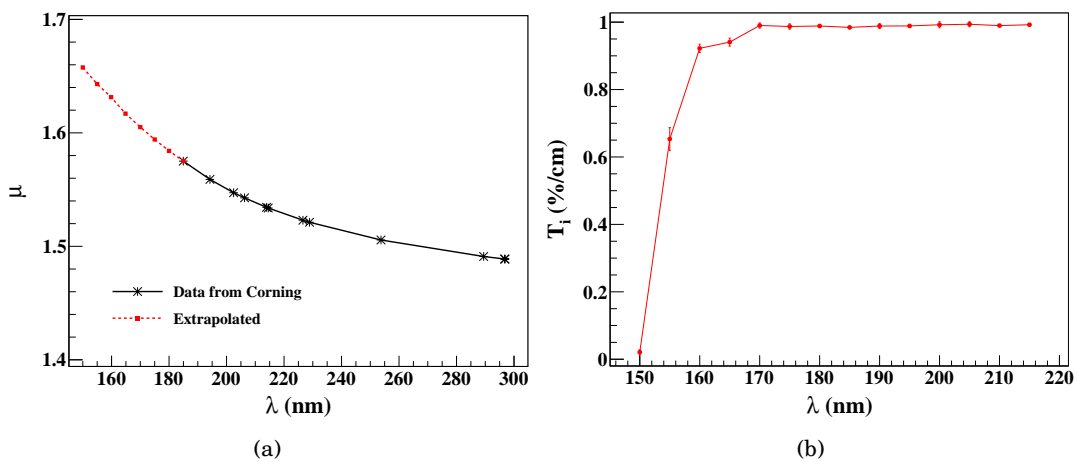


FIGURE 3.9. Some relevant characteristics of HPFS-8655. (a) The refractive index as provided by corning and extrapolated to relevant wavelength range. (b) The internal transmittance ( $T_i$ ). [Say something about the error bars](#)

### 3.3 Detector sensitivity

The sensitivity of the detector is estimated by its ability to identify an anisotropic component in the scintillation photons emission pattern (signal), over the isotropic one (background). The photon emission pattern is modeled using a combination of isotropic emission and one or two beams:

$$(3.1) \quad \mathcal{F}(\theta, \phi) = (1 - r_{aniso}) \cdot f_{iso} + r_{aniso} \cdot [r_1 f_G(\sigma_1) + r_2 f_G(\sigma_2)],$$

where  $f_{iso}$  is the PDF of an isotropic emission,  $f_G$  is a PDF of a Gaussian distribution with half width  $\sigma$ .  $r_{aniso}$  is the anisotropic emission fraction, and  $r_{1,2}$  are the relative beams intensities. The first beam direction is random, and the second's is either random ("uncorrelated") or opposite to the first's ("correlated"). The different emission patterns used here are summarized in Table 3.1.

Table 3.1: Anisotropic emission patterns. For all patterns  $r_{aniso} = 0.1$

Pattern no.	No. of beams	type	Beam half widths		Signal fractions		$N'$
			$\sigma_1$	$\sigma_2$	$r_1$	$r_2$	
1	1	single beam	$5^0$	-	1	0	3200
2	1	single beam	$15^0$	-	1	0	4630
3	2	correlated	$5^0$	$5^0$	0.5	0.5	4520
4	2	correlated	$15^0$	$15^0$	0.5	0.5	9770
5	2	uncorrelated	$5^0$	$5^0$	0.5	0.5	9370
6	2	uncorrelated	$5^0$	$10^0$	0.5	0.5	19500
7	2	uncorrelated	$15^0$	$15^0$	0.5	0.5	28200
8	2	uncorrelated	$10^0$	$30^0$	0.5	0.5	49900
9	2	uncorrelated	$10^0$	$30^0$	0.2	0.8	56000
10	2	uncorrelated	$30^0$	$10^0$	0.2	0.8	43000

A GEANT4 based simulation is used to model the detector system, generate photons, propagate them through the detector, and obtain a PMT hit pattern. The photons detected at the PMTs are mapped and put through a statistical test to check the detector's sensitivity towards the different emission patterns.

The relevant geometrical and optical parameters, which are used in the simulation, are listed in Table 3.2. The scintillation light produced in a particular event is emitted by a cloud of excimers. This cloud is assumed to have a linear size much smaller than that of the optical system. Therefore each event is simulated as a number of photons that are emitted from a point in the LXe with some emission pattern (see Table 3.1). The number of generated photons for each event is taken to be Poisson(50), which correspond to an energy deposition of  $\sim 2.5\text{keV}$  or  $\sim 7\text{keV}$  for ER or NR respectively. The LXe target is much smaller than the mean free path of the source particles, and to account for that the events are uniformly generated in the LXe volume. The probability for a photon being transmitted/reflected at a given surface is determined by Fresnel's equations, which include Snell's law for the transmitted light, and specular reflection for the

reflected light. The boundary surfaces between different media such as, the LXe–HPFS, HPFS–vacuum and vacuum–PMT, are assumed to be perfectly smooth, therefore enabling only specular reflection. The photons reaching the PMTs can either be detected, absorbed or reflected from the photocathode or PMT window. A simplified approach of the above possibilities is considered: a photon reaching the PMT has a 30% probability to be detected (since the PMTs have  $\text{QE} \geq 30\%$ ), 50% probability to get absorbed and 20% probability to get specularly reflected.

Table 3.2: The parameters used in simulation

Parameter	Value	Parameter	Value
LXe absorption length	100 cm	HPFS shell inner radius	1cm
LXe scattering length	35 cm	HPFS shell thickness	2 cm
LXe refractive index	1.61	PMT QE	30%
LXe Scintillation wavelength	178	PMT distance from center	39 mm
HPFS absorption length	100 cm	Number of PMT	20
HPFS refractive index	1.57	PMT active area	22mm × 22mm
HPFS scattering length	$\infty$	Invar tube diameter	1 mm

The statistical fluctuation in the electronic signal generated in a PMT for a certain number of incident photon is taken into account. The R8520 PMTs have 20% probability for double photoelectric emission for 178 nm photons, which is included in the simulation. Each detected photon on a PMT is assigned a uniformly random position on the PMT surface. The direction of this point with respect to the center of the LXe sphere is defined as the incident direction of the photon. The direction information is then used to calculate the angles between all possible pairs of photon for any event and calculate the correlation between all angle pairs. [Do you want to add fig of correlations iso and aniso?](#)

In order to quantify the anisotropicity of the emission, the angle correlation distribution of an anisotropic hit pattern is compared to that of the isotropic pattern. A  $\chi^2$  test statistics is used where the reduced  $\chi^2$  is defined as:

$$(3.2) \quad \chi^2_v = \frac{1}{v} \sum_{i=1}^v \frac{(O_i - E_i)^2}{E_i},$$

where  $E_i$  is the expected number of entries for an isotropic emission obtained from a sample of  $10^5$  simulated events.  $O_i$  is the observed number of entries, and  $v$  is the total number of angle correlation bins which is also the degree of freedom. Sixty bins of identical width are used.

To asses the needed exposure to claim discovery assuming one of the pattern mentioned above,  $10^4$  data sets are generated and tested against the null hypothesis. This is repeated for increasing number of events between 1 – 4000 assuming different values of the anisotropy fraction ( $r_{aniso}$ ). The  $\langle \chi^2_v \rangle$  and its  $2\sigma$  band for pattern 1, assuming  $r_{aniso} = 0.1$  overlaid with the corresponding values for an isotropic emission are shown in Fig. 3.10. The values of  $N'$ , required to claim  $5\sigma$

discovery, for different values of  $r_{aniso}$  are calculated for each pattern as illustrated in Fig. 3.11. The number of events  $N'$  for  $r_{aniso} = 0.1$  are summarized in Table 3.1 for all emission patterns.

A simulation with two typical sources that emit isotropically, a  $10 \mu\text{Ci}^{137}\text{Cs}$  (662 keV gamma), and a  $2.7 \mu\text{Ci}$  AmBe (5 MeV neutron), shows that for an average yield of 50 photons/event, the rate of events in the detector is:  $1.25 \times 10^4$  events/day for NR and 625 events/day for ER. Therefore a system that can operate stably for few weeks is expected to do reasonable measurements for ER and NR events.

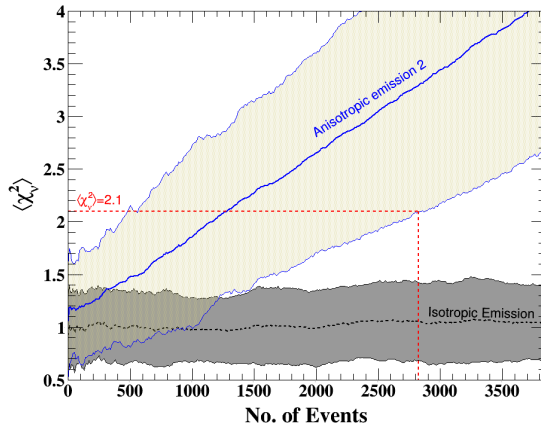


FIGURE 3.10.  $\langle \chi_v^2 \rangle$  and its  $2\sigma$  band for isotropic emission (black) and for pattern 2 (blue). The  $\langle \chi_v^2 \rangle$  for isotropic emission fluctuate around 1 with  $\sigma = 0.2$  which is consistent with the expected value of  $\frac{1}{\sqrt{30}} \equiv 0.18$  for reduced  $\chi^2$  distribution with 60 degrees of freedom.  $\sim 3000$  events are needed to claim  $5\sigma$  discovery ( $\chi_v^2 = 2.1$ ) for this emission pattern

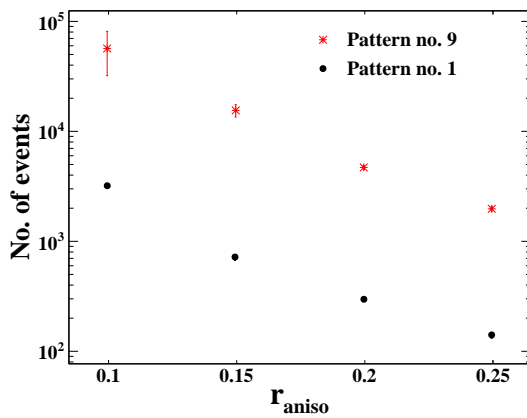


FIGURE 3.11. The number of events needed for each emission pattern to achieve  $5\sigma$  presented only for pattern 1 and 9. Here  $r_{aniso} = 0.1$ . for four different values of  $r_{aniso}$ .

### 3.4 Summary

The setup of Direxeno, an experiment to measure the spatial and temporal distribution of LXe scintillation, has been presented. The system consists of 4 main building blocks (gas handling, cryogenic, detector, and DAQ), each of which can be exchanged without altering others allowing significant flexibility and modularity. Each of the building blocks has been described in detail, with emphasis on the design and components.

The sensitivity of the setup to different postulated non isotropic emission patterns are studied using MC simulations. For the patterns studied, a run-time of 2-3 weeks is required using typical radioactive sources. Therefore the system is designed to maintain stability over a reasonable time period.

Using DireXeno, effects like superradiance or any other non-linear scintillation can be measured. Measuring the correlation between the direction of the emission and the direction of the radioactive source, may lead to directionality measurement which will allow enhanced statistical modeling of background and improved sensitivity in DM experiments.



## CALIBRATION SYSTEM FOR XENON1T

A crucial prerequisite for having a successful detector is a good understanding of the response for different types of interactions. In low-background experiments the usual technique for quantifying the detector response for different radiation types, is by creating controlled data samples. These samples are obtained by exposing the detector to a radioactive source with intensity which is order of magnitude greater than the background rate, insuring that events in the detector are coming from a well defined source. The study of these induced signals is known as "*detector calibration*".

The two measurables of XENON100 and XENON1T are S1 and S2 (see Sec. 1.9.2). The efficiency of detecting the scintillation light determines the energy threshold of the detector. Both light and charge yields can be attenuated by impurities in the LXe.

The S1 signal depends on the exact location of the interaction, due to non uniformity of scintillation light collection. This light collection is effected the solid angle covered by the PMTs, Rayleigh scattering length, reflectivity, transmission of the electrodes, etc. Extracted electrons are absorbed by impurities, mainly by oxygen and water, the number of electrons reaching the GXe is depth (z) dependent. Hence a correction to the energy scale both in S1 and S2 should be applied. This calibration is known as light and charge collection.

The main background source of XENON1T is due to electromagnetic interactions, predominantly,  $\gamma$ s, interacting in the target. Large fraction of background events occur near the TPC walls, this is due to the stopping power of LXe. Therefore, most of the background rejection is achieved through fiducialization, namely limiting the science data to a smaller FV. In addition, the ratio between S2 and S1 for NRs (expected signal) and ERs (background) is different in nature, and is larger for ERs. The main discrimination power of XENON1T exploit this ratio difference. A good understanding of the different response to the two interaction types is important to quantify the

background distribution. In addition, a good understanding of the NR response is important to produce the expected signal model. This is, amongst other, important to understand the effects of different data selection criteria applied in the analysis process. This calibration is known as "NR and ER bands"

The calibration technique used in XENON100, is placing a gamma source outside the detector and create the controlled data sample. However, this approach is not applicable for XENON1T. The main obstacle is to deploy the source inside the water tank. Moreover, for each calibration type, events need to fulfill certain data selection criteria which dictates the rate and energies needed.

For the light and charge collection calibration the full absorption peak is used; therefore even low-energetic sources, such as  $^{137}\text{Cs}$  (662 keV  $\gamma$ s) can be used to produce a fairly large data sample in a reasonable time. For the ER band calibration, just placing a source near the detector is not sufficient. There are more data selection criteria needed for this calibration.

A good ER band calibration event should have low energy deposition ( $2 - 15 \text{ keV}_{\text{ee}}$ ), contain only a single scatter, and occur inside the FV. Notice that the diameter of XENON1T TPC is  $\sim 1$  meter meaning a  $\gamma$  needs to penetrate the FV (travel  $\sim 10$  cm in LXe) interact such that the energy deposition is low (scatter in a small angel), and exit the TPC without interacting again (travel  $\sim 90$  cm) without scattering again to meet the selection criteria. The probability for that to happen, even for a 2 MeV source is very low  $\sim 10^{-7}$ . Because the detector cannot process data at high rates (O(100Hz)), the amount of time needed for this calibration is extremely long, and a new approach is needed.

Internal calibration techniques, in which a short lived radioactive source is dissolved inside the LXe is one of the calibration methods used in XENON1T. The radioactive sources used are:  $^{83m}\text{Kr}$ , tritiated methane  $\text{CH}_3\text{T}$  and  $^{220}\text{Rn}$ .

In this section I describe the new technique for external calibration, mainly ER band calibration, including the radioactive sources used, the holders of the sources which will confine there radiation to a smaller solid angle, and the system which drives the sources into place. The detector has been modeled in details using the GEANT4 toolkit [95] which provides also the nuclear and electronic recoil differential cross-section. Using this powerful toolkit one simulates the response of the detector to the different sources and study the expected response of the detector.

## 4.1 Radioactive source

### 4.1.1 ER band calibration

The mean free path of  $\gamma$  traveling in xenon is of the order of several cm (8.3 cm for a 1 MeV  $\gamma$ ), depending on the  $\gamma$ 's energy(see Fig. 4.1), a good  $\gamma$  calibration source should emit energetic enough  $\gamma$ s to penetrate the FV.

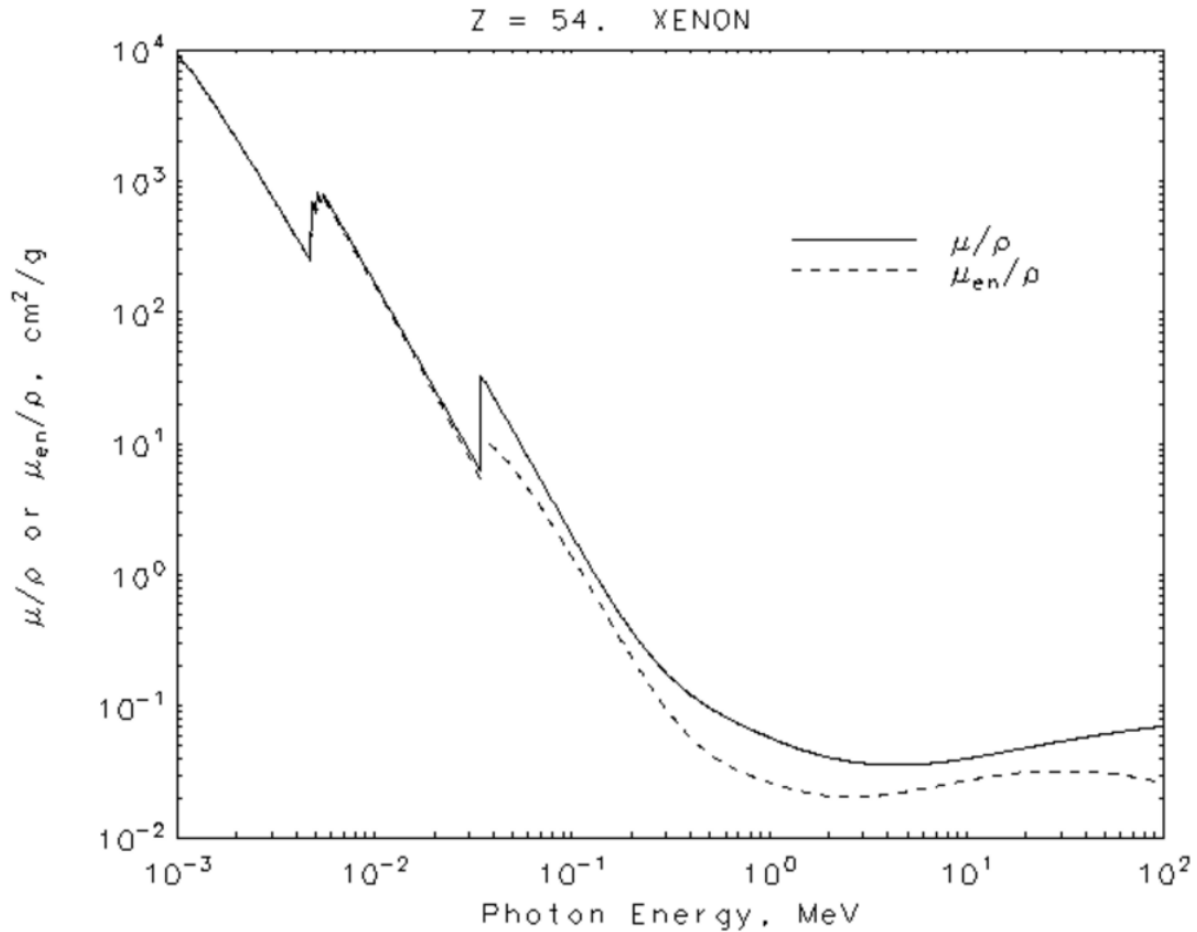
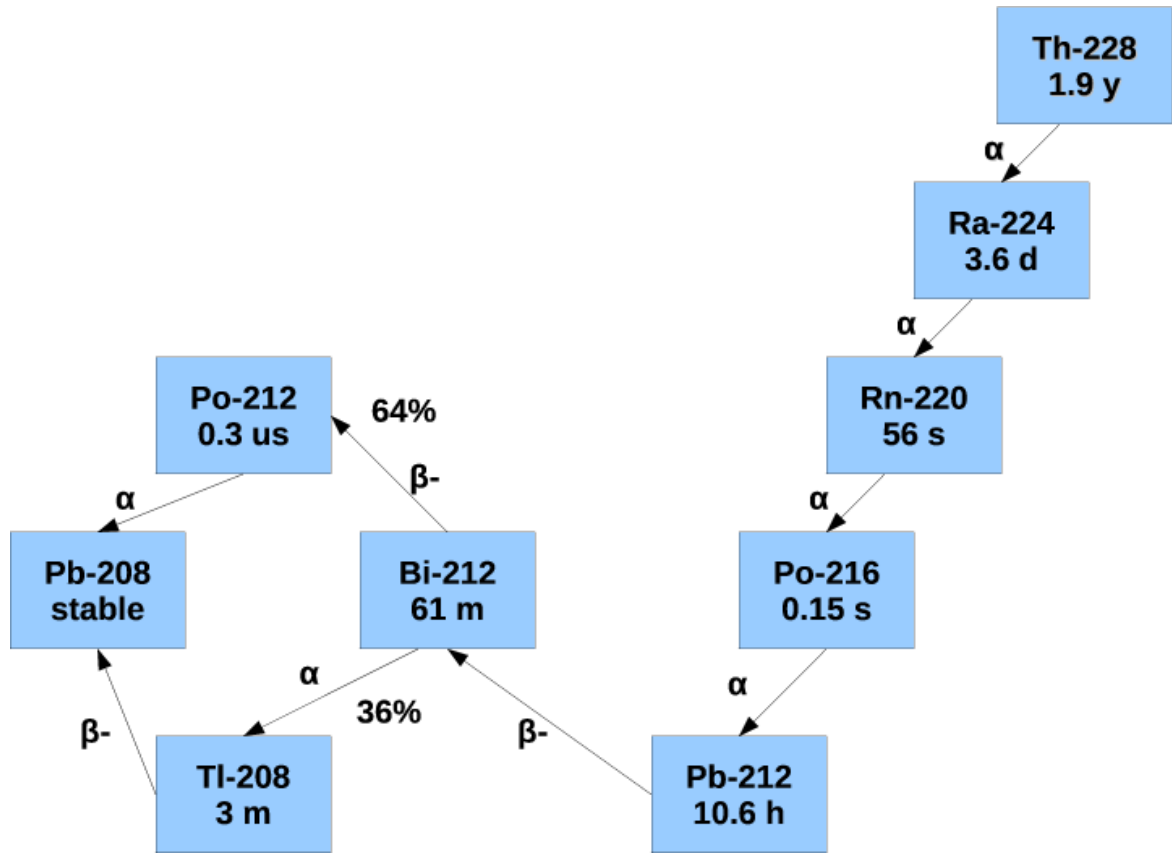


FIGURE 4.1. Attenuation coefficient of xenon. The relevant density for LXe is 3 g/cc.

The calibration source needed should emit high energetic  $\gamma$ s and have a long half life so it will not need to be replaced. After careful examination of all available sources, a  $^{228}\text{Th}$  source is selected, see decay chain is in Fig. 4.2. The energetic  $\gamma$  emission line coming from  $^{208}\text{Tl}$  with energy of 2614 keV and intensity of 99 % can produce good calibration events, and the half life  $t_{(1/2)} = 1.9$  years is long enough. The source is encapsulated inside SS, therefore all  $\beta$  and  $\alpha$  decay products will not reach the detector. Less energetic  $\gamma$  emission lines will penetrate the SV and trigger the PMTs but will not proceed to the FV, therefore will be treated as background.

In order to estimate the percentage of good calibration events from total triggering, all spectral lines are simulated. A summarize of the more energetic  $\gamma$  lines from  $^{228}\text{Th}$  decay chain is presented in Table 4.1.

All decays from  $^{208}\text{Tl}$  have an attenuation factor of 36% which is the branching ratio of  $^{212}\text{Bi} \rightarrow ^{208}\text{Tl}$ . In total the percentage of 2614 keV events in the SV is 0.69% of total source activity.

FIGURE 4.2.  $^{228}\text{Th}$  decay chain

Energy (keV)	SV prob(%)	Isotope	Intensity(%)
511	0.27	$^{208}\text{Tl}$	22.8
583	0.35	$^{208}\text{Tl}$	85
727	0.51	$^{212}\text{Bi}$	6.7
763	0.54	$^{208}\text{Tl}$	1.8
861	0.64	$^{208}\text{Tl}$	12.4
1621	1.15	$^{212}\text{Bi}$	1.5
2614	1.5	$^{208}\text{Tl}$	99

Table 4.1: High energy gamma lines from  $^{228}\text{Th}$  decay chain

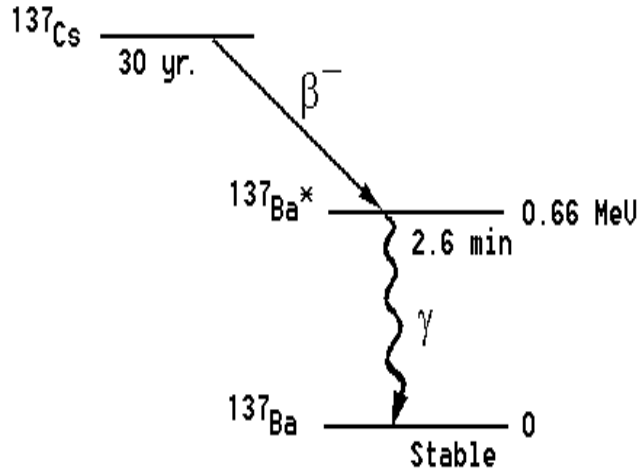


Figure 4.3:  $^{137}\text{Cs}$  decay

#### 4.1.2 Charge collection efficiency

The calibration of the charge collection efficiency is done with less restrict data selection criteria than the ER band calibration. A good calibration sample should have a well defined characteristic feature obtained from the source in various z-positions. By comparing this feature dependency on height a charge collection efficiency map is produced. A well defined feature is the full absorption peak.

$^{137}\text{Cs}$  source which emits a 662 keV *gamma* and  $t_{1/2} = 30$  years, is selected for this calibration. The decay of  $^{137}\text{Cs}$  is shown in Fig 4.3. The source is deposited inside a 25 mm diameter disk.

## 4.2 Collimators

Large portion of the  $\gamma$ s arriving to the SV are scattered at the outskirts of the SV and don't reach the FV, these events trigger the PMTs however are of no use for ER band calibration. In order to lower this portion the gamma source will be placed behind a frame, with a conical hole, such that the solid angle of the hole will cover just the FV when the source is located at the center of the TPC (see Fig. 4.4).

There are two types of collimators: a 16X16X16 cm collimator which moves only vertically on a belt (I-Collimator), and a 10X10X10 cm collimator which also passes below the cryostat (U-Collimator). Both collimators are made of Tungsten with a  $45^\circ$  aperture, sealed with a 1 mm SS plate to reduce the amount of water an emitted  $\gamma$  travels through. The two collimators are designed to host both sources; the  $^{228}\text{Th}$  source which has an M4 thread; and the  $^{137}\text{Cs}$  source which is deposited on a 1/2" disk. An M12 thread is located in front of the source position to allow

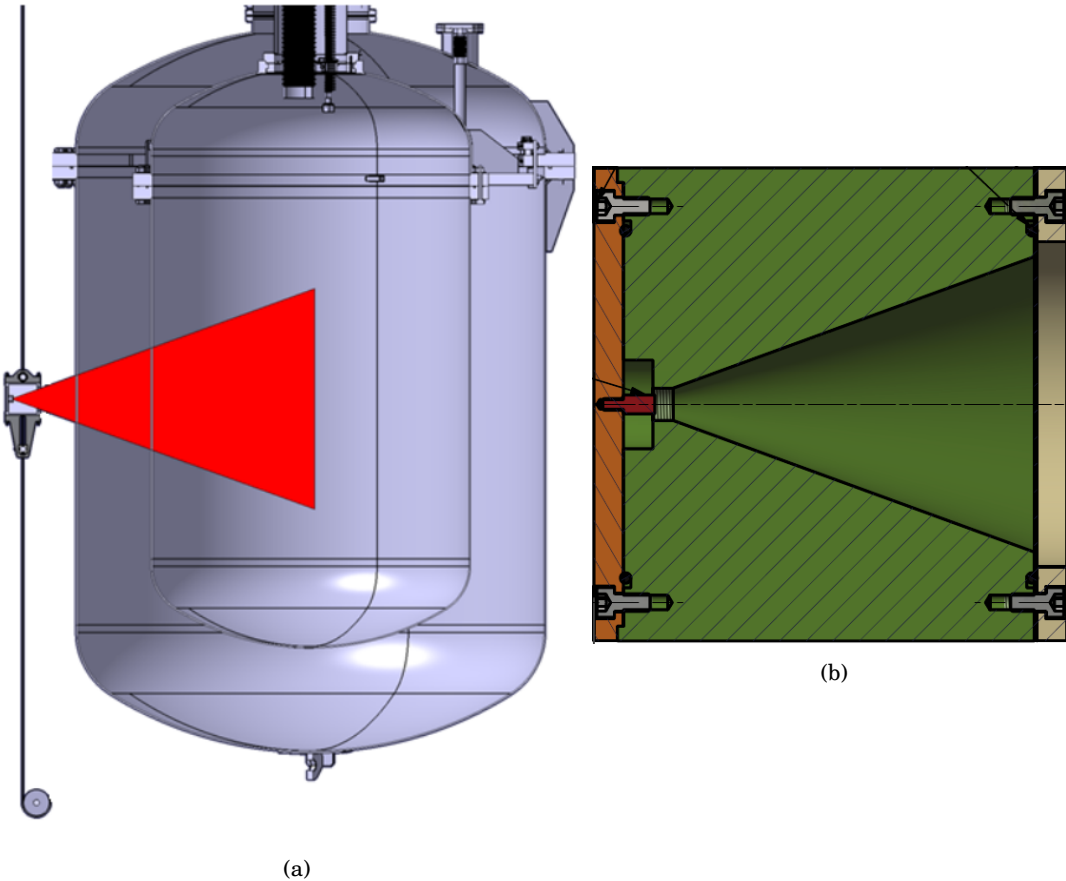


FIGURE 4.4. (a) The cryostat and the collimator shining just some of the FV (b) a CAD design of the collimator with the conical hole.

adding an attenuator.

The collimators are attached to belts that drive them to various calibration positions. The larger collimator is attached to the "I-belt", see Fig. 4.5. The smaller collimator is attached to the "U-belt", that passes below the cryostat, see Fig. 4.5. The two I belts are connected to ports 5 and 11 while the U belt is connected to ports 12 and 7, on the water tank's top flange see Fig. 4.6

#### 4.2.1 Simulation

In order to decide the source activity and collimator dimensions, a MC simulation using the GEANT4 toolkit is used. The DAQ rate assumed for this study is 350 Hz.

The results from the simulation of the I-Collimator which points to the center of the detector are shown in table 4.2, in Fig 4.7 are the original momentum-direction of  $\gamma$ s which do not produce a "good" calibration event. This is of importance to verify only events coming from the collimator opening will reach the detector's SV.



FIGURE 4.5. A picture of the two belts. The blue belt is the I-Belt (currently not the I-Belt in use). The grey belt is the U-Belt (with the U-Collimator mounted), which passes below the cryostat.

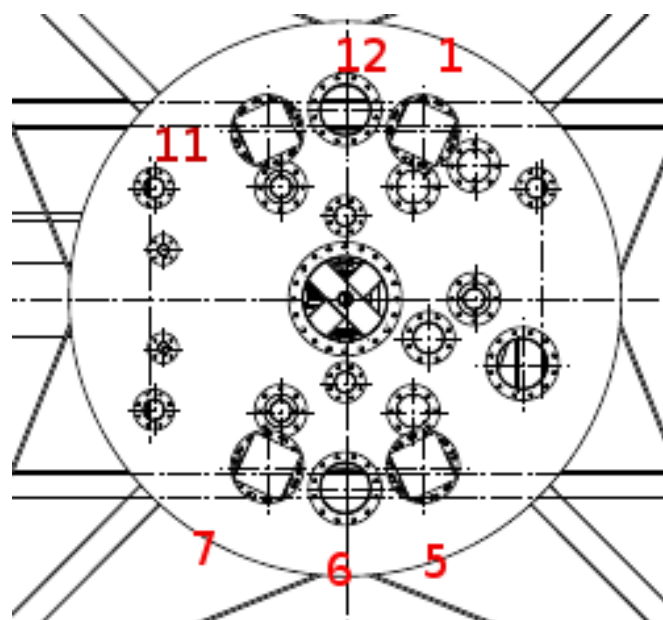


Figure 4.6: A top view of the water tank

number of simulated events	2e9
number of recorded events (SV)	2.5e7
number of good events	53
good evts/day @ 350Hz	65 ± 8
evt/day after bkg reduction	45

TABLE 4.2. result of GEANT4 simulations for a 16X16X16cm collimator with an aperture of 45deg, a good event is an event that scattered only once in the FV with energy deposition of 2-15 keVee

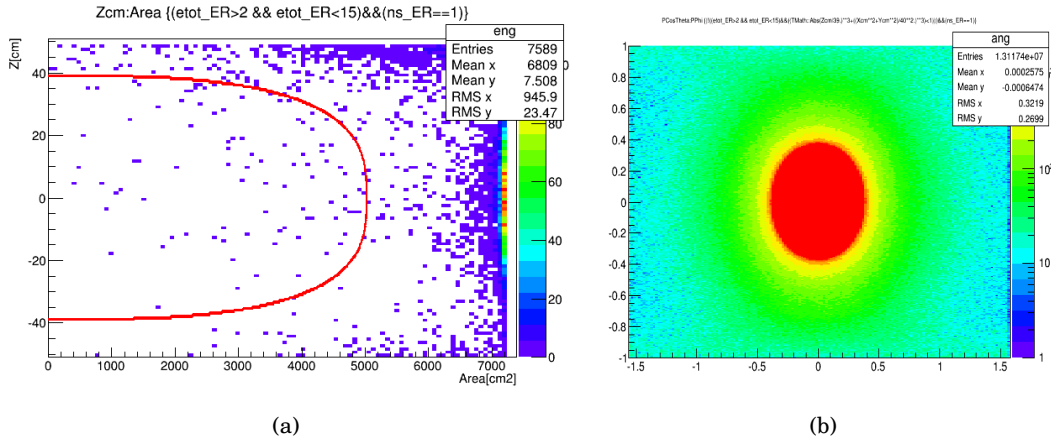


FIGURE 4.7. (a) scatter of good calibration events in the SV, the red line is the border of the FV (b) Intial momentum of background events i.e., events which trigger PMT's and do not meet all three conditions, FV, single scattered, and energy deposition range

The detector is attached via a spring to the water tank's floor, this is done to apply force against the detector's buoyancy while filling water. Therefore the U-belt cannot pass underneath the center of the detector. This causes the collimator to be in a small angle with respect to the center of the detector. The results of the simulation of the U-Collimator are shown in table 4.3 and Fig. 4.8.

### 4.3 Summary

In this chapter I have presented the external calibration technique used in the XENON1T detector. The radioactive sources used for different purposes the collimators holding them, and the belt system driving them. The system is mounted and fully functional.

number of simulated events	4e9
number of recorded events (SV)	4.05e7
number of good events	58
evt/day @ 350Hz good evts	$43 \pm 6$
evt/day after bkg reduction	30
Source activity	80kBq

Table 4.3: Result of GEANT4 simulation for a 10X10X10cm collimator with an aperture of 45 deg, a good event is an event that scattered only once in the FV with energy deposition of 2-15 keVee

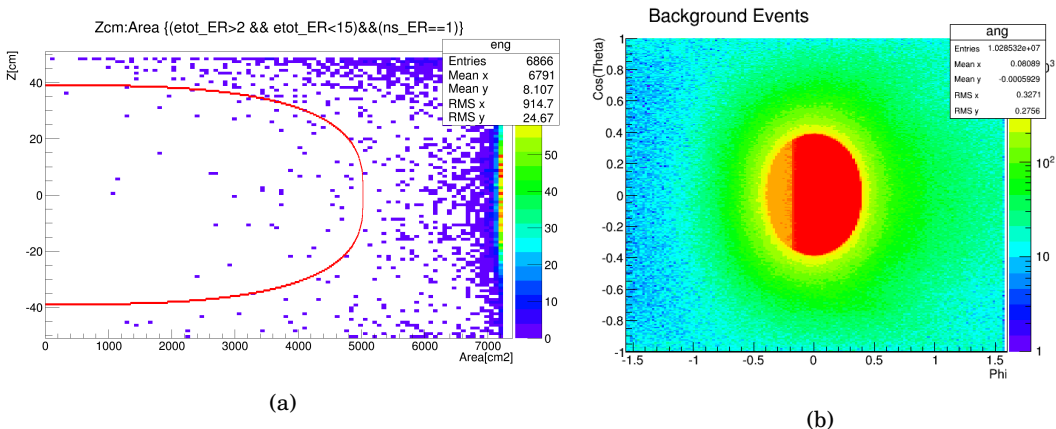


FIGURE 4.8. (a) scatter of good calibration events in the SV, the red line is the border of the FV (b) Intial momentum of background events i.e., events which trigger PMT's and do not meet all three conditions, FV, single scattered, and energy deposition range





## EFT SIGNAL MODEL DETECTOR RESPONSE TABLE

In this Appendix digital tables which can be used to construct an accurate signal model for the EFT analysis given any input recoil spectrum  $dR/dE$  arising from a theoretical model is described. A visualization of the tables is shown in Fig. A.1.

The signal model for the high-energy analysis region can be expressed analytically in the form

$$(A.1) \quad \frac{dR}{dcS1} = \int \frac{dR}{dE} \cdot \epsilon_{S1}(cS1) \cdot \epsilon_{S2'}(E) \cdot p_{S1}(cS1|E) dE$$

$$(A.2) \quad = \int \frac{dR}{dE} G(cS1, E) dE$$

where  $\epsilon_{S1}(cS1)$  and  $\epsilon_{S2'}(E)$  represent analysis cut efficiencies,  $p_{S1}(cS1|E)$  encodes detector effects, and  $dR/dE$  gives the theoretically predicted nuclear recoil rate from WIMP scattering. In the second line, we emphasize that all the detector and analysis effects can be encoded in a single function  $G(cS1, E)$ . To make a signal prediction for the bins in our analysis, this expression needs to be integrated over the appropriate range of  $cS1$  for each bin (and divided by 2 to account for the banding structure in  $cS2_b$ ):

$$(A.3) \quad R_{bin_i} = \frac{1}{2} \int_{lower_i}^{upper_i} \frac{dR}{dcS1} dcS1$$

With some simple rearrangement this rate can be written in terms of an integral over the detector response function  $G$  as follows,

$$(A.4) \quad R_{bin_i} = \frac{1}{2} \int \frac{dR}{dE} \int_{lower_i}^{upper_i} G(cS1, E) dcS1 dE$$

$$(A.5) \quad = \int \frac{dR}{dE} G'_i(E) dE$$

---

APPENDIX A. EFT SIGNAL MODEL DETECTOR RESPONSE TABLE

---

#	E(keV)	bin 1	bin 2	bin 3	bin 4	bin 5	bin 6	bin 7	bin 8	bin 9
3.00e+00	1.44e-22	2.70e-32	1.23e-42	0.00e+00	0.00e+00	0.00e+00	1.44e-22	1.23e-42	0.00e+00	
1.30e+01	9.21e-09	7.58e-14	1.25e-19	6.21e-40	0.00e+00	0.00e+00	9.21e-09	1.25e-19	0.00e+00	
2.30e+01	1.74e-04	1.07e-07	1.24e-11	1.51e-26	0.00e+00	0.00e+00	1.74e-04	1.24e-11	2.64e-32	
3.30e+01	2.22e-02	2.79e-04	6.56e-07	5.47e-18	8.20e-38	0.00e+00	2.25e-02	6.56e-07	1.71e-22	
4.30e+01	1.59e-01	1.68e-02	3.50e-04	1.89e-12	1.24e-28	1.82e-43	1.76e-01	3.50e-04	4.95e-16	
5.30e+01	2.23e-01	1.21e-01	1.40e-02	1.28e-08	6.89e-22	1.43e-34	3.44e-01	1.40e-02	1.82e-11	
6.30e+01	1.10e-01	2.12e-01	9.84e-02	4.73e-06	5.28e-17	5.47e-28	3.21e-01	9.84e-02	2.59e-08	
7.30e+01	2.77e-02	1.54e-01	2.51e-01	2.58e-04	2.20e-13	5.56e-23	1.82e-01	2.51e-01	4.20e-06	
8.30e+01	4.38e-03	6.14e-02	3.67e-01	4.07e-03	1.36e-10	5.26e-19	6.58e-02	3.71e-01	1.65e-04	
9.30e+01	4.65e-04	1.52e-02	3.96e-01	2.73e-02	2.31e-08	1.01e-15	1.57e-02	4.21e-01	2.44e-03	
1.03e+02	3.40e-05	2.47e-03	3.41e-01	9.81e-02	1.50e-06	6.05e-13	2.50e-03	4.21e-01	1.75e-02	
1.13e+02	1.91e-06	2.89e-04	2.29e-01	2.13e-01	4.09e-05	1.22e-10	2.91e-04	3.74e-01	6.77e-02	
1.23e+02	7.75e-08	2.38e-05	1.14e-01	3.28e-01	5.91e-04	1.16e-08	2.39e-05	2.76e-01	1.66e-01	
1.33e+02	2.18e-09	1.33e-06	3.98e-02	3.97e-01	5.03e-03	5.94e-07	1.33e-06	1.55e-01	2.87e-01	
1.43e+02	5.40e-11	6.21e-08	4.06e-02	4.06e-01	2.41e-02	1.42e-05	6.21e-08	6.64e-02	3.74e-01	
1.53e+02	1.33e-12	2.71e-09	2.23e-03	3.66e-01	7.14e-02	1.73e-04	2.71e-09	2.26e-02	4.17e-01	
1.63e+02	2.86e-14	1.00e-10	3.75e-04	2.85e-01	1.51e-01	1.32e-03	1.00e-10	6.04e-03	4.32e-01	
1.73e+02	5.43e-16	3.19e-12	5.09e-05	1.86e-01	2.43e-01	6.76e-03	3.19e-12	1.28e-03	4.34e-01	
1.83e+02	9.29e-18	8.90e-14	5.69e-06	1.01e-01	3.09e-01	2.42e-02	8.90e-14	2.21e-04	4.34e-01	
1.93e+02	1.44e-19	2.21e-15	5.32e-07	4.46e-02	3.23e-01	6.38e-02	2.21e-15	3.14e-05	4.31e-01	
2.03e+02	2.05e-21	4.92e-17	4.23e-08	1.62e-02	2.83e-01	1.29e-01	4.92e-17	3.73e-06	4.28e-01	
2.13e+02	2.71e-23	9.96e-19	2.91e-09	4.89e-03	2.10e-01	2.06e-01	9.96e-19	3.78e-07	4.21e-01	
2.23e+02	3.33e-25	1.85e-20	1.74e-10	1.23e-03	1.31e-01	2.71e-01	1.85e-20	3.29e-08	4.04e-01	
2.33e+02	3.83e-27	3.16e-22	9.25e-12	2.63e-04	6.94e-02	2.99e-01	3.16e-22	2.51e-09	3.69e-01	
2.43e+02	4.16e-29	5.03e-24	4.38e-13	4.80e-05	3.12e-02	2.81e-01	5.03e-24	1.68e-10	3.12e-01	
2.53e+02	4.29e-31	7.48e-26	1.87e-14	7.55e-06	1.20e-02	2.27e-01	7.48e-26	1.00e-11	2.39e-01	
2.63e+02	4.21e-33	1.05e-27	7.23e-16	1.04e-06	3.94e-03	1.58e-01	1.05e-27	5.38e-13	1.62e-01	
2.73e+02	3.95e-35	1.39e-29	2.56e-17	1.25e-07	1.12e-03	9.59e-02	1.39e-29	2.61e-14	9.70e-02	
2.83e+02	3.56e-37	1.74e-31	8.33e-19	1.34e-08	2.77e-04	5.04e-02	1.74e-31	1.15e-15	5.07e-02	
2.93e+02	3.08e-39	2.08e-33	2.51e-20	1.29e-09	6.00e-05	2.31e-02	2.08e-33	4.67e-17	2.31e-02	
3.03e+02	2.58e-41	2.38e-35	7.04e-22	1.11e-10	1.15e-05	9.25e-03	2.38e-35	1.75e-18	9.26e-03	
3.13e+02	2.03e-43	2.61e-37	1.84e-23	8.69e-12	1.95e-06	3.26e-03	2.61e-37	6.06e-20	3.26e-03	
3.23e+02	0.00e+00	2.76e-39	4.54e-25	6.20e-13	2.97e-07	1.01e-03	2.76e-39	1.96e-21	1.01e-03	
3.33e+02	0.00e+00	2.81e-41	1.05e-26	4.06e-14	4.06e-08	2.80e-04	2.81e-41	5.93e-23	2.80e-04	
3.43e+02	0.00e+00	2.72e-43	2.32e-28	2.44e-15	5.04e-09	6.91e-05	2.72e-43	1.69e-24	6.91e-05	

---

TABLE A.1. Detector response table using  $\mathcal{L}_{\text{eff}}$  with constrained scaling parameter set to  $-1\sigma$  value. First column gives recoil energies, subsequent columns give the values of  $G'_i(E)$  for each of the 9 high-energy analysis bins. The sampling is in steps of 10 keV<sub>nr</sub>, which is too coarse to give an accurate signal model for very low WIMP masses, but is suitable for the mass range most relevant to our analysis. Higher resolution  $G'_i(E)$  functions, and  $G'_i(E)$  functions for other values of  $\mathcal{L}_{\text{eff}}$ , are given in supplementary material.

where in the last line we absorb the factor of 1/2 into the definition of  $G'_i$ . We see here that the signal rate for each bin can be expressed as an integral over the recoil spectrum times a detector response function  $G'_i$  for that bin. It is these detector response functions which are shown in Fig. A.1, and which we provide digitally for use by the community. A low-resolution example is given in Table A.1. With these tables it is simple to produce a signal model for our analysis for any theoretical recoil spectrum. The functions  $G'_i$  are provided for three values of the nuisance variable  $\mathcal{L}_{\text{eff}}$ , namely the median value and values at  $\pm 1\sigma$  in  $\mathcal{L}_{\text{eff}}$ . From these, along with the measured background rates given in Table 2.1, one may construct a likelihood which accounts for uncertainties in  $\mathcal{L}_{\text{eff}}$ . Alternatively simply using the  $-1\sigma$  value produces quite an accurate prediction and is generally conservative.

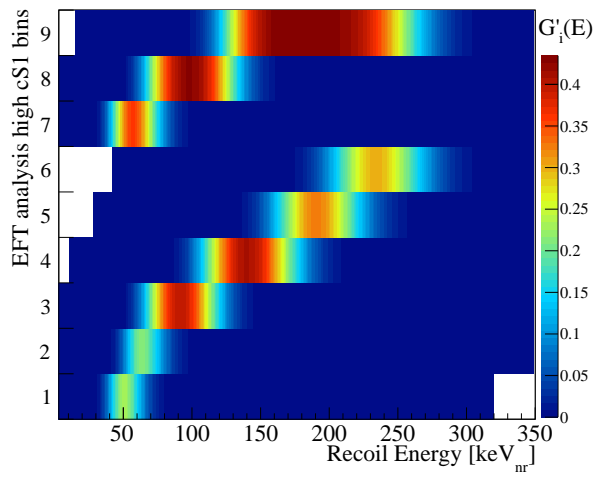


FIGURE A.1. A visualization of the detector response table for  $-1\sigma$  (i.e. conservative)  $\mathcal{L}_{\text{eff}}$ , as provided in the supplementary material. The y axis indicates the bins used for the high-energy signal region of this analysis (explained in 2.1). The x axis shows recoil energies, and the colors give the probability density for a recoil of a given recoil energy to produce an event in each analysis bin. To produce a signal model for this analysis, one simply multiplies the table values by  $dR/dE$  and integrates over  $E$ . The result is the predicted signal rate for each analysis bin.



## BIBLIOGRAPHY

- [1] C. L. Bennett *et al.*, “Nine-Year Wilkinson Microwave Anisotropy Probe (WMAP) Observations: Final Maps and Results,” *Astrophys. J. Suppl.*, vol. 208, p. 20, 2013.
- [2] P. A. R. Ade *et al.*, “Planck 2015 results. XIII. Cosmological parameters,” *Astron. Astrophys.*, vol. 594, p. A13, 2016.
- [3] F. Zwicky, “On the Masses of Nebulae and of Clusters of Nebulae,” *Astrophys. J.*, vol. 86, pp. 217–246, 1937.
- [4] E. Aprile *et al.*, “XENON100 Dark Matter Results from a Combination of 477 Live Days,” *Phys. Rev.*, vol. D94, no. 12, p. 122001, 2016.
- [5] E. Aprile *et al.*, “First Dark Matter Search Results from the XENON1T Experiment,” 2017.
- [6] D. S. Akerib *et al.*, “Improved Limits on Scattering of Weakly Interacting Massive Particles from Reanalysis of 2013 LUX Data,” *Phys. Rev. Lett.*, vol. 116, no. 16, p. 161301, 2016.
- [7] A. Tan *et al.*, “Dark Matter Results from First 98.7 Days of Data from the PandaX-II Experiment,” *Phys. Rev. Lett.*, vol. 117, no. 12, p. 121303, 2016.
- [8] R. Agnese *et al.*, “Search for low-mass weakly interacting massive particles using voltage-assisted calorimetric ionization detection in the supercdms experiment,” *Phys. Rev. Lett.*, vol. 112, p. 041302, Jan 2014.
- [9] R. Bernabei *et al.*, “New results from DAMA/LIBRA,” *Eur. Phys. J.*, vol. C67, pp. 39–49, 2010.
- [10] M. Ackermann *et al.*, “Measurement of separate cosmic-ray electron and positron spectra with the Fermi Large Area Telescope,” *Phys. Rev. Lett.*, vol. 108, p. 011103, 2012.
- [11] M. Aguilar *et al.*, “First Result from the Alpha Magnetic Spectrometer on the International Space Station: Precision Measurement of the Positron Fraction in Primary Cosmic Rays of 0.5–350 GeV,” *Phys. Rev. Lett.*, vol. 110, p. 141102, 2013.
- [12] M. G. Aartsen *et al.*, “Improved limits on dark matter annihilation in the Sun with the 79-string IceCube detector and implications for supersymmetry,” *JCAP*, vol. 1604, no. 04, p. 022, 2016.

## BIBLIOGRAPHY

---

- [13] M. Aaboud *et al.*, “Search for dark matter at  $\sqrt{s} = 13$  TeV in final states containing an energetic photon and large missing transverse momentum with the ATLAS detector,” *Eur. Phys. J.*, vol. C77, no. 6, p. 393, 2017.
- [14] A. M. Sirunyan *et al.*, “Search for dark matter produced with an energetic jet or a hadronically decaying W or Z boson at  $\sqrt{s} = 13$  TeV,” *JHEP*, vol. 07, p. 014, 2017.
- [15] A. D. Lewis, D. A. Buote, and J. T. Stocke, “Chandra observations of Abell 2029: The Dark matter profile at  $< 0.01$  R(VIR) in an unusually relaxed cluster,” *Astrophys. J.*, vol. 586, pp. 135–142, 2003.
- [16] K. G. Begeman, A. H. Broeils, and R. H. Sanders, “Extended rotation curves of spiral galaxies: Dark haloes and modified dynamics,” *Mon. Not. Roy. Astron. Soc.*, vol. 249, p. 523, 1991.
- [17] V. C. Rubin, N. Thonnard, and W. K. Ford, Jr., “Rotational properties of 21 SC galaxies with a large range of luminosities and radii, from NGC 4605 /R = 4kpc/ to UGC 2885 /R = 122 kpc/,” *Astrophys. J.*, vol. 238, p. 471, 1980.
- [18] J. Silk *et al.*, *Particle Dark Matter: Observations, Models and Searches*. Cambridge: Cambridge Univ. Press, 2010.
- [19] A. Einstein, “Lens-Like Action of a Star by the Deviation of Light in the Gravitational Field,” *Science*, vol. 84, pp. 506–507, 1936.
- [20] I. Ferreras, P. Saha, and S. Burles, “Unveiling dark halos in lensing galaxies,” *Mon. Not. Roy. Astron. Soc.*, vol. 383, p. 857, 2008.
- [21] R. Gavazzi, T. Treu, J. D. Rhodes, L. V. Koopmans, A. S. Bolton, S. Burles, R. Massey, and L. A. Moustakas, “The Sloan Lens ACS Survey. 4. The mass density profile of early-type galaxies out to 100 effective radii,” *Astrophys. J.*, vol. 667, pp. 176–190, 2007.
- [22] N. Kaiser and G. Squires, “Mapping the dark matter with weak gravitational lensing,” *Astrophys. J.*, vol. 404, pp. 441–450, 1993.
- [23] D. Clowe, M. Bradac, A. H. Gonzalez, M. Markevitch, S. W. Randall, C. Jones, and D. Zaritsky, “A direct empirical proof of the existence of dark matter,” *Astrophys. J.*, vol. 648, pp. L109–L113, 2006.
- [24] S. W. Randall, M. Markevitch, D. Clowe, A. H. Gonzalez, and M. Bradac, “Constraints on the Self-Interaction Cross-Section of Dark Matter from Numerical Simulations of the Merging Galaxy Cluster 1E 0657-56,” *Astrophys. J.*, vol. 679, pp. 1173–1180, 2008.
- [25] K. Jedamzik and M. Pospelov, “Big Bang Nucleosynthesis and Particle Dark Matter,” *New J. Phys.*, vol. 11, p. 105028, 2009.

- [26] R. D. Peccei and H. R. Quinn, “CP Conservation in the Presence of Instantons,” *Phys. Rev. Lett.*, vol. 38, pp. 1440–1443, 1977.
- [27] M. Pospelov and A. Ritz, “Electric dipole moments as probes of new physics,” *Annals Phys.*, vol. 318, pp. 119–169, 2005.
- [28] C. A. Baker *et al.*, “An Improved experimental limit on the electric dipole moment of the neutron,” *Phys. Rev. Lett.*, vol. 97, p. 131801, 2006.
- [29] J. E. Kim, “Weak Interaction Singlet and Strong CP Invariance,” *Phys. Rev. Lett.*, vol. 43, p. 103, 1979.
- [30] D. S. Akerib *et al.*, “First Searches for Axions and Axionlike Particles with the LUX Experiment,” *Phys. Rev. Lett.*, vol. 118, no. 26, p. 261301, 2017.
- [31] S. Hawking, “Gravitationally collapsed objects of very low mass,” *Monthly Notices of the Royal Astronomical Society*, vol. 152, no. 1, pp. 75–78, 1971.
- [32] B. Carr, F. Kuhnel, and M. Sandstad, “Primordial Black Holes as Dark Matter,” *Phys. Rev.*, vol. D94, no. 8, p. 083504, 2016.
- [33] J. H. MacGibbon, “Can Planck-mass relics of evaporating black holes close the universe?,” *Nature*, vol. 329, pp. 308–309, 1987.
- [34] M. Ricotti, J. P. Ostriker, and K. J. Mack, “Effect of Primordial Black Holes on the Cosmic Microwave Background and Cosmological Parameter Estimates,” *Astrophys. J.*, vol. 680, p. 829, 2008.
- [35] M. Milgrom, “A Modification of the Newtonian dynamics as a possible alternative to the hidden mass hypothesis,” *Astrophys. J.*, vol. 270, pp. 365–370, 1983.
- [36] J. D. Bekenstein, “Relativistic MOND as an alternative to the dark matter paradigm,” *Nucl. Phys.*, vol. A827, pp. 555C–560C, 2009. [,937(2009)].
- [37] G. Steigman and M. S. Turner, “Cosmological Constraints on the Properties of Weakly Interacting Massive Particles,” *Nucl. Phys.*, vol. B253, pp. 375–386, 1985.
- [38] G. Jungman, M. Kamionkowski, and K. Griest, “Supersymmetric dark matter,” *Phys. Rept.*, vol. 267, pp. 195–373, 1996.
- [39] D. Tucker-Smith and N. Weiner, “Inelastic dark matter,” *Phys. Rev.*, vol. D64, p. 043502, 2001.
- [40] S. Lowette, “Accelerator searches for new physics in the context of dark matter,” *J. Phys. Conf. Ser.*, vol. 718, no. 2, p. 022011, 2016.

## BIBLIOGRAPHY

---

- [41] J. Conrad, “Indirect Detection of WIMP Dark Matter: a compact review,” in *Interplay between Particle and Astroparticle physics (IPA2014) London, United Kingdom, August 18-22, 2014*, 2014.
- [42] M. Aguilar *et al.*, “First Result from the Alpha Magnetic Spectrometer on the International Space Station: Precision Measurement of the Positron Fraction in Primary Cosmic Rays of 0.5–350 GeV,” *Phys. Rev. Lett.*, vol. 110, p. 141102, 2013.
- [43] K. Blum, B. Katz, and E. Waxman, “AMS-02 Results Support the Secondary Origin of Cosmic Ray Positrons,” *Phys. Rev. Lett.*, vol. 111, no. 21, p. 211101, 2013.
- [44] A. Achterberg *et al.*, “First Year Performance of The IceCube Neutrino Telescope,” *Astropart. Phys.*, vol. 26, pp. 155–173, 2006.
- [45] M. Ageron *et al.*, “ANTARES: the first undersea neutrino telescope,” *Nucl. Instrum. Meth.*, vol. A656, pp. 11–38, 2011.
- [46] J. D. Lewin and P. F. Smith, “Review of mathematics, numerical factors, and corrections for dark matter experiments based on elastic nuclear recoil,” *Astropart. Phys.*, vol. 6, pp. 87–112, 1996.
- [47] B. Feldstein, A. L. Fitzpatrick, and E. Katz, “Form Factor Dark Matter,” *JCAP*, vol. 1001, p. 020, 2010.
- [48] S. Chang, A. Pierce, and N. Weiner, “Momentum Dependent Dark Matter Scattering,” *JCAP*, vol. 1001, p. 006, 2010.
- [49] A. L. Fitzpatrick, W. Haxton, E. Katz, N. Lubbers, and Y. Xu, “Model Independent Direct Detection Analyses,” 2012.
- [50] N. Anand, A. L. Fitzpatrick, and W. C. Haxton, “Weakly interacting massive particle-nucleus elastic scattering response,” *Phys. Rev.*, vol. C89, no. 6, p. 065501, 2014.
- [51] A. L. Fitzpatrick, W. Haxton, E. Katz, N. Lubbers, and Y. Xu, “The Effective Field Theory of Dark Matter Direct Detection,” *JCAP*, vol. 1302, p. 004, 2013.
- [52] G. Barello, S. Chang, and C. A. Newby, “A Model Independent Approach to Inelastic Dark Matter Scattering,” *Phys. Rev.*, vol. D90, no. 9, p. 094027, 2014.
- [53] K. Hiraide and O. B. O. T. X. Collaboration, “Recent results of direct dark matter search with XMASS,” *PoS*, vol. ICHEP2016, p. 213, 2016.
- [54] D. S. Akerib *et al.*, “The Large Underground Xenon (LUX) Experiment,” *Nucl. Instrum. Meth.*, vol. A704, pp. 111–126, 2013.

- [55] X. Cao *et al.*, “PandaX: A Liquid Xenon Dark Matter Experiment at CJPL,” *Sci. China Phys. Mech. Astron.*, vol. 57, pp. 1476–1494, 2014.
- [56] E. Aprile *et al.*, “The XENON1T Dark Matter Experiment,” 2017.
- [57] A. Zani, “The WArP Experiment: A Double-Phase Argon Detector for Dark Matter Searches,” *Adv. High Energy Phys.*, vol. 2014, p. 205107, 2014.
- [58] A. Rubbia, “ArDM: A Ton-scale liquid Argon experiment for direct detection of dark matter in the universe,” *J. Phys. Conf. Ser.*, vol. 39, pp. 129–132, 2006.
- [59] T. Alexander *et al.*, “DarkSide search for dark matter,” *JINST*, vol. 8, p. C11021, 2013.
- [60] A. Manzur, A. Curioni, L. Kastens, D. N. McKinsey, K. Ni, and T. Wongjirad, “Scintillation efficiency and ionization yield of liquid xenon for mono-energetic nuclear recoils down to 4 keV,” *Phys. Rev.*, vol. C81, p. 025808, 2010.
- [61] E. Aprile *et al.*, “Measurement of the Scintillation Yield of Low-Energy Electrons in Liquid Xenon,” *Phys. Rev.*, vol. D86, p. 112004, 2012.
- [62] L. Baudis, H. Dujmovic, C. Geis, A. James, A. Kish, A. Manalaysay, T. Marrodan Undagoitia, and M. Schumann, “Response of liquid xenon to Compton electrons down to 1.5 keV,” *Phys. Rev.*, vol. D87, no. 11, p. 115015, 2013.
- [63] D. S. Akerib *et al.*, “Low-energy (0.7-74 keV) nuclear recoil calibration of the LUX dark matter experiment using D-D neutron scattering kinematics,” 2016.
- [64] W. H. Lippincott, K. J. Coakley, D. Gastler, A. Hime, E. Kearns, D. N. McKinsey, J. A. Nikkel, and L. C. Stonehill, “Scintillation time dependence and pulse shape discrimination in liquid argon,” *Phys. Rev.*, vol. C78, p. 035801, 2008. [Erratum: *Phys. Rev.*C81,039901(2010)].
- [65] D. Muna, “The DRIFT-II directional dark matter detector,” *Nucl. Phys. Proc. Suppl.*, vol. 173, pp. 172–175, 2007.
- [66] C. Deaconu, M. Leyton, R. Corliss, G. Druitt, R. Eggleston, N. Guerrero, S. Henderson, J. Lopez, J. Monroe, and P. Fisher, “Measurement of the directional sensitivity of Dark Matter Time Projection Chamber detectors,” *Phys. Rev.*, vol. D95, no. 12, p. 122002, 2017.
- [67] R. Yakabe, Y. Yamaguchi, K. Miuchi, K. Nakamura, S. Nakaura, T. Hashimoto, T. Ikeda, and R. Taishaku, “Direction-Sensitive Dark Matter Search Using Micro Time-Projection-Chamber,” *JPS Conf. Proc.*, vol. 11, p. 040002, 2016.
- [68] Q. Riffard *et al.*, “MIMAC low energy electron-recoil discrimination measured with fast neutrons,” *JINST*, vol. 11, no. 08, p. P08011, 2016.

## BIBLIOGRAPHY

---

- [69] V. Chepel and H. Araujo, “Liquid noble gas detectors for low energy particle physics,” *JINST*, vol. 8, p. R04001, 2013.
- [70] R. H. Dicke, “Coherence in spontaneous radiation processes,” *Phys. Rev.*, vol. 93, pp. 99–110, Jan 1954.
- [71] D. Rosenberger, “Superstrahlung in gepulsten argon-, krypton und xenon-entladungen,” *Physics Letters*, vol. 14, pp. 32–32, Jan. 1965.
- [72] M. Gross and S. Haroche, “Superradiance: An essay on the theory of collective spontaneous emission,” *Physics Reports*, vol. 93, no. 5, pp. 301 – 396, 1982.
- [73] M. Benedict, *Super-radiance: Multiatom Coherent Emission*. Series in Optics and Optoelectronics, Taylor & Francis, 1996.
- [74] J. Angle *et al.*, “First Results from the XENON10 Dark Matter Experiment at the Gran Sasso National Laboratory,” *Phys. Rev. Lett.*, vol. 100, p. 021303, 2008.
- [75] E. Aprile *et al.*, “The XENON100 Dark Matter Experiment,” *Astropart. Phys.*, vol. 35, pp. 573–590, 2012.
- [76] E. Aprile *et al.*, “Effective field theory search for high-energy nuclear recoils using the XENON100 dark matter detector,” 2017.
- [77] E. Aprile *et al.*, “Dark Matter Results from 225 Live Days of XENON100 Data,” *Phys. Rev. Lett.*, vol. 109, p. 181301, 2012.
- [78] E. Aprile *et al.*, “Analysis of the XENON100 Dark Matter Search Data,” *Astropart. Phys.*, vol. 54, pp. 11–24, 2014.
- [79] E. Aprile *et al.*, “The neutron background of the XENON100 dark matter search experiment,” *J. Phys.*, vol. G40, p. 115201, 2013.
- [80] E. Aprile *et al.*, “Response of the XENON100 Dark Matter Detector to Nuclear Recoils,” *Phys. Rev.*, vol. D88, p. 012006, 2013.
- [81] E. Aprile *et al.*, “Observation and applications of single-electron charge signals in the XENON100 experiment,” *J. Phys.*, vol. G41, p. 035201, 2014.
- [82] E. Aprile *et al.*, “Limits on spin-dependent wimp-nucleon cross sections from 225 live days of xenon100 data,” *Physical review letters*, vol. 111, no. 2, p. 021301, 2013.
- [83] G. Cowan, K. Cranmer, E. Gross, and O. Vitells, “Asymptotic formulae for likelihood-based tests of new physics,” *Eur. Phys. J.*, vol. C71, p. 1554, 2011. [Erratum: Eur. Phys. J.C73,2501(2013)].

- [84] E. Aprile *et al.*, “Dark Matter Results from 100 Live Days of XENON100 Data,” *Phys. Rev. Lett.*, vol. 107, p. 131302, 2011.
- [85] E. Aprile *et al.*, “Likelihood Approach to the First Dark Matter Results from XENON100,” *Phys. Rev.*, vol. D84, p. 052003, 2011.
- [86] A. L. Read, “Modified frequentist analysis of search results (The CL(s) method),” in *Workshop on confidence limits, CERN, Geneva, Switzerland, 17-18 Jan 2000: Proceedings*, pp. 81–101, 2000.
- [87] K. Schneck *et al.*, “Dark matter effective field theory scattering in direct detection experiments,” *Phys. Rev.*, vol. D91, no. 9, p. 092004, 2015.
- [88] Z. Ahmed *et al.*, “Dark Matter Search Results from the CDMS II Experiment,” *Science*, vol. 327, pp. 1619–1621, 2010.
- [89] D. Yu. Akimov *et al.*, “Limits on inelastic dark matter from ZEPLIN-III,” *Phys. Lett.*, vol. B692, pp. 180–183, 2010.
- [90] E. Aprile *et al.*, “Implications on Inelastic Dark Matter from 100 Live Days of XENON100 Data,” *Phys. Rev.*, vol. D84, p. 061101, 2011.
- [91] A. De Simone and T. Jacques, “Simplified models vs. effective field theory approaches in dark matter searches,” *Eur. Phys. J.*, vol. C76, no. 7, p. 367, 2016.
- [92] J. Billard, L. Strigari, and E. Figueroa-Feliciano, “Implication of neutrino backgrounds on the reach of next generation dark matter direct detection experiments,” *Phys. Rev.*, vol. D89, no. 2, p. 023524, 2014.
- [93] N. G. Basov, V. A. Danilychev, and Y. M. Popov, “Stimulated emission in the vacuum ultraviolet region,” *Soviet Journal of Quantum Electronics*, vol. 1, no. 1, p. 18, 1971.
- [94] F. H. Mies, “Stimulated emission and population inversion in diatomic bound-continuum transitions,” *Molecular Physics*, vol. 26, no. 5, pp. 1233–1246, 1973.
- [95] S. Agostinelli *et al.*, “Geant4 a simulation toolkit,” *Nuclear Instruments and Methods in Physics Research Section A: Accelerators, Spectrometers, Detectors and Associated Equipment*, vol. 506, no. 3, pp. 250 – 303, 2003.

